17548

**NATIONAL LIBRARY**
**OTTAWA**

CANADA

**BIBLIOTHÈQUE NATIONALE**
**OTTAWA**

NAME OF AUTHOR....G. D. Hillman....................

TITLE OF THESIS....THIN FILM TRANSDUCERS
AND THEIR APPLICATION
TO ACOUSTO-OPTIC MODULATORS

UNIVERSITY........U of Alberta................

DEGREE FOR WHICH THESIS WAS PRESENTED....Ph. D..........

YEAR THIS DEGREE GRANTED..........1973..........

Permission is hereby granted to THE NATIONAL LIBRARY OF CANADA to microfilm this thesis and to lend or sell copies of the film.

The author reserves other publication rights, and neither the thesis nor extensive extracts from it may be printed or otherwise reproduced without the author's written permission.

(Signed)....G. D. Hillman.

PERMANENT ADDRESS:

34 Crystal Beach Drive
Ottawa, Ontario
..........................

DATED...Oct. 2.......1973

NL-91 (10-68)

THE UNIVERSITY OF ALBERTA

# THIN FILM TRANSDUCERS AND THEIR APPLICATION TO ACOUSTO-OPTIC MODULATORS

by

Ⓒ GARTH DECKER HILLMAN

A THESIS

SUBMITTED TO THE FACULTY OF GRADUATE STUDIES AND RESEARCH
IN PARTIAL FULFILMENT OF THE REQUIREMENTS FOR THE DEGREE
OF DOCTOR OF PHILOSOPHY

DEPARTMENT OF ELECTRICAL ENGINEERING

EDMONTON, ALBERTA

FALL, 1973

THE UNIVERSITY OF ALBERTA

FACULTY OF GRADUATE STUDIES AND RESEARCH

The undersigned certify that they have read, and recommend to the Faculty of Graduate Studies and Research, for acceptance, a thesis entitled THIN FILM TRANSDUCERS AND THEIR APPLICATION TO ACOUSTO-OPTIC MODULATORS submitted by GARTH DECKER HILLMAN in partial fulfilment of the requirements for the degree of Doctor of Philosophy.

H. Seguin ......

Supervisor

..............................

Ronald P W Lawson ......

..............................

..............................

External Examiner

Date Oct. 26/73

# ABSTRACT

The deposition system and parameters for repeatably producing highly oriented Zinc Oxide (ZnO) thin films suitable for high frequency acousto-electric transducers are described. At the higher supersaturations used, the crystalline state of the nucleating surface and partial pressure of oxygen in the sputtering gas mix are shown to critically affect the texture and level of stress in the ZnO films. In particular, the level of orientation in the ZnO thin films images that in the nucleating gold thin film underlay. The orientation of the gold thin film, in turn, depends upon the method of deposition used and is shown to be highest when deposited by sputtering. In addition to the crystalline structure of the ZnO thin films, their resistivity, band gap energy, dielectric constant, index of refraction and electro-mechanical coupling coefficient are determined.

The value of the electromechanical coupling coefficient is determined by comparing the experimental insertion loss data with that generated on a computer. An outline is given for the theory upon which the computer program is based. In order for a comparison to be made, the experimental data must be corrected for acoustic losses. The acoustic loss data for a compressional wave propagating along the <11$\bar{1}$> axis in Germanium at 300°K is presented.

The performance of a germanium acousto-optic modulator employing a ZnO thin film transducer is compared with that expected theoretically. The theory required for this comparison is outlined. At 10.6$\mu$ the relevant photoelastic constant of germanium, $P'_{33}$, is found to be .42.

Also, the theory is shown to adequately describe the interaction between an electromagnetic wave and an acoustic wave in the Bragg regime.

It is predicted that such a modulator can be used intracavity to simultaneously couple energy out of a $CO_2$ laser cavity efficiently and frequency modulate this coupled radiation.

# ACKNOWLEDGEMENTS

The author wishes to thank his supervising professor, Dr. H.J.J. Seguin, for his help and encouragement throughout the course of this research.

Without the understanding, encouragement and assistance of his loving wife, Shirley, this work would not have been possible and the author most gratefully acknowledges this.

The author would also like to express his appreciation to the following people:

Barry Arnold for his excellent optical and thin film work which was so necessary to the project.

Bruce White, Roy Schmaus, Jim Dow and 'Rapid' Robert Gaver for their technical assistance.

M.E. Pedinoff for the project proposal.

Members of the Laser Group for their helpful discussions and assistance.

Maureen K. Mounteer for her excellent typing of this thesis.

The staff of the machine shop headed by E. Buck for their excellent service and workmanship.

The author also wishes to thank the National Research Council of Canada and the Department of Electrical Engineering for their financial support.

# TABLE OF CONTENTS

Page

CHAPTER I : INTRODUCTION 1

1.1 Stimulus for the Investigation 1

1.2 Background 2

1.3 Description of Proposed Heterodyne System 6

1.4 Present Work 11

CHAPTER II : THE ACTIVE MEDIUM AND FABRICATION SYSTEM 14

2.1 Introduction 14

2.2 Choice of Active Medium Material 15

2.3 Thin Film Deposition System 20

2.3.1 Choice of Deposition System 21

2.3.2 The Sputtering Process in a Triode System 22

2.3.3 General Characteristics of a Triode Sputtering System 25

2.3.4 The Deposition System Constructed 28

2.3.5 System Safeguards 41

2.4 Discussion 44

2.5 Conclusion 48

CHAPTER III : INFLUENCE OF DEPOSITION PARAMETERS ON FILM CHARACTERISTICS 50

3.1 Introduction 50

3.2 X-Ray Analysis 51

3.3 Thickness Determination 55

3.4 Factors Affecting the Level of Orientation in ZnO 57

Page
3.4.1 Sputtering Potential 57
3.4.2 Deposition Rate 59
3.4.3 Partial Pressure of Oxygen in Sputtering Gas Mix - $P_{O_2}$ 60
3.4.4 Nucleating Surface 64
3.5 Stress Manifestation 67
3.6 Non-Structural Analysis 70
3.6.1 Electron Probe 70
3.6.2 Resistivity 72
3.6.3 Band Gap 73
3.6.4 Optical Properties in the Infrared 73
3.7 Discussion 76
3.8 Conclusion 78
CHAPTER IV : TRANSDUCER FABRICATION AND EVALUATION 80
4.1 Introduction 80
4.2 Transducer Fabrication Recipe 81
4.3 Mathematical Model of Complete Electro-Acoustic System 84
4.4 Insertion Loss Measurement 94
4.5 Acoustic Losses 96
4.5.1 Diffraction Losses 96
4.5.2 Intrinsic Losses 100
4.6 Evaluation of Coupling Coefficient 102
4.7 Conclusion 106
CHAPTER V : ACOUSTO-OPTIC PERFORMANCE OF GERMANIUM EMPLOYING A ZnO THIN FILM TRANSDUCER 108
5.1 Introduction 108

Page

5.2 Theoretical Description of Acousto-Optic Diffraction 109

5.2.1 Difference Differential Equation 109

5.2.2 Derivation of Diffracted Intensity 115

5.2.3 The Raman-Nath Parameter for a Single Crystal Solid 117

5.3 Acousto-Optic Experimental Results 120

5.3.1 Determination of Photoelastic Constant of Germanium ($p'_{33}$) 120

5.3.2 Angular Dependence of Diffracted Intensity 122

5.4 Conclusion 125

CHAPTER VI : CONCLUSION 128

REFERENCES 130

APPENDIX 1 139

APPENDIX 2 142

# LIST OF TABLES

Page

TABLE 2.1 : Materials for High-Frequency Piezoelectric Transducers (ca. 1969) 16

TABLE 4.1 : Sputtering Parameters 82

TABLE 4.2 : Input Data for Computer Program 104

# LIST OF FIGURES

Page

FIGURE 1.1 Proposed 10.6μ Heterodyne System Employing an Intracavity Acousto-Optic Modulator 7

FIGURE 2.1 Low Pressure Sputtering or Triode System 23

2.2 Schematic of Triode Sputtering Module Developed 29

2.3 Photograph of Triode Deposition System Constructed 31

2.4 Substrate Arm Vacuum Plate; Substrate Table, Masks and Holder; Presputtering Shield; Target Shield 31

2.5 View of Targets During Operation 31

2.6 Cross-Section of R.F.-D.C. Probe - Target Mounting End 38

2.7 Cross-Section of Changing Arm Assembly 40

2.8 System Block Diagram Showing Electrical Safeguards 42

2.9 Proposed Metal or Semiconductor Target Shroud 46

2.10 Top View of Proposed Deposition System 46

FIGURE 3.1 Graphical Interpretation of the Bragg Law in Terms of Reciprocal Lattice Vectors 52

3.2 Graphical Explanation of X-Ray Distribution from Textured Specimen - Modified Debye-Scherrer Powder X-Ray Diffraction Technique 54

Page

3.3 Tallysurf 4 Recorder Output Trace of Edge of Chromium Thin Film Sputtered on Glass Disc 56

3.4 X-Ray Diffraction Photographs of ZnO Triode Sputtered on Single Crystal Germanium 58

(a) 800v, 34ma, 10k; 25 Å/min

(b) 1500v, 34ma, 10k; 50 Å/min

3.5 X-Ray Diffraction Photograph of ZnO Triode Sputtered on Single Crystal Germanium - 200Å/min 58

3.6 X-Ray Diffraction Photographs of ZnO Triode Sputtered on Pyrex - 1.65kv, 44ma, 10k, 300 Å/min 61

(a) $P_{O_2} = 0\%$

(b) $P_{O_2} = 30\%$

(c) $P_{O_2} = 60\%$

3.7 S.E.M. Photographs of the Thin Films Represented in:- 63

(a) Fig. 3.6a

(b) Fig. 3.6c

3.8 Photograph of a Large Fractured Area in a ZnO Thin Film. (500x) 63

3.9 Photograph of a Fractured Area in which the Expelled Material has been Re-Incorporated into the Film. (50x) 63

Page

3.10 X-Ray Diffraction Photographs of ZnO Triode Sputtered on Gold Thin Film Surfaces 65
(a) Gold-Flash Evaporated, Not Annealed
(b) Gold-Slowly Evaporated, Vacuum Annealed
(c) Gold-Triode Sputtered, Vacuum Annealed

3.11 Photograph of ZnO Film Surface in which Chamber Debris has been Incorporated into the Film. (500x) 69
(a) Analyser Not Crossed
(b) Analyser Crossed

3.12 Photograph of ZnO Film Surface Showing Typical Size and Density of Inclusions. (50x) 69
(a) Analyser Not Crossed
(b) Analyser Crossed

3.13 Visible Spectrophotometer Scan of ZnO Film Deposited on Pyrex 74

3.14 Infrared Spectrophotometer Scans on: 75
(a) Uncoated Single Crystal Germanium
(b) Germanium Substrate A.R. Coated with ZnO on Both Sides
Infrared Absorption Spectra on:
(c) Bulk Single Crystal Zinc Oxide
(d) Tungsten Oxide (not to scale)

Page

FIGURE 4.1 Layered Structure to be Modelled 86
4.2 Equivalent Circuit of Active Layer 86
4.3 Equivalent Circuit of Inactive Layer 86
4.4 Equivalent Circuit for Determining 'M' 90
4.5 Circuit for Insertion Loss Calculation 90
4.6 Insertion Loss Measurement Circuit 95
4.7 Stainless Steel Mount for Germanium Cubes; U.H.F. Coupler 97
4.8 Effects of Acoustic Diffraction on the Compressional Echo Pattern in Germanium 99
4.9 Inadvertently Generated Shear Waves 99
4.10 Exponential Decay of Compressional Wave in Germanium at 300°K and 210 MHz 99
4.11 Acoustic Losses in Germanium for Compressional Waves Propagating in the <111> Direction at 300°K 101
4.12 Experimental and Computed Insertion Loss versus Frequency 103
FIGURE 5.1 Ultrasonic Diffraction of Electromagnetic Radiation - Orientation of the Partial Wave Vectors n = 0, +1, -1. 110
5.2 Schematic Diagram of Experimental Apparatus 121
5.3 Circuit for Controlling and Monitoring Transducer Input Power (Power Meter) and Reflected Power (Scope) 123

Page

5.4 Diffracted 10.6μ Laser Pulses at the Angular Locations of Maximum Intensity 124

(a) Θ' = 18.75°

(b) Θ' = 20°

(c) Θ' = 21.25°

5.5 First Order Light Intensity versus Angle of Incidence (Θ' external) with ν = .1 and Q = 291 126

# LIST OF SYMBOLS

$P_t$ = peak transmitted power

$\sigma_o$ = object cross-sectional area

$A_{tr}$ = area of transmit-receive antenna

$\lambda$ = radiation wavelength

$\xi_{max}$ = maximum range

$P_{r_{min}}$ = minimum discernible signal

$\omega_d$ = Doppler frequency shift in radians/sec

$v_t$ = target radial velocity

$c$ = velocity of light in a vacuum

$\omega_c$ = carrier frequency in radians/sec

$\omega_{if}$ = information frequency

$i_s(\omega_{if})$ = signal current at difference frequency

$\omega_s$ = ultrasonic drive frequency in radians/sec

$E_s$ = signal electric field intensity

$E_{LO}$ = local oscillator electric field intensity

$\ell_d$ = effective linear dimension of detector surface

$A_d$ = detector surface area

$\theta$ = angle between the directions of propagation of the signal and local oscillator waves

$k_t$ = thickness coupling coefficient
K = relative dielectric constant
$f_o$ = parallel resonance frequency
Zo = characteristic mechanical impedance
d = thickness of active medium
v = acoustic velocity
$\rho$ = material density
f = frequency
Z = electrical impedance
$\varepsilon_o$ = permittivity of free space
$j^+$ = ion current density
e = electronic charge
$m^+$ = mass of ion
$V_T$ = probe potential
$V_a$ = anode potential
$d_{sh}$ = sheath thickness
$I^+$ = target ion current
$A_T$ = effective area of target
$n^+$ = number of ions incident on a unit area per unit time
$\rho^+$ = ion density in glow discharge
$\nu^+$ = average random velocity of ions
M.F.P. = mean free path
T° = absolute temperature in °K
$P_T$ = total gas pressure
$K_B$ = Boltzmann's constant
§ = molecular diameter
$f_i$ = fraction of impurity species i trapped

$\alpha_i$ = effective sticking coefficient of the species i
$D_R$ = deposition rate
$\mu$ = $10^{-6}$ mm of mercury or $10^{-6}$ mm
$B$ = magnetic field intensity
$N_i$ = number of atoms of species i incident per unit area per unit time

$d_{hk\ell}$ = interplanar spacing between planes having the Miller indices h, k, $\ell$.
$\Theta_B$ = Bragg angle
$\lambda_x$ = x-ray wavelength
$\vec{\sigma}_{hk\ell}$ = reciprocal lattice vector
$\vec{n}$ = unit vector normal to the set of diffracting planes in the crystal
$d_{sf}$ = specimen to film distance
$P_{O_2}$ = partial pressure of oxygen in the sputtering gas mix
$P_{Ar}$ = partial pressure of argon in the sputtering gas mix
$C_{sp}$ = weight concentration of an element in the specimen
$C_{st}$ = weight concentration of an element in the standard
$I_{sp}$ = measured intensity of an x-ray line of the element in the specimen
$I_{st}$ = measured intensity of an x-ray line of the element in the standard
$r$ = resistivity
$A$ = cross-sectional area

$\ell$ = electrode separation
$R$ = measured resistance

$Zo_n$ [illegible] characteristic acoustic impedance of layer n
$v_n^d$ [illegible] dilatational acoustic velocity in layer n
$\rho_n$ = material density of layer n
$d_n$ = thickness of layer n
$\beta_{ij}^s$ = constant strain dielectric impermeability tensor component
$C_{ij}^D$ = constant displacement elastic stiffness component in matrix notation
$C_o$ = clamped capacitance
$\phi$ = electro-mechanical transformer turns ratio
$h_{33}$ = piezoelectric component in matrix notation
$S$ = top electrode area
$\gamma_n$ = phase constant of layer n
$j$ = $\sqrt{-1}$
$M_n^a$ = acoustic matrix for layer n
$F$ = force at interface
$\dot{u}$ = particle velocity at interface
$Z_b = jZ_b'$ = acoustic impedance of backing layers
$C_{se}$ = series capacitance due to ZnS layer
$K_{ZnS}$ = relative dielectric constant of Zinc Sulphide
$Zo_d$ = characteristic acoustic impedance of delay medium
$M_n^e$ = electrical matrix for layer n
$M_n^{e-a}$ = electro-acoustic matrix for layer n
$Z_s=R_s+jX_s$ = electrical source impedance

$V$ = voltage
$I$ = current
$Z_L = R_L + jX_L$ = electrical load impedance
I.L. = insertion loss
$|M|$ = determinant of matrix M
$M^{-1}$ = inverse of matrix M
$a$ = half of the smallest transducer dimension
$\Lambda$ = acoustic wavelength
$\alpha_d$ = acoustic loss due to diffraction
$\alpha_i$ = acoustic loss due to intrinsic attenuation

$\nabla^2 = \frac{\partial^2}{\partial x^2} + \frac{\partial^2}{\partial y^2} + \frac{\partial^2}{\partial z^2}$
$E$ = electric field intensity
$\Omega$ = sound frequency
$\kappa$ = acoustic wave number
$\zeta_o$ = index of refraction
$\omega$ = $2\pi f$; radian frequency of electromagnetic wave
$k$ = vacuum wave number
$\Theta$ = the compliment of the angle between $\vec{k}$ and $\vec{\kappa}$
(in the diffracting medium)
$\lambda_o$ = vacuum wavelength
$A(x,z,t)$ = slowly varying spatial and time dependence of E
$\Phi_m(x)$ = slowly varying x dependence of E
$\Phi_m^{*}(x)$ = complex conjugate of $\Phi(x)$
$L$ = transducer length
$H$ = transducer height
$\nu$ = Raman-Nath parameter

$\alpha$ = dimensionless parameter related to the angle of incidence of an E-M wave on an acoustic wave

$Q$ = dimensionless parameter related to the spatial phase difference between diffraction orders

P.L. = radiation path length

$\beta_n$ = angle between direction of diffracted beam of order n and zeroth order beam

$\Delta\delta$ = spatial phase difference between $n^{th}$ diffracted order and zeroth order

$\sigma$ = function of $\alpha$, $Q$, and $\nu$

$I_o$ = intensity of zeroth order diffracted beam

$I_1$ = intensity of first order diffracted beam

$B_{ij}$ = dielectric impermeability tensor component

$p_{ijk\ell}$ = elasto-optic coefficient in tensor notation

$s_{k\ell}$ = strain in tensor notation

$K_{ij}$ = dielectric permittivity tensor component

$\delta_{ik}$ = Kronecker delta

$\zeta_{ij}$ = refractive index tensor component

$T_{mnop}$ = general fourth rank tensor component

$A^T$ = axes transformation matrix having components $a^T_{ij}$

$P_{del}$ = average acoustic power delivered to crystal

$P_{RF}$ = R.F. power incident on transducer impedance matching network

$\Psi$ = photoelastic figure of merit

$T$ = effective transduction efficiency

$\theta'$ = angle between incident infrared beam and the normal to the diffracting cube

$p_{11}, p_{12}, p_{44}$ = the non-zero photoelastic constants (written in reduced notation) for germanium (m3m) [5.7]

# CHAPTER I

# INTRODUCTION

## 1.1 Stimulus for the Investigation

High frequency acousto-optic modulators and deflectors utilizing surface and bulk acoustic waves are presently being successfully employed in the control and processing of optical and infrared laser signals [1.1, 1.2, 1.3]. Such applications are of course, motivated by the desire to more fully utilize the large bandwidths afforded by these signals.

In the infrared, control of the $CO_2$ laser is particularly attractive for communications and radar applications because it provides high power densities at 10.6 microns ($\mu$) which is within the $8\mu$ to $14\mu$ atmospheric window [1.4]. Such an Infra Red Detection And Ranging (IRDAR) system proposed by M.E. Pedinoff and employing an acousto-optic modulator provided the impetus for the investigation to be described in this thesis [1.5].

In addition to improvements in the quality of existing materials and the discovery of new materials, the increasing use of acousto-optic devices for beam deflection has been due to the development of new high frequency acoustic techniques. These techniques include the use of thin films of piezoelectrically active materials as the active mediums for electro-mechanical transducers. Unfortunately not all piezoelectrically active materials perform satisfactorily in thin film form. Only those which have a high degree of symmetry and chemical simplicity, such as Zinc Oxide (ZnO), have been successfully employed.

## 1.2 Background

Detection and Ranging systems were developed during the Second World War for military applications. In the post war period their use has been primarily to aid in air and sea navigation. Needless to say, the performance of such systems had to greatly improve in order to keep pace with the rapid development in the aviation industry. Now, with the advent of the space age, another order of magnitude improvement in performance is needed.

Active Detection and Ranging systems transmit a pulse of radiation at a particular frequency and then attempt to detect that portion of the transmitted radiation which has been back-scattered towards the receiver. By measuring the time between transmitting the pulse and receiving the echo, the range or distance of the object from the transmitter can be determined.

If the transmitting and receiving antennae are one and the same, the maximum range is given by the classical diffraction limited Radar equation

$$\xi_{max} = \sqrt[4]{\frac{P_t A_{tr}^2 \sigma_o}{P_{r_{min}} 4\pi\lambda^2}} \qquad (1.1)$$

where $P_t$ = peak transmitted power,

$\sigma_o$ = object cross-sectional area,

$A_{tr}$ = area of transmit-receive antenna,

$\lambda$ = radiation wavelength in a vacuum,

$\xi_{max}$ = maximum range

and $P_{r_{min}}$ = minimum received power which may be unambiguously detected [1.6].

Intuitively it can be seen that the range resolution or the ability of the system to resolve individual objects out of a group of objects is inversely proportional to the pulse duration and beam width [1.7]. From the previous statement and equation (1.1) it can be seen that, for maximum range and resolution, a high energy short duration pulse having a small beam divergence or equivalently a short wavelength is desirable. In addition to these pulse characteristics it is also desirable to have a large receiving antenna area so that more of the reflected signal may be captured. Lastly, but by no means least important, is the requirement for a small minimum detectable signal. The most sensitive detection systems are coherent or heterodyne systems and these are invariably employed in radar systems. In heterodyne detection a high power, local oscillator signal is combined with the low level target signal and the resultant signal is fed into a square law detector. The output of this detector will have a component at the difference frequency which is proportional to two times the product of the target signal and local oscillator signal levels. Thus by increasing the local oscillator signal level the detection sensitivity or signal to noise ratio can be increased allowing lower reflected powers to be detected.

The target velocity may be determined either by measuring the change in range per unit time or by measuring the change in frequency of the reflected radiation due to the Doppler effect. If the second method is employed, the system resolution can be improved since the targets may also be resolved on the basis of their differing radial velocities [1.8]. The Doppler frequency shift and radial velocity are related by

$$\omega_d \simeq \pm 2 \frac{v_t}{c} \omega_c \tag{1.2}$$

where $\omega_d$ = Doppler frequency shift in radians/sec,
$v_t$ = target radial velocity,
$c$ = velocity of light in a vacuum
and $\omega_c$ = carrier frequency in radians/sec [1.6].

Thus, the radial velocity resolution is directly proportional to the carrier frequency. Again the advantage of having a large carrier frequency is apparent.

In a conventional radar system one would find peak pulsed powers of approximately one megawatt at a frequency of 1 GHz with pulse durations in the order of 1 μsec, being used [1.9]. If, on the other hand, $CO_2$ laser radiation ($f = 2.83 \times 10^{13}$ Hz) could be employed, a gigawatt peak pulsed power with a pulse width of 1 nanosecond is available [1.4]. Although the $CO_2$ laser is not the only laser capable of producing such short, high energy pulses, it is the only one which can do so at a wavelength (10.6 μ) where atmospheric attenuation is low (8μ to 14μ window). Clearly, as transmission losses increase, the maximum range decreases. Such a system would, of course, require coherent detection. Such detection in the infrared does not reduce the minimum detectable power relative to the conventional systems and is in fact much more difficult to accomplish due to the stringent alignment requirements. However, if similar values of $P_{r_{min}}$ (per unit bandwidth) can be achieved then the significant improvements in range and resolution due to the 10.6μ transmitter characteristics can be realized.

An infrared system, however, does have several practical limitations. For instance, one would not expect to use such a system in the 'search' mode due to its narrow beam cross-section. Instead, it would have to be used in conjunction with conventional radar which would 'lock' the laser system onto the target. Also, the maximum I.R. detector frequency response, at present, is only 1 GHz. This is certainly adequate for detecting the Doppler shifts due to the velocities of aircraft, however, for space applications several gigacycles of change in frequency may be expected. One method of reducing the requirements on the detector would be to modulate the transmitted beam and thereby translate the Doppler frequency down to a frequency which can be detected. Also, the effect of the necessarily larger receiver bandwidth and concomitant increase in $P_{r_{min}}$ may be somewhat offset by employing a multichannel receiver.

The above discussion can be summarized by stating that an IRDAR system (at 10.6μ) would provide improved range and resolution over conventional RADAR for Doppler-tracking applications. The requirements of such a system are: (1) high energy short duration pulses of high-frequency radiation which do not suffer severe atmospheric attenutation; (2) coherent detection and; (3) facility to frequency modulate the transmitted radiation.

## 1.3 Description of Proposed Heterodyne System

The proposed 10.6μ laser heterodyne system using an ultrasonic frequency translator and deflector as an intracavity element is shown in Fig. 1.1. The motivation for using ultrasonic modulators as intracavity elements stems from the fact that a single frequency travelling ultrasonic wave can produce a pair of oppositely-directed, oppositely-frequency-shifted optical beams whose frequency difference is twice the ultrasonic drive frequency ($\omega_s$) [1.10].

Therefore, the $CO_2$ laser oscillator in Fig. 1.1 not only injection locks the $CO_2$ laser amplifier to a frequency $\omega_c$ but also provides the continuous local oscillator power necessary for heterodyne detection. A portion of the radiation travelling to the right from the frequency stable ($\omega_c$), low power, $CO_2$ laser oscillator is diffracted towards the detector by the ultrasonic modulator. The remainder of the radiation passes through the pulsed, low pressure transversely excited $CO_2$ laser amplifier. During the time this amplifier is pulsed on, this beam will be amplified and a portion thereof, upon returning to the modulator, will be diffracted towards the collimator. Depending upon the pulse width and cavity dimensions mutliple transits may occur in which case a high intensity pulse will also be directed towards the detector. If allowed to reach the detector element such a pulse would destroy it. Detector isolation can be provided by electro-optically scattering the incident radiation pulse. Due to the ultrasonic Bragg diffraction phenomenon the frequency of the beam directed towards the detector will be $\omega_c + \omega_s$ while that diffracted towards the collimator will be $\omega_c - \omega_s$. A single frequency travelling wave is guaranteed by anechotically terminating the

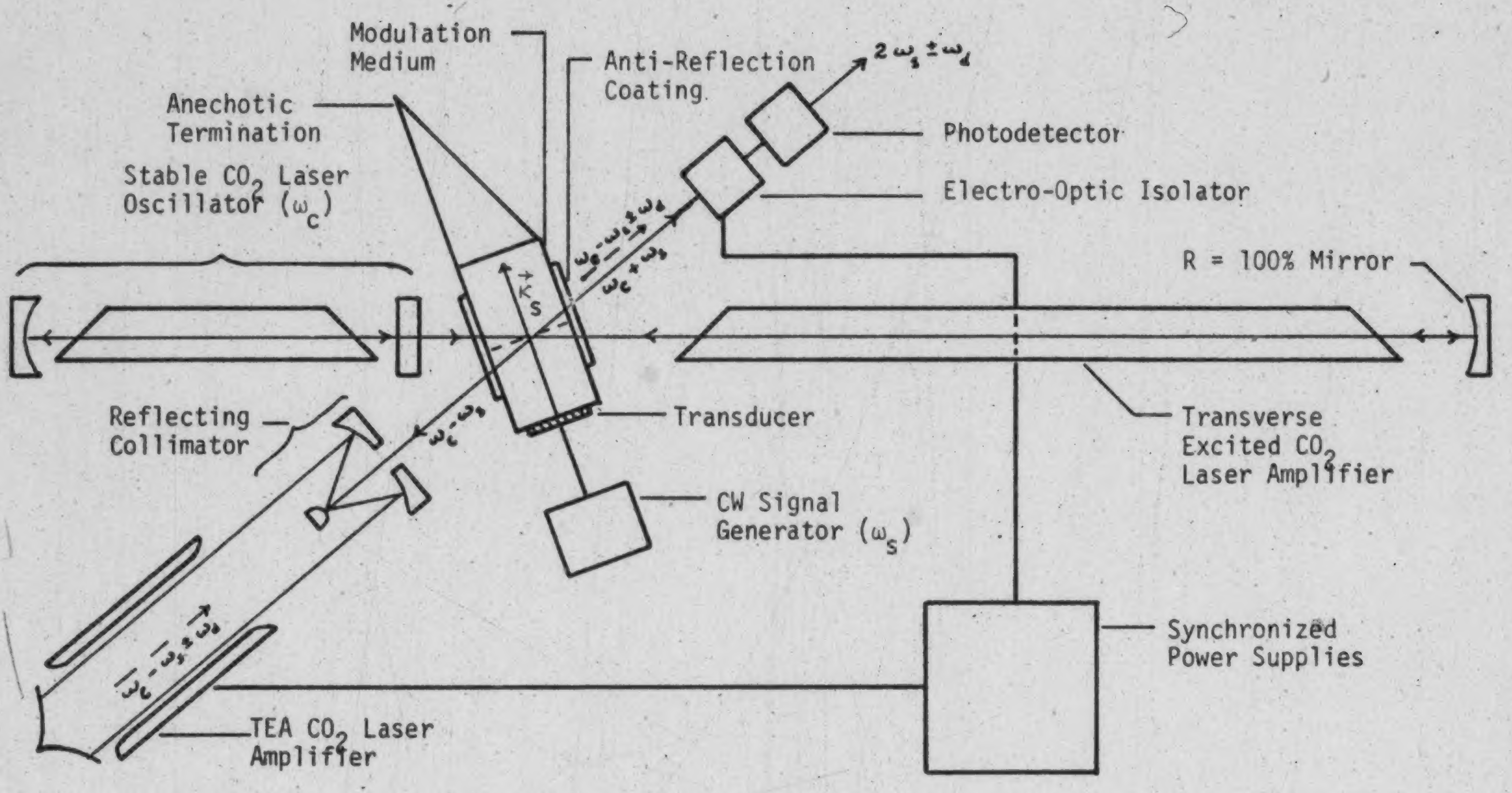
Modulation Medium
Anti-Reflection Coating
$2\omega_s \pm \omega_d$
Anechotic Termination
Photodetector
Stable $CO_2$ Laser Oscillator ($\omega_c$)
Electro-Optic Isolator
$\overline{\omega_c} - \overline{\omega_s} \pm \omega_d$
$\omega_c + \omega_s$
$\vec{K}_S$
R = 100% Mirror
$\omega_c - \omega_s$
Reflecting Collimator
Transducer
Transverse Excited $CO_2$ Laser Amplifier
CW Signal Generator ($\omega_s$)
$\overline{\omega_c} - \overline{\omega_s} \pm \omega_d$
Synchronized Power Supplies
TEA $CO_2$ Laser Amplifier

Fig. 1.1 Proposed 10.6μ Heterodyne System Employing an Intracavity Acousto-Optic Modulator.

acoustic beam after it has traversed the modulating medium. If the downshifted beam encounters a moving object it will be scattered and Doppler shifted in frequency to $\omega_c - \omega_s \pm \omega_d$. A small portion of this radiation will be reflected 'normally' and will therefore be parallel with the local oscillator beam upon entering the detector. This is extremely important for heterodyne detection. Depending on the system range specifications, a high pressure, TEA $CO_2$ laser may be used to further amplify the target signal (see Fig. 1.1).

In a solid state photodetector the change in current is proportional to the square of the total electric field intensity at the detector. Therefore, when two waves differing in frequency by $\omega_{if}$ and having an angle $\theta$ between their directions of propagation, are incident on a detector of surface area $A_d$, the signal current ($i_s$) at the difference frequency is given by

$$i_s(\omega_{if}) = A_d E_s E_{LO} \cos(\omega_{if} t) \frac{\sin\left[\frac{2\pi \sin\theta \, \ell_d}{2\lambda}\right]}{\frac{2\pi \sin\theta \, \ell_d}{2\lambda}} \qquad (1.3)$$

where $\omega_{if}$ = $2\omega_s \pm \omega_d$ = information frequency,

$\omega_s$ = ultrasonic drive frequency in radians/sec

$E_s$ = electric field intensity of the low level signal,

$E_{LO}$ = electric field intensity of the local oscillator signal,

and $\ell_d$ = linear dimension of the detector in the direction defined by the intersection of the plane of incidence with the detector surface [1.11].

This is the fundamental equation of photomixing or heterodyne detection. From equation (1.3) it can be seen that heterodyne detection not only provides a method of considerably increasing the receiver sensitivity by increasing $E_{LO}$ but also, it permits translation of the Doppler-shifted radiation signal down to some convenient information frequency ($2\omega_s \pm \omega_d$) for precise filtering of the Doppler information.

Also, as can be seen from equation (1.3), the signal current is critically dependent on $\theta$, being a maximum for $\theta = 0$. For instance, when $\theta = 3.2\text{x}10^{-3}$ degrees and $\ell_d = 1$ mm, the signal current has already been reduced to 84% of its maximum value. This is indeed a stringent colinearity restriction. In the proposed system, however, this problem is overcome for all modulation frequencies by virtue of the fact that the two acousto-optically diffracted beams are always parallel due to the symmetrical nature of the ultrasonic Bragg diffraction phenomenon.

Thus, not only has the intracavity ultrasonic modulator supplied the necessary beam colinearity but it has also reduced by a factor of 2, the required $\omega_s$ for a specified $\omega_d$. This becomes significant when the ultrasonic attenuation in solids at room temperature is considered. For example, as shown in Chapter IV, the attenuation in single crystal germanium at 300°K is already 5 db/cm for 500 MHz compressional waves propagating in the <111> direction. Since operation at a single frequency is required in this system the main design specification placed on the transduction system is one of maximum efficiency at $\omega_s$. The required acoustic bandwidth is an important specification which must be considered when choosing the transducer active medium, since the available acoustic bandwidth is proportional to the square of the active medium coupling coefficient. Therefore, a large bandwidth requirement could force the use of a thin, single crystal plate for the transducer active medium. Such transducers are technologically difficult to fabricate, as will be discussed in Chapter II. With some modification this proposed system may be used as a bilateral Doppler compensated space communications link. In such a system, the frequency transmitted by the stationary station is $\omega_c - \omega_d - \omega_{if}$ so that the frequency of the signal received in the moving station is $\omega_c - \omega_{if}$. By heterodyning with a local oscillator $\omega_c$, the signal having the proper information center frequency, $\omega_{if}$, is received. Conversely, the signal transmitted by the station in motion will be at $\omega_c$. The frequency of this signal at the stationary station will be $\omega_c + \omega_d$ and, therefore, it will have to be heterodyned with a frequency at $\omega_c + \omega_d + \omega_{if}$ to provide the signal centered at the difference frequency of $\omega_{if}$. However, in this system the ultrasonic drive frequency $\omega_s = \pm (\omega_d + \omega_{if})$ will have to be variable and gain-bandwidth considerations will become important.

Finally, it should be mentioned that the system proposed has been designed utilizing guidelines formerly reserved for the microwave region of the electromagnetic spectrum. As DeMaria has stated, this is possible because the $CO_2$ laser is presently the only laser that can be designed so as to optimize its performance as either a stable-frequency master oscillator, power oscillator, low noise-high gain preamplifier, or an intermediate-or-high-power amplifier [1.4].

Clearly the feasibility of such a system hinges on the efficiency of the ultrasonic frequency-translator and beam-deflector. Such an acousto-optic modulator consists of an electromechanical transducer attached to a modulation medium which has antireflection (A.R.) coated faces perpendicular to the direction of propagation of the infrared beam.

The high frequency transducer consists of a thin layer of high resistance, piezoelectrically active material between two metal electrodes. The bottom or counter-electrode is attached to the modulation medium. The required transducer frequency will be determined by either the frequency response of the detector or the acoustic losses in the modulating medium. To prevent time varying diffracted beams the acoustic beam should be anechotically terminated and a reduction of acoustic and electromagnetic losses can be accomplished by cooling the modulation medium.

The development of such a modulator is the subject of this thesis.

## 1.4 Present Work

The maximum detectable modulation frequency in infrared solid state detectors is at present ∿ 1 GHz. In Chapters IV and V, the superiority of germanium as an acousto-optic modulator material at 10.6μ is referenced. It is shown that in germanium the maximum diffraction efficiency occurs when the electromagnetic wave is polarized in the <111> direction and interacts with a <111> directed ultrasonic compressional wave. Also, the ultrasonic attenuation in germanium is shown to limit its use to frequencies below 500 MHz. Therefore, in Chapter II the fabrication of thickness dilatational transducers having a resonant frequency of 400 MHz is discussed. The basis for employing a thin film of Zinc Oxide (ZnO) as the active medium is given and the methods of deposition considered. A detailed description of the Triode sputtering system constructed is also presented.

Chapter III deals with the effect of the deposition parameters on the orientation of the crystallites in the ZnO films. The effect of the partial pressure of oxygen in the sputtering gas mix and the crystalline state of the nucleating gold thin film are shown to have considerable influence on the structure of the ZnO thin films. Also presented in this chapter are the results of the non-structural investigations performed on the films. The films are shown to have resistivities greater than $10^6 \Omega$-cm, relative dielectric constants of 8.5, refractive indices in the 2.5μ to 10μ region of 2.1 and band gap energies of 3.2 ev.

In Chapter IV a detailed description of the transducer fabrication process is presented and the details of the acoustic investigation are given. A mathematical model suitable for computer programming, and simulating a ZnO thin film transducer acoustically radiating into single crystal germanium was developed and is outlined. Implementation of this theory requires correcting the experimental data for acoustic losses. The procedure for determining these losses and the results are given. In particular the intrinsic attenuation data for a longitudinal acoustic wave propagating along the <111> axis in Germanium at 300°K is determined. By comparing the experimental and computed insertion loss data, a value of $k_t$ (electromechanical coupling coefficient) greater than or equal to 90% of the ZnO bulk value is obtained for the active ZnO thin films produced.

The acousto-optic performance of the modulator is given in Chapter V. The necessary theory for Bragg regime diffraction is outlined. The experimental results and theory are compared and the correlation is shown to be excellent. The effective photoelastic constant of germanium evaluated is $P'_{33}$, corresponding to radiation polarized in the <111> direction interacting with a <111> directed dilatational acoustic wave. The value of $P'_{33}$ obtained in this investigation was found to agree with that determined elsewhere [1.12]. It is felt that this agreement lends considerable credibility to the techniques described and conclusions made in this thesis.

# CHAPTER II

# THE ACTIVE MEDIUM AND FABRICATION SYSTEM

## 2.1 Introduction

In addition to its elastic, dielectric, and piezoelectric constants, a real transducer material has other properties which are not easily specified by numbers. The choice of the fabrication technique is dictated by these properties.

In the following section it will be shown that for efficient high frequency thickness dilatational transducers the requirements on the physical constant are; a piezoelectrically active medium having a thickness of less than ten microns, a large coupling coefficient, $k_t$, and a small relative dielectric constant, K. The effect of the transducer size on the choice of the fabrication technique is referenced. In these references it is suggested that for high frequency transducers, at present, single crystal plates are superior when acoustic beams of small cross-sectional areas (diameter $\leq$ 2 mm) are required whereas, thin film transducers are superior for generating large area ($\sim .5$ cm$^2$) acoustic beams. This is due to the difficulties encountered when bonding and lapping single crystal plates which are uniform over large areas. Since large area transducers are needed for high acousto-optic diffraction efficiences one is limited to thin film techniques. On the basis of its superior bulk physical constants Zinc Oxide (ZnO) was selected for deposition.

In the third section of this chapter the possible methods of depositing ZnO are discussed, and a general description of a triode sputtering system is given. The system which was constructed is described in detail in Sections 2.3.4 and 2.3.5. The chapter is followed by a discussion and conclusion.

## 2.2 Choice of Active Medium Material

Table 2.1, taken from Meitzler, lists all (up to 1969) the piezoelectric and ferroelectric materials of practical interest for high-frequency transducers for which a substantial amount of information is known [2.1]. All the parameters required for the equivalent circuit analysis are presented.

The first column designates the material by its nominal chemical formula, except in the case of the ceramic compounds which are designated by their trade names. The point-group categorization of the material, in Hermann-Mauguin symbols, is presented in parenthesis. The symbols [D] or [S] indicate whether the information on a given line applies to thickness-dilatational or thickness-shear transducers. The second column indicates the orientation required for a layer of the material to operate in the mode indicated. The third column presents the 'effective' value of the electromechanical coupling coefficient, $k_t$, applicable for the mode of vibration indicated. This constant is related to the portion of electrical energy which will be transformed into mechanical energy. K, the 'effective' relative dielectric constant is presented in the fourth column. The fifth column lists the value of the frequency constant for what is conventionally termed the 'parallel resonance frequency, $f_0$', which is the frequency at

Table 2.1 Materials for High-Frequency Piezoelectric Transducers (ca. 1969)

| Material (point group) [Mode] | | Orientation | Coupling factor, $k_t$ | Relative dielectric constant, K | Frequency constant $f_o \cdot d = \frac{v}{2}$ MHz·μm | Mechanical impedance $Z_o = \rho v$ $10^6$kg/s·m$^2$ | Reference |
|---|---|---|---|---|---|---|---|
| Piezoelectric materials | | | | | | | |
| Single crystals | | | | | | | |
| $SiO_2$ (32) | [D] | X | 0.098 | 4.58 | 2850 | 15.1 | 2.15 |
| | [S] | Y | 0.137 | 4.58 | 1925 | 10.2 | |
| | [S] | AC | 0.083 | 4.58 | 1650 | 8.8 | |
| $LiGaO_2$ (mm2) | [D] | Z | 0.30 | 8.5 | 3130 | 26.2 | 2.16 |
| | [S] | X | 0.17 | 7.0 | 2550 | 21.4 | |
| | [S] | Y | 0.17 | 6.0 | 2900 | 24.2 | |
| $Bi_{12}GeO_{20}$ (23) | [D] | (111) | 0.155 | 38 | 1670 | 30.6 | 2.17 |
| | [S] | (110) | 0.235 | 38 | 850 | 15.6 | |
| $LiIO_3$ (6) | [D] | 0° | 0.51 | 6 | 2066 | 18.5 | 2.18 |
| | [S] | 90° | 0.60 | 8 | 1260 | 11.3 | |
| Films | | | | | | | |
| CdS (6mm) | [D] | 0° | 0.154 | 9.53 | 2750 | 21.7 | 2.19 |
| | [S] | 90° | 0.188 | 9.02 | 900 | 8.69 | |
| | [S] | 39.7° | 0.212 | 9.33 | 1050 | 10.2 | |
| ZnO (6mm) | [D] | 0° | 0.282 | 8.84 | 3200 | 36.4 | 2.19 |
| | [S] | 90° | 0.259 | 8.33 | 2880 | 16.4 | |
| | [S] | 43.0° | 0.322 | 8.63 | 1620 | 18.4 | |
| AlN (6mm) | [D] | 0° | 0.20 | 8.5 | 5200 | 34.0 | 2.20 |

Table 2.1 (continued)

| Material (point group) | [Mode] | Orientation | Coupling factor, $k_t$ | Relative dielectric constant, K | Frequency constant $f_o \cdot d = \frac{v}{2}$ MHz·µm | Mechanical impedance $Z_o = \rho v$ $10^6$kg/s.m$^2$ | Reference |
|---|---|---|---|---|---|---|---|
| Ferroelectric materials | | | | | | | |
| Poled ceramics | | | | | | | |
| MBT (6mm) | [D] | 0° | 0.30 | 395 | 2880 | 31.3 | 2.21 |
| | [S] | 90° | 0.30 | 365 | 1700 | 18.4 | |
| PZT-5 (6mm) | [D] | 0° | 0.49 | 635 | 2170 | 33.4 | 2.22 |
| | [S] | 90° | 0.69 | 730 | 1120 | 17.3 | |
| SPN (6mm) | [D] | 0° | 0.46 | 310 | 3470 | 31.3 | 2.23 |
| | [S] | 90° | 0.65 | 545 | 1880 | 16.9 | |
| PZT-7A (6mm) | [D] | 0° | 0.50 | 235 | 2400 | 33.8 | 2.21 |
| | [S] | 90° | 0.67 | 460 | 1250 | 17.6 | |
| Single Crystals | | | | | | | |
| $LiNbO_3$ (3m) | [D] | Z | 0.17 | 29 | 3660 | 34.4 | 2.24 |
| | [D] | 35°Y | 0.49 | 39 | 3700 | 34.8 | |
| | [S] | 163°Y | 0.62 | 43 | 2280 | 21.4 | |
| | [S] | X | 0.68 | 44 | 2400 | 22.3 | |
| $LiTaO_3$ (3m) | [D] | Z | 0.19 | 43 | 3040 | 45.3 | 2.24 |
| | [D] | 47°Y | 0.29 | 42 | 3700 | 55.1 | |
| | [S] | 165°Y | 0.41 | 41 | 2280 | 34.0 | |
| | [S] | X | 0.44 | 41 | 2100 | 31.3 | |
| $Ba_2NaNb_5O_{15}$ (mm2) | [D] | Z | 0.57 | 32 | 3075 | 32.6 | 2.25 |
| | [S] | X | 0.21 | 222 | 1820 | 19.3 | |
| | [S] | Y | 0.25 | 227 | 1830 | 19.4 | |

which the transducer thickness is equal to half the acoustic wavelength. The numbers in the last column refer to the mechanical impedance of the transducer material.

Since a maximum transduction efficiency is the prime design specification to be met, an active material having a large coupling coefficient, a mechanical impedance approximately equal to that of germanium and a low relative dielectric constant is necessary. It can be seen by definition, that a large coupling coefficient is advantageous. Because the transducer and modulator medium constitute an acoustic generation and transmission network their mechanical impedances should be matched for maximum acoustic power transfer. The requirement for the lowest possible material dielectric constant follows from the capacitive nature of the transducer. To reduce the capacitive loading, the transducer impedance should be as close as possible to 50Ω. As shown below, due to the required transducer physical dimensions, a 50Ω impedance necessitates a value of K less than unity. Since this is impossible an impedance matching network will have to be employed. The matching requirements of this network will depend upon the impedance mismatch which should therefore be kept as small as possible.

As stated in Chapter I, the transducer consists of a high resistance material between two conducting electrodes. Therefore, electrically it is simply a capacitor whose impedance is given by

$$|Z| = \frac{d}{2\pi f \, K\varepsilon_0 S} \,, \tag{2.1}$$

where d = thickness of active medium,

f = frequency,

$\varepsilon_0$ = permittivity of free space and S = top electrode area.

Since a transducer operates most efficiently at or near $f_o$, and because frequencies above 300 MHz are being considered, the required transducers will be less than 10μ thick. Also, as shown in Chapter V, areas in the order of 1 $cm^2$ are required for sufficient acousto-optic diffraction efficiencies. Using these values and solving for K in equation (2.1) one finds the relative dielectric constant should be .12. For increased frequencies this value will be lower. In this case, the need for a material dielectric constant close to unity will be even more acute.

Based upon the above considerations,from Table 2.1 $Ba_2NaNb_5O_{15}$ appears to be the best choice since it has the highest thickness dilatational coupling factor and a relative dielectric constant less than 50. However, as referenced below, large, high frequency transducers using lapped and bonded single-crystal active mediums are technologically very difficult to produce.

Investigations have been performed using bonded and subsequently lapped signle-crystal plates as transducers for signal processing applications requiring 3 db bandwidths of a few hundred megacycles with a center frequency up to 500 MHz [2.2, 2.3, 2.4]. The bandwidth requirements demanded coupling coefficients of approximately .5 and small area top electrodes to provide a 50Ω capacitive impedance. Even with these small areas (diameter ∿ 1mm ) the bonding problems were extremely involved [2.2]. For example, epoxy bonding requires a "built-in" interferometer to be incorporated into the transducer-bond-substrate since a thickness of only one-one hundredth of an acoustic wavelength can be tolerated. This is because the specific mechanical impedance of epoxies is low relative to other solid materials. In the case of indium bonding techniques, there are three thin films involved in the bond as well as a requirement for precision pneumatic (1,000 to 10,000 psi) pressing under vacuum of the two overlaid surfaces. After bonding the crystal plates must be uniformly lapped or sputter machined. Meitzler states, "The achievement of transducer layers with lateral dimensions of several mm and thicknesses of several μm, requires elaborate means to measure and maintain alignment of surfaces with high angular precision of the order of ± 5 sec of arc" [2.5]. In view of the above discussion it is not surprising that Warner states, "thin film transducers continue to have advantages, particularly for applications involving frequencies in excess of 1 GHz or for applications involving extended areas or curved surfaces" [2.3].

Since large area transducers are necessary for high diffraction efficiency acousto-optic modulators one is therefore, finally limited to selecting the best thin film material. Returning to Table 2.1, ZnO is the obvious choice. The ultimate success of this trade-off between coupling coefficient and bonding layer loss, will of course depend upon the degree of perfection obtainable in the thin films and their power handling capabilities.

## 2.3 Thin Film Deposition System

The capability of independently controlling as many of the system parameters as possible should be possessed by any prototype fabrication system. In the case of a thin film deposition system, independent control over all of the deposition parameters is virtually impossible. However, systems which approach this objective more closely than others can be constructed but at a cost of increased complexity.

### 2.3.1 Choice of Deposition System

Thin film preparation can be broadly divided into two classes; one which depends upon the physical ejection of material from a source and a second which depends on a chemical reaction.

Since the chemical method by definition, involves a chemical reaction, it is unsuitable for the present multi-layer application. The reaction processes available restrict the choice of substrate and materials which may be deposited. Due to this lack of universality, the choice of thin film preparation was therefore limited to a method within the physical ejection class. Two distinct processes are included in this class; evaporation and sputtering.

Compounds may be directly deposited in an inert atmosphere or in a reactive atmosphere in which one or more of the elements of the compound are intentionally introduced into the vacuum chamber. The direct evaporation of ZnO is very difficult because first, ZnO is refractory, having a melting point of 1975°C and second, there is a considerable difference in vapor pressures of the two components. Reactive evaporation, where zinc is evaporated in an oxygen atmosphere is possible and has been attempted with limited success relative to that obtained by sputtering [2.6].

If the ejection of material is due to positive-ion bombardment, it is referred to as 'cathodic sputtering'. This is the most inexpensive and widely used method of sputtering because the ions may easily be supplied by a plasma discharge.

In a diode sputtering system, the discharge may be generated between two electrodes one of which, the cathode, is composed of the material to be sputtered. In this system the sputtering parameters cannot be varied independently, and pressures generally greater than approximately thirty microns are necessary for a stable glow discharge. Due to this lack of flexibility such systems are usually constructed for depositing materials whose general deposition characteristics have been determined in a more experimentally oriented triode sputtering system.

Therefore, due primarily to its greater experimental flexibility a system having a triode configuration was constructed for ZnO thin film transducer fabrication.

### 2.3.2 The Sputtering Process in a Triode System

The basic components and their relative orientation in a triode sputtering module are shown in Fig. 2.1, [2.7]. The plasma is formed independently as the positive column of a discharge maintained between a thermionic cathode and an anode. If the material to be sputtered is not a dielectric, sputtering is accomplished by inserting the target in this plasma as a separate negative electrode. In the case of a dielectric R.F. must be used on the target electrode. In the case considered here where ZnO, a semiconductor, was sputtered the main advantage of incorporating a thermionic cathode is that even without a magnetic field a plasma can be maintained at much lower gas pressures (low millitorr region) than in a d.c. glow discharge.

An adequate description of the processes which take place at a target in contact with a low-gas-pressure plasma is furnished by Langmuir's probe theory. The plasma has such high electrical conductivity that a voltage applied to a probe or target does not result in field changes throughout the whole column but only in the immediate vicinity of the probe. When a negative voltage is applied with respect to the plasma (or with respect to the anode since anode potential is usually close to plasma potential), the plasma electrons in the electrode vicinity are repelled, a positive ion sheath is formed through which the ions stream from the plasma toward the electrode. The major part of this voltage drop is localized in this sheath. The current density to

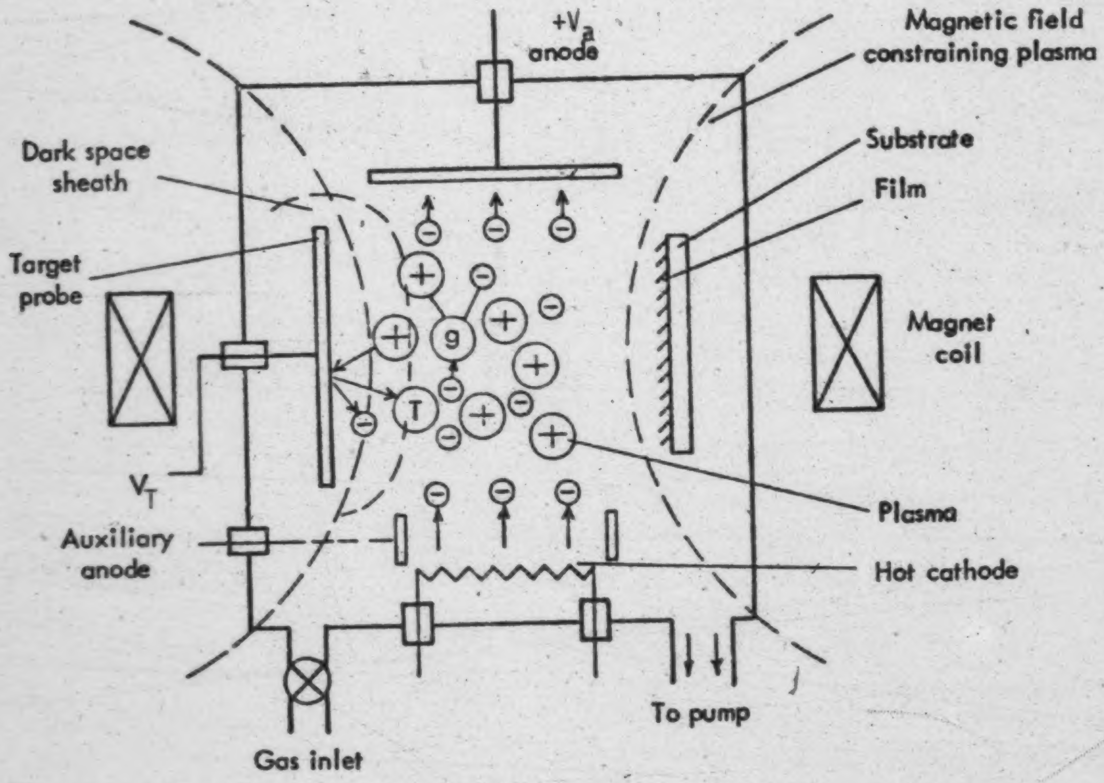

Auxiliary anode sometimes used as this renders target ion current less dependent on ionization conditions.

Pressure range $\simeq 5 \times 10^{-4} - 10^{-2}$ torr
Target voltage $\simeq$ 1 - 2 kV
Anode voltage $\simeq$ 0.2 - 0.5 kV

Fig. 2.1 Low Pressure Sputtering or Triode System.

the target is related to the applied potential and sheath thickness by Langmuir's space-charge equation

$$j^+ = \frac{4}{9}\varepsilon_o\left[\frac{2e}{m^+}\right]^{1/2}\frac{V_T^{3/2}}{d_{sh}^2} \tag{2.2}$$

where $j^+$ = ion current density drawn by probe,

$e$ = electronic charge,

$m^+$ = mass of ion,

$V_T$ = probe potential

and $d_{sh}$ = sheath thickness [2.8].

This is the usual equation used to describe the current voltage relationship in a standard, space charge limited electronic tube. However, in our case the source of charged particles is the positive column and is therefore limited by the number of ions incident on a unit area per unit time as given by

$$j^+ = e\,n^+ = \frac{I^+}{A_T}\ , \tag{2.3}$$

where $n^+$ = number of ions incident on a unit area per unit time,

$A_T$ = effective area of target, that is, the target sheath area which depends upon $d_{sh}$

and $I^+$ = target ion current.

From kinetic theory

$$n^+ = \frac{\rho^+ \nu^+}{4} \tag{2.4}$$

where $\rho^+$ = ion density in the glow discharge

and $\nu^+$ = the average random velocity of the ions [2.9].

Note, there will be little spread in $\nu^+$ because the ion temperature is not much higher than the gas temperature.

From equations(2.3) and (2.4) the current density to the target is constant for a particular plasma density which in turn depends on the pressure and anode potential. Also, as $V_T$ is increased, the sheath thickness increases causing an increased effective area. This permits a coarse adjustment of target current and deposition rate.

### 2.3.3 General Characteristics of a Triode Sputtering System

#### Low Pressure Operation

By operating at gas pressures where the mean free path of ions and sputtered atoms becomes comparable with or larger than the ion-accelerating region or the chamber dimensions, one reduces or eliminates many of the complications inherent in glow discharges (diode sputtering). Some of these complications are; diffusion of sputtered material back to the target, poorly defined bombarding ion energies and angles of incidence, as well as charge-exchange effects in the ion-accelerating region. The last effect is due to the fact that an ion moving in its own gas has a relatively high probability of transferring its charge to a neutral atom. After the transfer, the neutral, which was formerly the ion, continues with the momentum which it possessed prior to charge transfer while the newly formed ion has only thermal energy. If this effect is severe, most of the ions and neutrals which reach the cathode will have essentially zero energy resulting in much lower sputtering yields [2.12].

The mean free path of a gas molecule is given by

$$\text{M.F.P.} = \frac{K_B T^\circ}{\sqrt{2}\pi \S^2 P_T} \qquad (2.5)$$

where M.F.P. = mean free path of gas molecule,

$K_B$ = Boltzmann's constant,

$T^\circ$ = absolute temperature in °K,

$\S$ = molecular diameter,

and $P_T$ = total gas pressure [2.10].

Using this formula, with $P_T = 5\mu$ of Argon, § ave. = 3.25 and $T^\circ = 373^\circ$K, a mean free path of 1.65 cm is obtained [2.11].

There is, however, at least one disadvantage to operating at low pressures, namely the entrapment of inert gas impurities in films during deposition. The fraction of impurity species trapped in a film is given by

$$f_i = \frac{\alpha_i N_i}{\alpha_i N_i + D_R} \qquad (2.6)$$

where $N_i$ = number of atoms of species i incident per unit area per unit time,

$f_i$ = fraction of impurity species i trapped,

$\alpha_i$ = effective sticking coefficient of the species i,

and $D_R$ = deposition rate [2.12].

It has been shown that for inert gases having thermal energies, $\alpha_i$ is effectively zero but also that if their energies were greater than

100 ev. $\alpha_i$ approached unity [2.13, 2.14]. This energy was presumed to be sufficient to drive the argon atoms into the surface, where they would then be held. Since some energetic neutrals will be reflected from the target, due to charge exchange for example, progressively fewer of these will arrive at the substrate with energies greater than 100 ev as the pressure is increased. Therefore, provided the use of high pressures for sputtering does not of itself lead to the presence of excess impurities, the purest films are obtained by sputtering at higher pressures.

## Configuration

Since the discharge is fed and maintained by the electrons released from the thermionic cathode whatever happens at the target in a triode system is unimportant for maintaining the plasma. One is therefore free to select the bombarding-ion energy even down to very low energy independent of the other parameters like discharge current or gas pressure. Also, one can regulate the bombarding-ion current density independently by controlling the main discharge current. This, of course, is conducive to a better understanding of the basic sputtering process as well as experimental flexibility. An excellent example of the latter point is the increasing use of systems having the triode configuration for selective surface etching and implanting foreign ions in solids to modify their surface layers; that is, essentially using the system in reverse.

There are, however, at least two disadvantages to this system configuration. First, it is difficult to provide uniform films over extended areas; and second, such a system is more cumbersome to build and operate than its diode counterpart.

### 2.3.4 The Deposition System Constructed

The transducer fabrication system constructed is shown schematically in Fig. 2.2 and photographically in Fig. 2.3.

The nucleus of the system was a six inch diameter, six arm glass cross, which was mounted on a 1000 litre per second Carl Herman Associates high vacuum pumping station. Although the module was not bakeable, base pressures of $5\times10^{-7}$ Torr, as measured on an N.R.C. cold cathode ionization gauge, were easily obtained when the Meissner trap, located in the chamber, was cooled down to ∿ 130°K. For pressures greater than .5μ a precision M.K.S. capacitance manometer pressure gauge was used so that the sputtering gas mix could be more accurately monitored and controlled. The substrate table temperature could be raised to 450°C. Also included in the system was a three element target changer assembly so that three separate materials could be sputtered at will, without breaking the vacuum.

### Chamber Cold Trap

A Meissner type of cold trap was chosen because it could be cycled very rapidly. This is necessary if the substrate is to be removed from the vacuum chamber within 30 to 60 minutes after deposition termination. If the chamber were to be opened immediately after deposition was completed and the chamber trap was still pumping, then it would become saturated with the condensable vapors from the atmosphere. This of

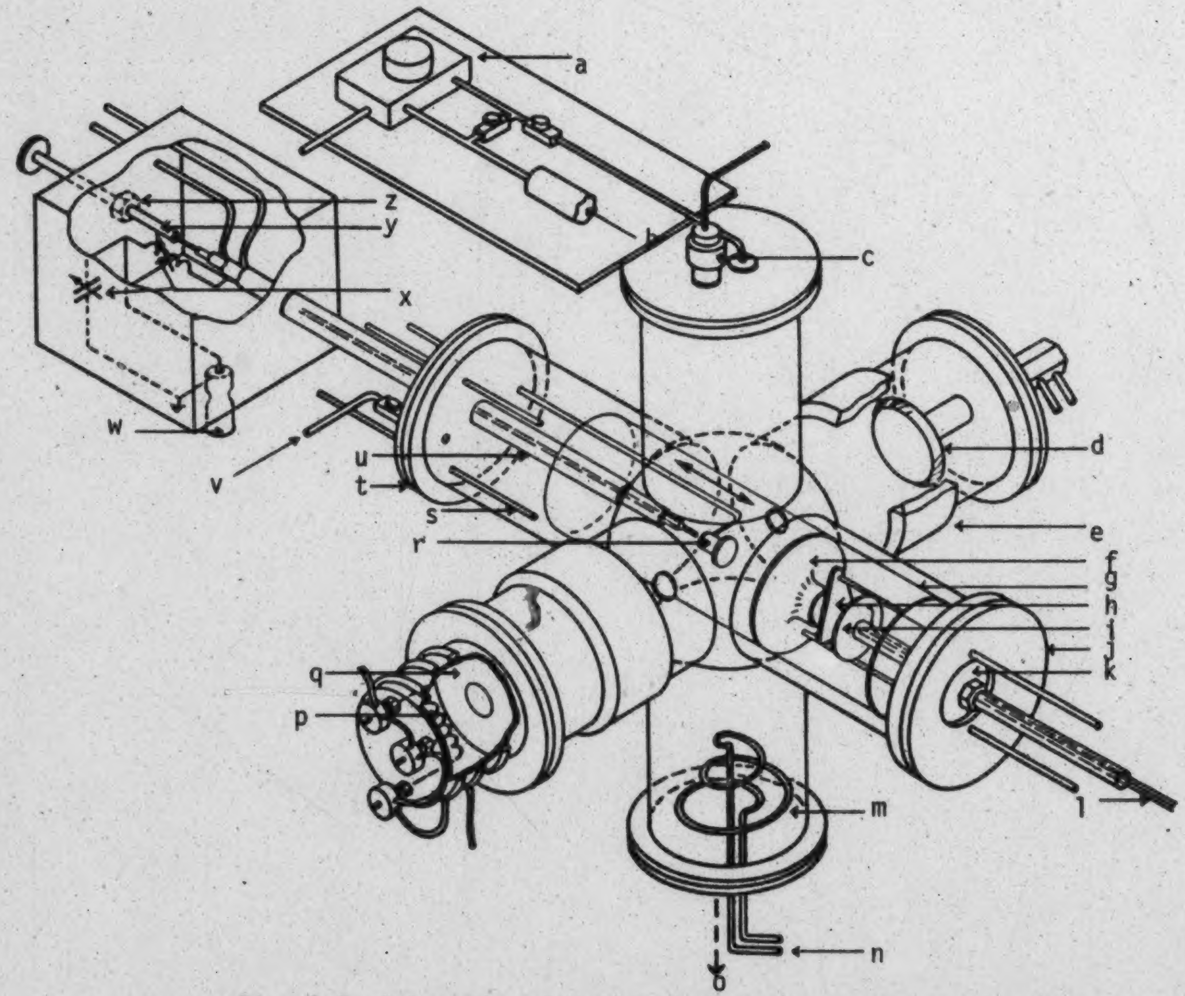

Fig. 2.2 Schematic of Triode Sputtering Module Developed.

Legend to Figure 2.2

a - Capacitance manometer pressure head
b - To reference high vacuum
c - Cold cathode ionization gauge
d - Water cooled anode
e - Magnet coil
f - Pyrex target shield
g - Chamber shield
h - Presputtering shield
i - Substrate table
j - Substrate arm vacuum plate
k - Insulating glass feedthrough plate
l - Electrical connections (thermocouple, heater)
m - Meissner cold trap
n - Liquid nitrogen
o - To diffusion pump
p - Dual filaments
q - Filament shield
r - Sputtering target
s - Target changing arm
t - Probe arm vacuum plate
u - Coaxial probe (cooled, R.F. or D.C.)
v - Gas inlet from mixing manifold
w - R.F. or D.C. connector
x - R.F. matching network
y - Insulated target drawbolt
z - Drawbolt nut

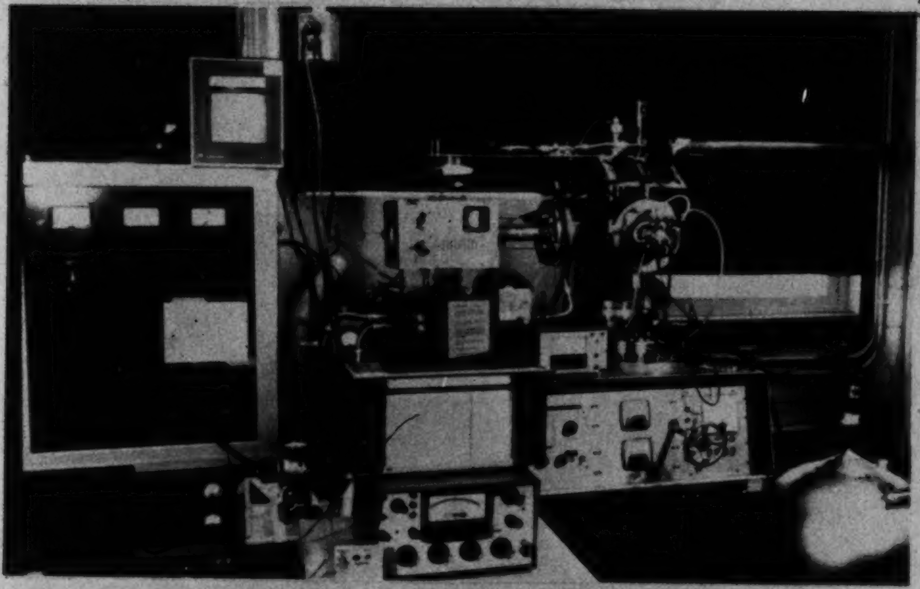

Fig. 2.3 Photograph of Triode Deposition System Constructed.

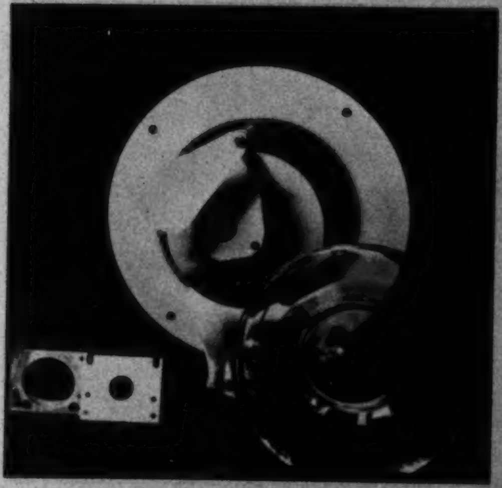

Fig. 2.4 Substrate Arm Vacuum Plate; Substrate Table, Masks and Holder; Presputtering Shield; Target Shield.

Fig. 2.5 View of Targets During Operation.

course would contaminate the system for the subsequent runs.

The pipe array was cooled, when its pumping action was required, by forcing cold nitrogen gas through it. This was supplied from a pressurized dewar (evident in Fig. 2.3) with the efflux going into the surrounding atmosphere. The temperature of the efflux was monitored and kept at about -140°C. Rapid warm-up of the trap prior to atmospheric exposure was achieved by forcing dry gas under pressure through it.

A heating element was situated on the transfer tube at the junction of the pressure release valve and pressurizing gas inlet. Besides preventing the pressure release valve from freezing, this element allowed coarse temperature regulation of the nitrogen gas. This was necessary to prevent the sputtering gases from condensing. Oxygen liquifies at 90°K and Argon at 86°K.

The trap was located in the pumping arm and shaped in the form of a conical helix. The trap, therefore, offers a large surface area and a low molecular conductance path between the deposition chamber and the high vacuum region. Thus, both condensable vapors from the deposition chamber and backstreaming oil vapors migrating into the chamber are effectively trapped. Although, some throttling was provided by this trap, a mechanical throttle was still found necessary.

## Pressure Measurement

The accurate control of the partial pressures of the gases used in the chamber during deposition, as will be shown, was of the utmost importance. During the investigation ionization, thermocouple and pirani gauges were tried, however, all showed an intolerable dependence upon the gas species present. The M.K.S. capacitance manometer vacuum gauge, however, is species independent and proved to be adequate. This gauge measures the change in capacitance resulting from the deflection of a membrane which separates a constant pressure (high vacuum) reference chamber and the unknown pressure chamber. The complete measuring head is temperature controlled for added stability. The pressure is directly measured from the number of molecular collisions per unit area per unit time and is not dependent upon a property peculiar to the gas such as thermal conductivity or ionization potential. Corresponding to a pressure of 5 microns as measured on the M.K.S. gauge, the pressure inside the main chamber shield was 4.2$\mu$. The pressures specified in this thesis were taken directly from the M.K.S. capacitance manometer readout.

It should be noted, however, that the ideal measurement system would consist of a species independent gauge used in conjunction with flow meters on each of the gas input lines. This is because, in a flowing system the true partial pressures, which are the significant parameters, can only be determined if the pumping speeds of the individual gases as well as their respective throughputs are known. As implied, all gases are in general not pumped equally. This can be due to the pump itself but also due to selective getter pumping by the vacuum chamber walls, filaments or in the case of a thin film deposition system, by the freshly deposited films. In this latter situation an accurate determination of the individual pumping speeds is difficult. Thus, in a dynamic system the best alternative is to specify the mass flow of the individual gases and the total pressure together with a schematic of the system showing in particular the location of the vacuum gauge, as well as the system volume and internal structure. The partial pressure measurements given later in the thesis should, therefore, not be considered as absolute.

## Gas Introduction System

The pure gases, Argon (99.999%) and Oxygen (99.997%) were introduced into the system through a pyrex mixing manifold. The 'mixed' gas inlet was located on the probe arm vacuum plate. Due to the position of the target shield during deposition the gas was forced to flow through an annular area surrounding the target. It should be noted that industrial grade gases were tried. In this case the Meissner trap became visibly covered with condensed vapors within 30 minutes.

## Anode

The anode was simply an aluminum disc with rounded front edges mounted onto a water cooled, insulated feedthrough.

## Filaments

The coiled (∿ 3 loops) filaments consisted of two strands of .020 inch tungsten wire twisted together. When run at 45 amps in a pure argon atmosphere they had a lifetime of approximately 1500 minutes. However, in a 60% - 40%, $O_2$ - Ar atmosphere their lifetime was reduced to approximately 150 minutes. Since ZnO deposition times of ∿ 250 minutes were required, dual filaments were installed. The filaments were mounted on insulating, water cooled feedthroughs. The filament chamber was provided with a tantalum shield having a center aperture 2 inches in diameter. In this way, the system contamination from the filaments was reduced and, at the same time the electron source was effectively centralized.

### Electromagnets

In order to confine and further centralize the discharge two cylindrical electromagnets were mounted as shown in Fig. 2.2. Plasma confinement, of course, allows stable discharges to be operated at low pressures. In this sytem, sputtering was possible at pressures less than $5 \times 10^{-4}$ Torr with an anode potential of approximately 100 volts, 2.5 amps anode current and a magnetic flux density of 120 gauss. The B field was produced by running 2 amps through approximately 2000 turns of number 20 magnet wire.

### Substrate Table

The substrate table consisted of a two inch diffusion pump heating element disc enclosed in an aluminum pill box type of structure (see Fig. 2.4). A type J thermocouple was centrally mounted and in good thermal contact with the table. The heating element was used for vacuum annealing the gold thin films and was not used during ZnO deposition.

The heating table could be electrically biased with respect to the anode because, the heating element was electrically floated by connecting it to an isolation transformer and the vacuum linear feedthrough for the table was mounted in an insulating glass annulus which in turn was supported by the substrate arm vacuum plate. The linear feedthrough was necessary for varying the target substrate separation as well as permitting target changing under vacuum.

### Presputtering Shield, Target Shield

Also mounted on the substrate arm vacuum plate were the linear feedthroughs for the target and presputtering shields (see Fig. 2.4).

The presputtering shield was simply a piece of 'pie shaped' aluminum sheet while the pyrex target shield was shaped as shown in Fig. 2.2. The target shield, during sputtering was translated to a position adjacent to the unused targets. In this manner, back-scattered, sputtered material was prevented from contaminating the surfaces of the targets not in use. It also provided a guard ring necessary during the deposition of ZnO.

### Substrate Mount and Indexed Masks

Many differently shaped substrates requiring a variety of holders were used during the course of this investigation. The one shown in Fig. 2.4 was used to hold the germanium cubes on which the transducers were fabricated. The two piece holder was spring loaded and equipped with two indexing pins necessary for repeatable, accurate masking.

Also shown in Fig. 2.4 are two masks, one attached to the presputtering shaft and a second, adjacent to the holder. The former was used when the vacuum was not broken between the gold and zinc oxide deposition while the latter was used when the vacuum was broken.

As mentioned in Section 2.3.3 films triode sputtered are not uniform in thickness over extended areas. This difficulty is compounded by the substrate mask, in fact, for masked areas much smaller than the target area, their effect becomes dominant. To reduce the contribution to nonuniformity by sputtered material reflected from the mask edges, sharp edges were used.

### Chamber Shields

To facilitate rapid cleaning of the module the four horizontal arms were lined with fitted, removable glass liners. The main chamber liner was simply a pyrex cylinder with two, 1 1/2 inch diameter holes colinear with the plasma path. These apertures provided the only pumping access to the deposition region. In addition, due to their size, they served to further confine the plasma and reduce the contamination from the discharge electrodes. This liner could not be separated into two smaller liners since it supported the target shield, previously mentioned, during its translation.

### Probe

The target mounting section of the probe is illustrated in Fig. 2.6 Basically the device was a water cooled coaxial transmission line, terminated in the target material. This design made it useful for R.F. as well as D.C. sputtering.

It has a tapered termination which was found necessary for guiding the target onto the probe as well as for the formation of an

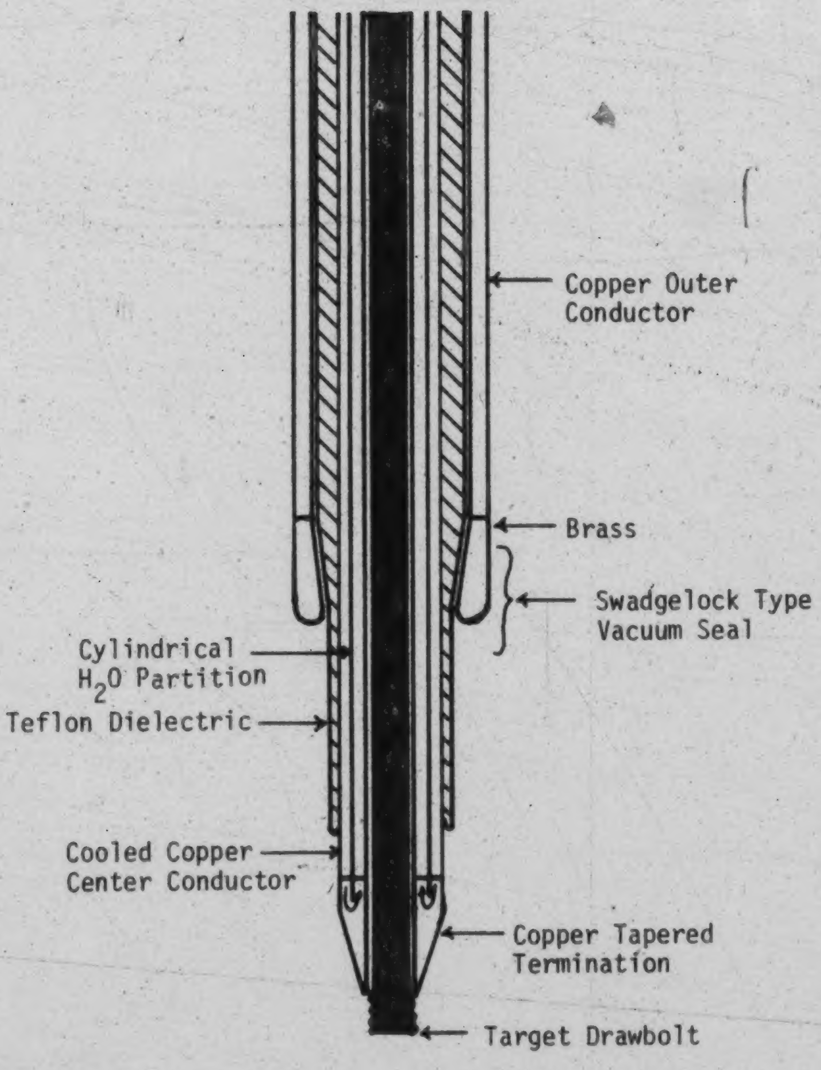
Copper Outer Conductor
Brass
Swadgelock Type Vacuum Seal
Cylindrical $H_2O$ Partition
Teflon Dielectric
Cooled Copper Center Conductor
Copper Tapered Termination
Target Drawbolt

Fig. 2.6 Cross-Section of R.F.-D.C. Probe - Target Mounting End.

acceptable thermal contact between the target and probe. The target drawbolt could be linearly moved along the probe axis. The drawbolt vacuum seal was located at the matching network end, not shown in Fig. 2.6; the vacuum seal between the inner and outer probe conductors was of a Swadgelock nature and was located approximately two inches from the target; and finally the outer conductor vacuum seal was located on the probe arm vacuum plate.

### Target Changing Assembly and Procedure

A schematic of the target mounted in the changing arm assembly is shown in Fig. 2.7.

The target itself was epoxied with 'Cerac Hot Pressing Inc., Silver Epoxy' onto a copper backing plate in the back center of which was hard soldered a tapped brass insert. Above the insert a tapered seat was machined in the copper to identically match the probe termination taper. The backing plate was spring loaded into the glass shroud using the backing plate nut. The insulating pyrex shroud guarded against sputtering from the target edge and backing plate as well as being the means by which the target was attached to the target support shroud hence the changing arm itself. For non-metals (e.g. ZnO) the shroud did not protrude past the back surface of the [illegible]get. The target shrouds were held in the target shroud supports by a spring loaded, slotted, locking arm. By simply rotating this arm 180° a new target could be inserted. Fig. 2.5 shows the relative positions of the targets during operation.

Securing the targets to the probe was accomplished by centering the targets on the probe through manipulation of the target changing arms,

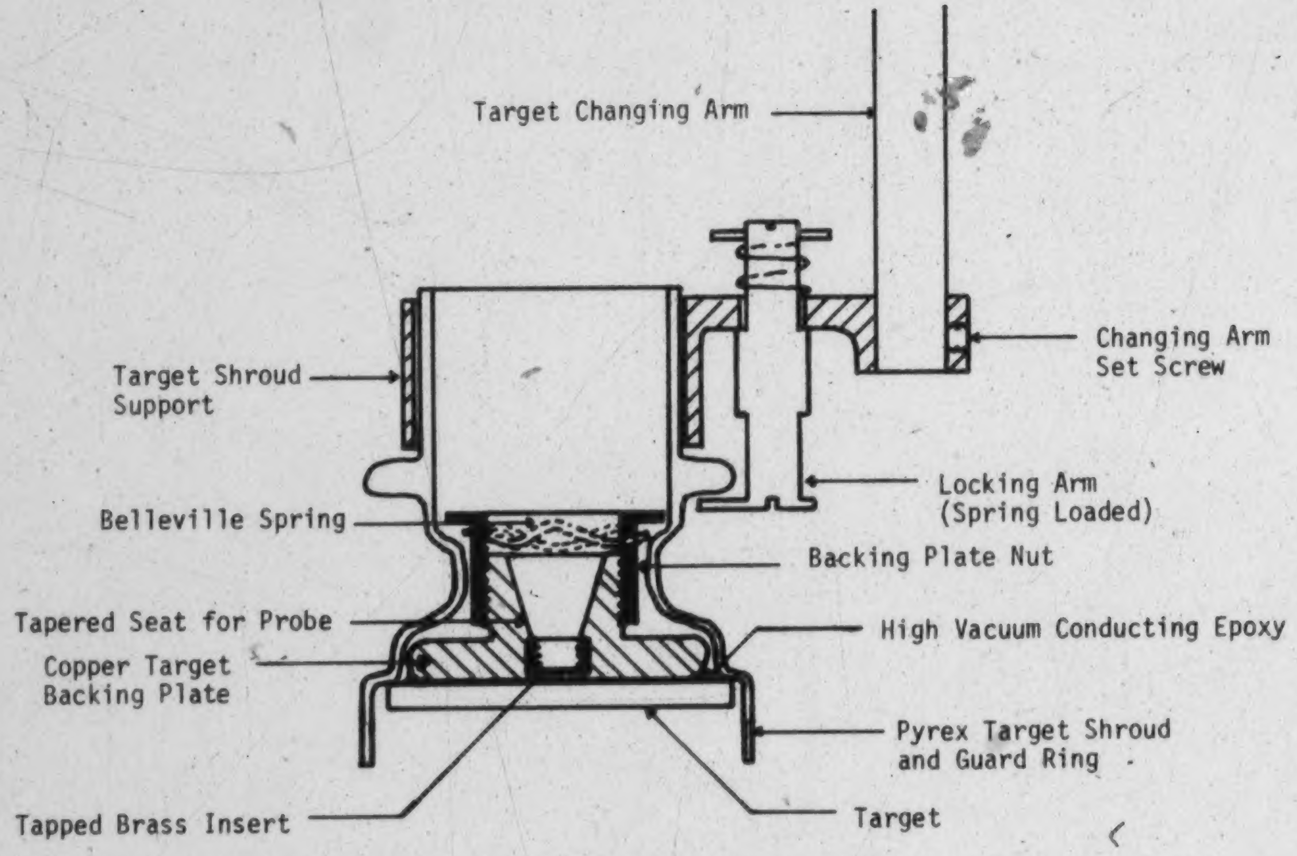

Fig. 2.7 Cross-Section of Changing Arm Assembly.

then engaging the drawbolt in the threaded insert followed by tightening of the drawbolt nut.

### 2.3.5 System Safeguards

The block diagram showing the electrical safeguards built into the system is shown in Fig. 2.8. These safeguards were necessary to allow unattended operation as well as for equipment safety.

The R.F. power supply was protected against high reflected R.F. power levels resulting from discharge failure by relay 'a', which switched the R.F. power supply off when the anode current became less than half an amp. This generally occurred as a result of filament burn out or a decrease in chamber pressure.

Relay 'b' was an over pressure relay built into the N.R.C. vacuum gauge controller and could be set to switch for chamber pressures greater than ten microns. This guarded against formation of a discharge between the probe and anode due to high pressures resulting from a sudden system leak or warming of the Meissner trap be de-energizing relay 'c'.

The power to relay 'c' was controlled by two switches, first, the normally closed contacts of relay 'b' and second, the module coolant level mercury switch. The normally open contact of relay 'c' switch the in-line module water valve; the power to the d.c. power supply, filament power supply and substrate heating power supply; as well as the timer. Therefore, when this relay is de-energized module operation is completely shut down and the time of shut down recorded.

The module coolant switch prevented the system from operating when a leak in module water lines occurred or when the main water supply was shut off.

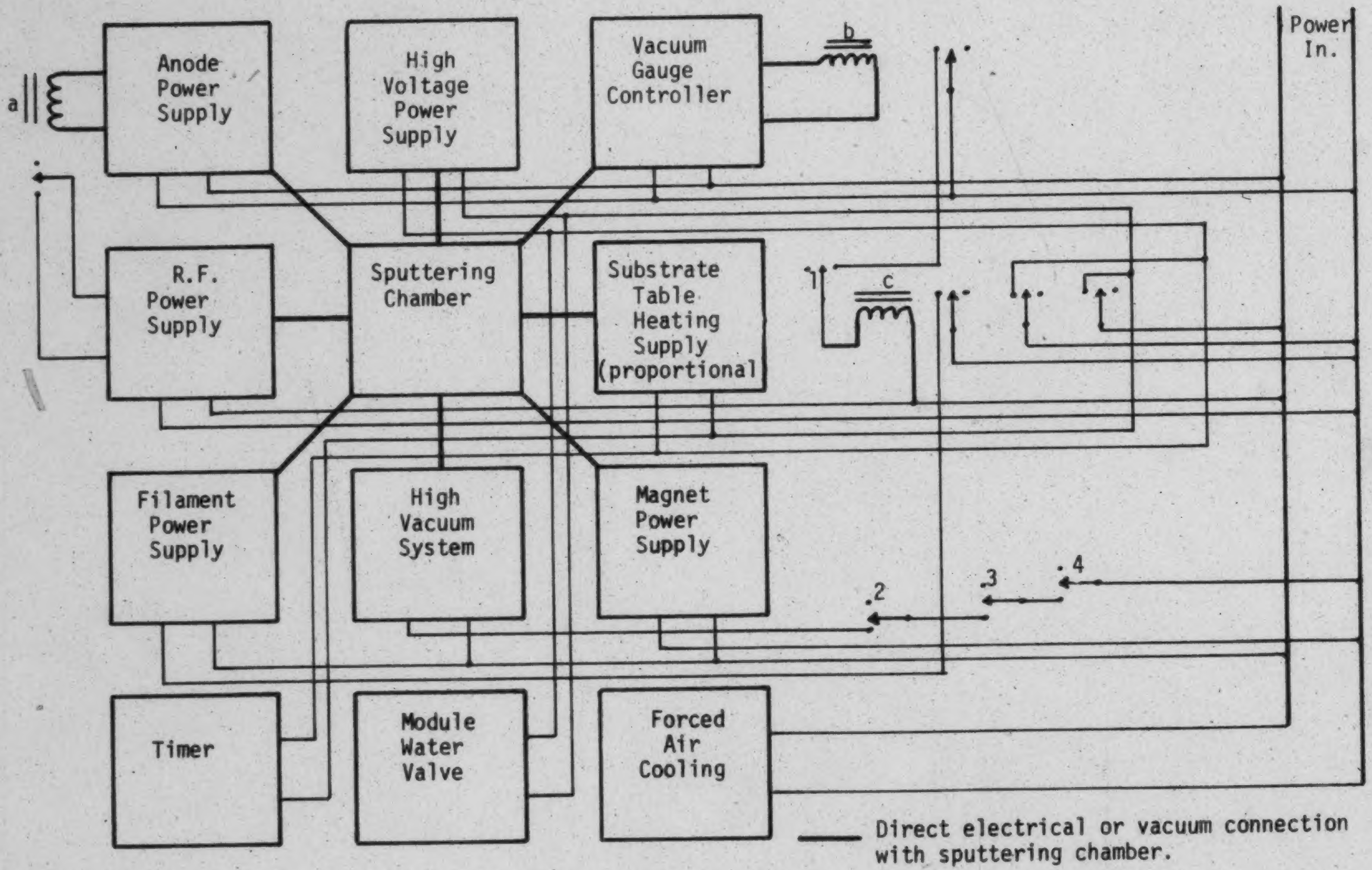

Fig. 2.8 System Block Diagram Showing Electrical Safeguards.

Legend to Figure 2.8

Relay Contacts

a - Normally open; energized by anode current

b - Normally closed; energized by over pressure gauge reading

c - Normally open ; energized by line voltage

Switches

1 - Module coolant level switch

2 - Diffusion pump thermal switch

3 - Foreline pressure switch

4 - Diffusion pump coolant switch

Under Operating Conditions

Relay Contacts

a - closed

b - closed

c - closed

Switches

1 - closed

2 - closed

3 - closed

4 - closed

The vacuum system itself was also protected by: a diffusion pump thermal switch to insure against the diffusion pump heating section rising above the cracking temperature of the diffusion pump fluid; a foreline pressure switch set for 100 Torr; and a diffusion pump coolant switch which monitors the main water pressure. Activation of any one of these switches turns off the power to the diffusion pump.

## 2.4 Discussion

One of the most common methods of providing the necessary high vacuum a system may require is to enclose the working apparatus in a bell jar type of structure which is subsequently evacuated. This approach posed many problems for a triode sputtering system in which more than one target was required. Since the probe must be adjacent to the plasma and yet opposite the substrate, only a single probe was feasible, making an externally operated target changing mechanism necessary. Also, in any deposition system, it is advantageous to position the source and substrate so as to reduce their contamination by sputtered material which has broken away from the chamber walls. This implies that the probe and substrate table feedthrough axis should be horizontal. Due to these considerations, the system employing a six arm cross was constructed. Not only was the suggested configuration realized but also, the magnet coils and water lines were kept external to the vacuum chamber. Although the system was acceptable there were problems which were encountered.

One of the major problems encountered was arcing to the sputtering targets. In the case of metals the arcing was between the target shroud and target. This is believed to be due to improper shielding which allowed the charge accumulated on the coated shrouds to discharge via an arc to that area of the target in closest proximity to the shield. This problem became more acute as the target potential and total gas pressure were increased. It is suggested that a redesigned target shroud as shown in Fig. 2.9, would alleviate the arcing problem for metal targets as well as aid in counteracting the dust problem to be discussed below. It should be noted that the use of such a target shroud was impossible in the system constructed due to the physical dimensions of the side arms.

Before considering the dust problem, arcing to the zinc oxide target should be mentioned. As indicated in Chapter III, the characteristics of sputtered zinc oxide are very dependent upon the deposition conditions used. When deposited in an oxygen deficient atmosphere the conductivity of the film and a portion of the target surface appeared to increase. Accompanying this increased conductivity was intolerable target arcing. The semicontinuous arcs in this case, were formed between the discharge and the target. The target shroud was not necessary for the formation of the arc but, due to the conducting film on it, served to aggravate the situation by offering a lower resistance discharge path to the target surface. It is thought that a conducting network to the target backing plate is formed on the target surface. This not only offers the necessary low resistance path but also effectively reduces the target area; both of which are conducive to the formation of an arc discharge. It was found that the only solution to this and other problems involving ZnO was to increase the oxygen content in the sputtering gas mix. Use of the redesigned target shroud would, however, still be desirable in order to control the 'fine particle' contamination problem.

The second major problem encountered was the control of fine

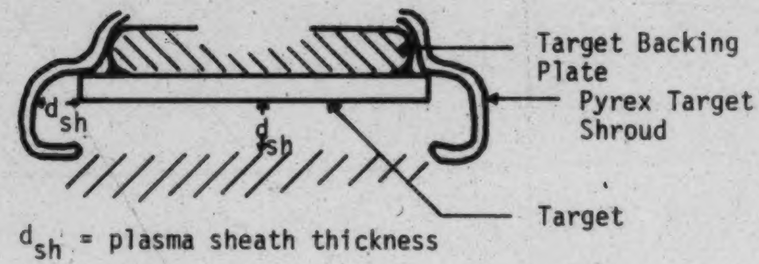

Fig. 2.9 Proposed Metal or Semiconductor Target Shroud.

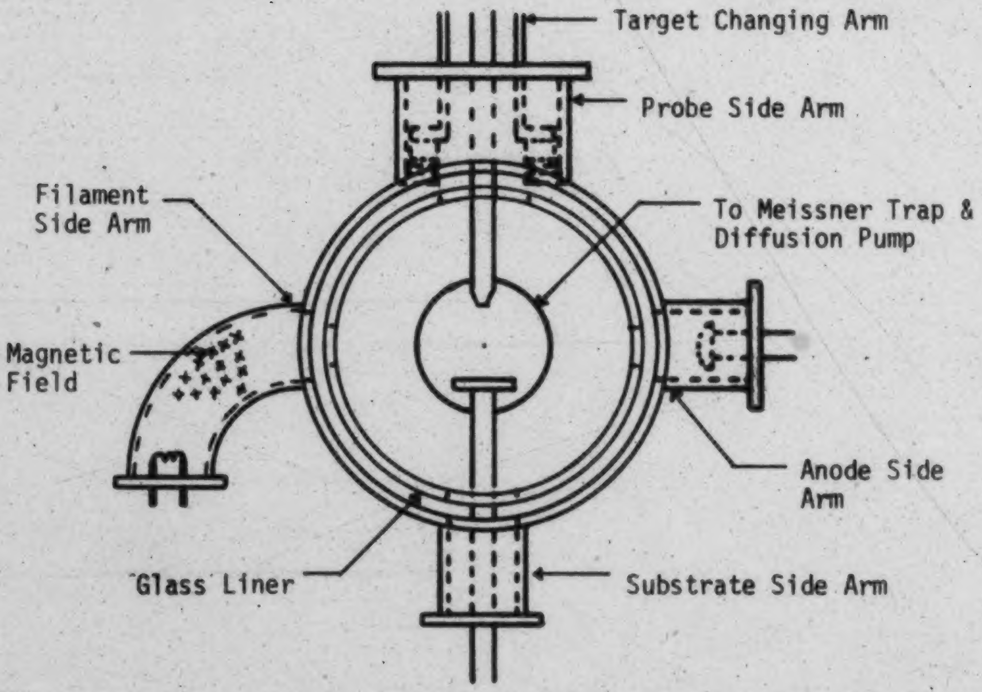

Fig. 2.10 Top View of Proposed Deposition System.

dust-like particles of ZnO which became more prevalent with increased film thickness and deposition time. This problem was extremely important since incorporation of these particles into the film during growth results in stress and pin holes which may cause the active medium to fracture or be shorted out, respectively. The source of these particles appeared to be the films on the substrate and main chamber shields as well as the target shroud, which had broken away. It is suggested that the films on these shields flake due to: (1) their intrinsic stress which will be considered in detail in Chapter III; (2) their thickness; (3) the scrubbing of the shield surfaces by the plasma, and possibly most important; (4) the angle of incidence of the sputtered material on the shields. The last two considerations are based on the observation that, the area on the chamber shield which breaks away first is at an angle of approximately 45° to the target surface normal and colinear with the plasma path through the shield. This situation, it is felt, could be improved by: (1) using the proposed cup shaped target shroud; (2) having a larger deposition chamber volume and; (3) using smooth (possibly glass) substrate masks since ZnO films, when deposited under the proper conditions on polished surfaces, are of optical quality and do not fracture. It should also be noted that the particles adhered to the target surface as well as the substrate surface. Their presence on the target surface did not seem to be affected when R.F. probe potentials were employed. A more thorough investigation would have to be performed, however, to decide whether or not their adherence was electrostatic in nature.

Another problem which existed with the system constructed was the contamination introduced into the deposition region by evaporation of the tungsten filaments. This is due to the direct line of sight access between the filament chamber and the deposition region. This direct path could be eliminated by mounting the filaments at right angles to the deposition region access apertures and bending the electron beam magnetically.

Lastly, the heating wire in the diffusion pump heating element used in the substrate table was encapsulated in porous alumina consequently subject to prolonged outgassing. This outgassing could be considerably reduced by mounting the heating wire in hard, non-porous ceramic tubes which could then be incorporated in the substrate table.

### Proposed Deposition System

The outline of a stainless steel system incorporating some of the features suggested above is shown in Fig. 2.10. Not only could the electromagnets be hung from the top plate but also mounted on this plate could be a viewing port and the vacuum gauges. The diameter of the main cylinder will depend upon the size of the target changing assembly. It is suggested, however, that it should be no less than 18 inches in diameter as well as in depth.

In addition to the interconnections presently employed, it would be advantageous to interlock the timer with a switch which monitors the filament current.

## 2.5 Conclusion

It has been shown that for large area, efficient, high frequency transducers, a thin film of ZnO is the best choice for the active medium. After considering the possible methods of deposition, a triode sputtering system was thought to be the most experimentally oriented and versatile. This versatility is highlighted by the fact that, with no modification it may be converted to a diode sputtering system. The triode system constructed was described in detail. Two significant features in this design were the R.F.-D.C. probe and the target changing facility. Although adequate, the system was not without problems and an updated system design was presented.

# CHAPTER III

# INFLUENCE OF DEPOSITION PARAMETERS ON FILM CHARACTERISTICS

## 3.1 Introduction

For thin films of ZnO to be efficient dilatational mode transducers, the 'c'-axis, (<0002> direction of the individual crystallites) must be aligned perpendicular to the substrate surface. This is referred to as perpendicular orientation. The angular distribution of the 'c'-axis of the crystallites about this preferred direction determines the 'level of perpendicular orientation'.

The structure and composition of thin films are, in general, strongly dependent upon the deposition conditions. Epitaxial ZnO thin films have previously been produced but at low supersaturations (high substrate temperatures and low deposition rates) [3.1]. In a practical fabrication system however, one is limited to deposition at high supersaturations. Although this generally results in films having a low level of orientation, it was found that by controlling the state of the nucleating surface (thin film of gold) as well as the partial pressure of oxygen in the sputtering gas mix, a high level of orientation could still be obtained.

In particular, it was observed that the degree of <111> perpendicular orientation in the gold film was reflected in the level of <0002> perpendicular orientation in the overlaying ZnO thin film. However, concomitant with this increased level of orientation was an increase in the level of mechanical stress. This problem was eventually traced to an oxygen deficiency in the sputtering gas mix.

The following two sections deal with the x-ray technique used to evaluate the crystal structure of the films and; the method employed to measure the film thickness hence deposition rate. In Section 3.4 the factors influencing the level of orientation in ZnO thin films are discussed. The manner in which the stress manifests itself is presented in Section 3.5 and in Section 3.6 the results of the non-structural analysis are given. The chapter is followed by a discussion and conclusion.

## 3.2 X-Ray Analysis

A modified Debye-Scherrer powder x-ray diffraction technique was the primary diagnostic tool used to investigate the crystalline structure of the thin films.

X-ray diffraction is based upon Bragg's law, namely

$$2d_{hkl} \sin \Theta_B = n\lambda_x \tag{3.1}$$

where $d_{hkl}$ = the interplanar spacing between planes having the Miller indices h,k,l,

$\Theta_B$ = the Bragg angle between the incident beam and the diffracting plane in the crystal

and $\lambda_x$ = the x-ray wavelength.

This equation may be expressed diagrammatically in terms of the reciprocal-lattice vectors. This construction, due to Ewald, is shown in Fig. 3.1

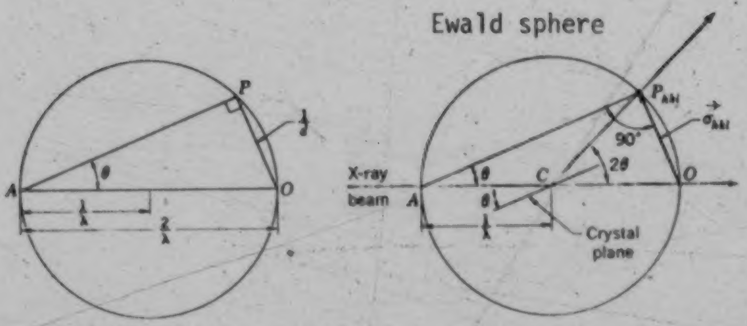

Fig. 3.1 Graphical Interpretation of the Bragg Law in Terms of Reciprocal Lattice Vectors

where $\vec{\sigma}_{hkl} = \dfrac{1}{d_{hkl}}\vec{n}$ = reciprocal-lattice vector (3.2)

and $\vec{n}$ = the unit vector normal to the diffracting plane of the crystal.

From this construction it can be seen that a diffracted beam is possible only when a reciprocal-lattice vector lies on the Ewald sphere of reflection. The reciprocal lattice is derived from the real lattice using equation (3.2).

Thin films are polycrystalline so that many crystals will be irradiated by the incident x-ray beam and also, these crystals will be in general, randomly oriented with respect to each other. Therefore, the reciprocal-lattice vectors representing any one particular plane will be randomly directed but all of the same length. The reciprocal-lattice space may therefore be represented as a collection of concentric spheres whose radii are the various possible reciprocal-lattice vectors. Since the intersections of two spheres (Ewald sphere of reflection and the reciprocal lattice sphere) is a circle, for each reciprocal lattice vector a cone of diffracted x-rays passing through this circle emanates from the specimen. Analysis of the diffracted radiation as captured on film provides information on the interplanar spacings in the material as well as any preferred orientation, denoted as texture, which may be present in the specimen.

Texture occurs when a particular plane or planes (represented by their normals) in the individual crystallites tend to be aligned about a preferred direction. For thin films, this situation is very often encountered and is highly dependent upon the thin film deposition conditions. Due to this preferential alignment, the angular distribution of the crystal planes is no longer completely random. That is, the reciprocal-lattice vectors no longer lie on a closed spherical surface but on an open portion thereof, which is centered about the preferred direction. The diagrammatical representation for this situation is shown in Fig. 3.2 for the case of ZnO.

Essentially the x-ray photograph is a projection of the spherical section of the intersection between the Ewald sphere of reflection and the reciprocal-lattice spheres. When this intersection is as shown we have perpendicular orientation. This is because the reciprocal-lattice vectors for the ZnO (0002) plane are distributed about the normal to the plane of the thin film. Should they be distributed parallel to the plane of the film, the orientation will be termed parallel and no reflection from the ZnO (0002) plane will be observed. The perpendicular orientation, necessary for thickness mode dilatational transducers, is of course, desired.

The surface of the specimen has been tilted 15° with respect to the incident x-ray beam so the reflection from the (0002) plane would be

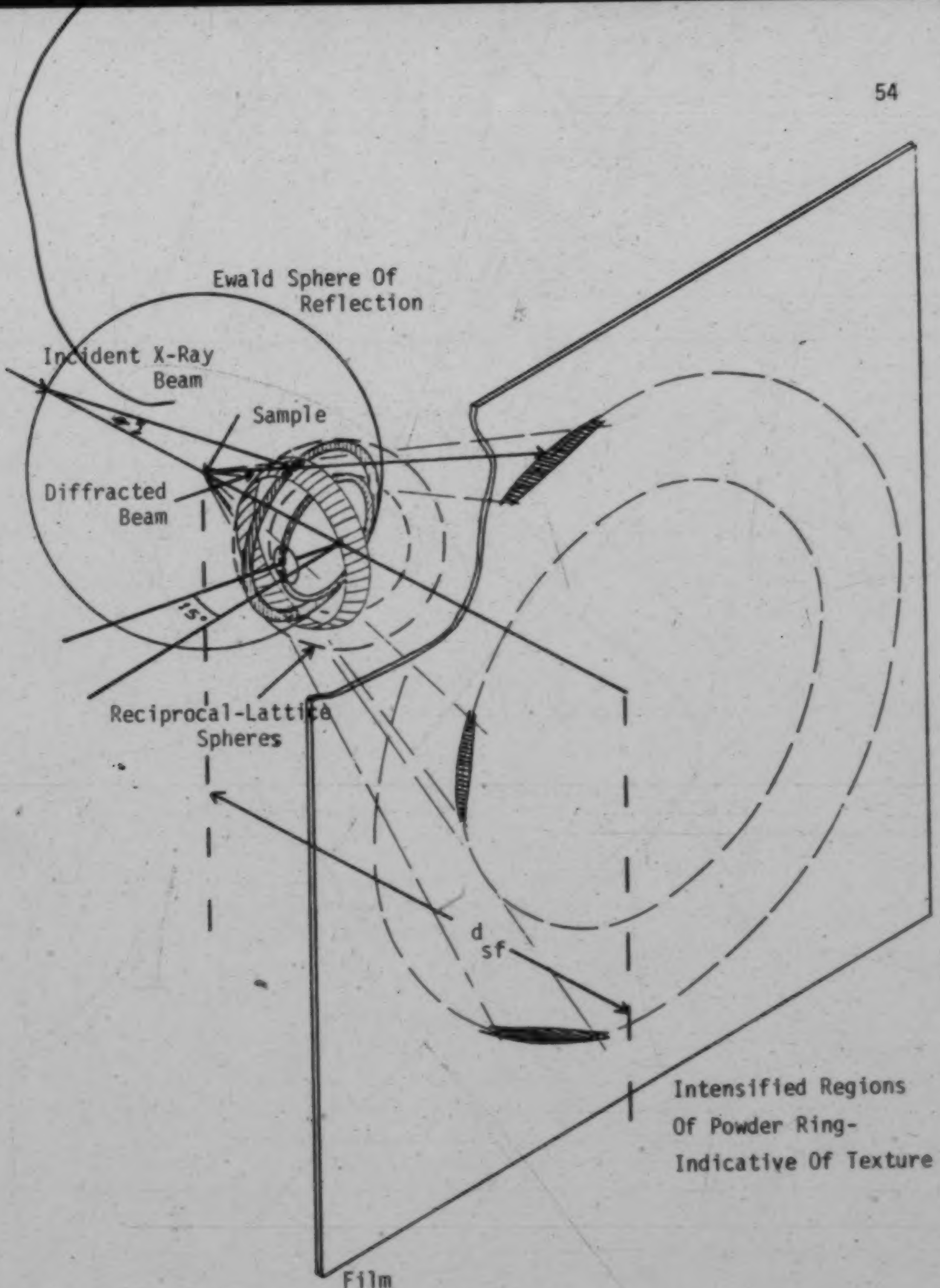
Ewald Sphere Of Reflection
Incident X-Ray Beam
Sample
Diffracted Beam
15°
Reciprocal-Lattice Spheres
$d_{sf}$
Intensified Regions Of Powder Ring- Indicative Of Texture
Film

Fig. 3.2 Graphical Explanation of X-Ray Distribution from Textured Specimen - Modified Debye-Scherrer Powder X-Ray Diffraction Technique.

recorded. The x-ray wavelength used was 1.54 Å obtained from nickel filtered radiation from a copper x-ray target. The specimen to film distance , $d_{sf}$, was usually 5 cm. The approach for films other than ZnO was similar.

### 3.3 Thickness Determination

Thickness is, in general, the single most significant film parameter [3.2]. It may be measured either by in-situ monitoring of the deposition rate or after the film is removed from the deposition chamber. The latter method was employed due to the deposition parameter control inherent in the triode sputtering process. The various materials were deposited under controlled deposition conditions, then the films were removed from the chamber and their thickness determined by the stylus method. A Taylor-Hobson Tallysurf 4 having a vertical resolution of ∿ 125 Å and a horizontal resolution of $10^{-2}$ inches, was used.

The stylus in this case, consisted of a diamond with a rounded ($R = 1.25\mu$) tip fastened to a lever arm which was delicately balanced so that the load on the tip was only .1 gram. A differential inductance transducer transforms vertical variations of the stylus arm, as it is dragged across a surface, into an electrical signal which is subsequently amplified by $10^5$ to $10^6$ and fed into a recorder. An example of the recorder output for a chromium thin film sputtered on a pyrex substrate is shown in Fig. 3.3.

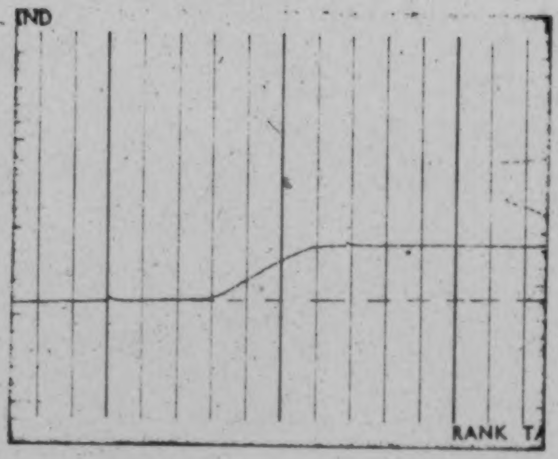

Fig. 3.3 Tallysurf 4 Recorder Output Trace of Edge of Chromium Thin Film Sputtered on Glass Disc, Vertical div. = 508 Å; Horizontal div. = $10^{-2}$ in.

The advantages of this method are: (1) it is applicable to all films, that is, metallic, semi-conducting or dielectric; (2) the maximum thickness which may be recorded is essentially unlimited; (3) the film need not be deposited on a special substrate (provided it is reasonably flat and parallel) or undergo any post deposition treatment thereby permitting it to be used as originally intended (e.g. as a transducer); (4) it provides not only the height of the step but also the step profile and lastly; (5) absolute measurements can be made rapidly.

When doing a deposition rate calibration run, the percent error due to the relatively low resolution (compared to interferometric methods) can be considerably reduced by increasing the thickness of the film. In this manner the percent error was reduced to less than 1%. For the transducer equivalent circuit analysis to be presented in Chapter IV, the film thickness accuracy required is ~ 5%. This was the approximate repeatability of the deposition process as measured for 7μ thick ZnO thin films. Therefore, the accuracy of the Tallysurf 4 was more than suitable for this investigation. There was, however, one problem with this particular model of Tallysurf; the force on the stylus was enough to create a visible (under a microscope) trench in the soft gold films. In this case the gold thin films had to be overcoated with a chromium film before being measured. In models of the Tallysurf specifically designed for thin film thickness analysis, this problem is largely overcome [3.2].

## 3.4 Factors Affecting the Level of Orientation in ZnO

The effect on the thin film crystal structure of various deposition parameters were determined by the x-ray procedure discussed in Section 3.2. The values of oxygen partial pressures quoted in this section should not be taken as absolute for reasons already discussed. In general, results involving the use of high vacuum systems are very difficult to duplicate exactly in different (environmentally as well as physically) systems. Values specified should, therefore, be thought of as indicative of trends rather than absolute.

### 3.4.1 Sputtering Potential

In Fig. 3.4 the effect of the sputtering potential on the orientation is demonstrated. In Fig. 3.4a and b the probe conditions were 800 volts and 1500 volts, respectively, at 34 milliamps, using a 10K ballast resistor. The potential specified, in all cases, includes the

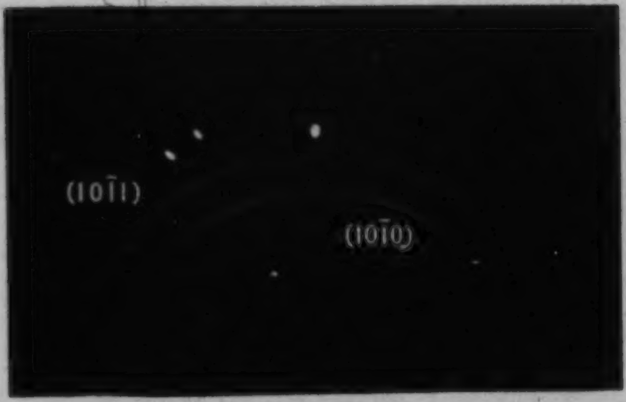

Fig. 3.4a - 800v, 34ma, 10k; 25 Å/min.

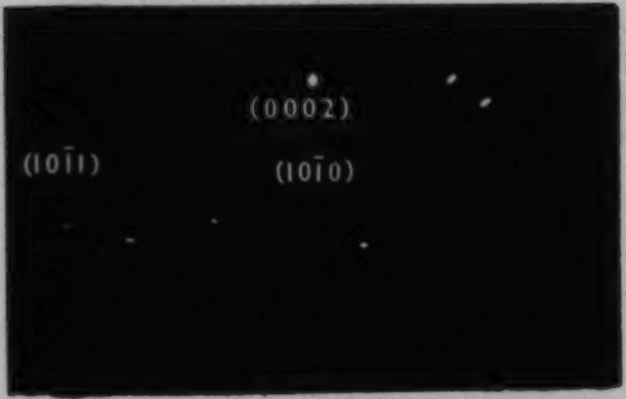

Fig. 3.4b - 1500v, 34ma, 10k; 50 Å/min.

Fig. 3.4 X-Ray Diffraction Photographs of ZnO Triode Sputtered on Single Crystal Germanium.

Fig. 3.5 X-Ray Diffraction Photograph of ZnO Triode Sputtered on Single Crystal Germanium - 200 Å/min.

voltage drop across the ballast resistors. The common ZnO deposition conditions were:

Substrate - unoriented single crystal germanium
$P_{O_2}$ - 15%
$P_T$ (total measured pressure) - ~ 1.5μ
Deposition Rate - < 50Å/min
Substrate Table Temperature - 75°C to 125°C.

The film in Fig. 3.4a exhibits no perpendicular orientation whereas that in Fig. 3.4b does show a low level of <0002> perpendicular orientation. Both films were mechanically stable.

These results suggest that the level of <0002> perpendicular orientation improves with increased target potential. Since the highest possible level of <0002> perpendicular orientation in a mechanically stable film is required, a high accelerating potential was used.

### 3.4.2 Deposition Rate

In Fig. 3.5 the effect of increasing the deposition rate on the orientation is shown. Here a deposition rate of approximately 200Å per minute was used. This is to be compared with that used for the film in Fig. 3.4b. The remaining ZnO deposition parameters were:

Substrate - unoriented single crystal germanium
$P_{O_2}$ - 45%
$P_T$ - 6μ

Substrate Table Temperature - 75°C to 125°C
Target - 1.6Kv, 43 ma, 10K.

The x-ray photograph again indicates a lack of perpendicular orientation. The film was mechanically stable.

As is generally accepted, increasing the deposition rate (raising the supersaturation) has a randomizing effect on the crystalline order in a thin film. This effect is observed to be substantial since a high target potential was employed as well as a high partial pressure of oxygen, both of which are conducive to creating a higher level of perpendicular orientation. The significance of the latter condition will become apparent in the following section.

From a practical fabrication point of view, a deposition rate as high as possible is advantageous.

### 3.4.3 Partial Pressure of Oxygen in Sputtering Gas Mix - $P_{O_2}$

The partial pressure of oxygen used in the sputtering gas mix was very important in this investigation since it not only affects the film structure but also the level of stress in the ZnO films. These two film characteristics are, of course, expected to be interrelated.

In Fig. 3.6a, b and c, the partial pressures of oxygen in the sputtering gas mix were 0%, 30% and 60%, respectively. The common ZnO deposition conditions were:

Substrate - pyrex discs
$P_T$ - 6μ

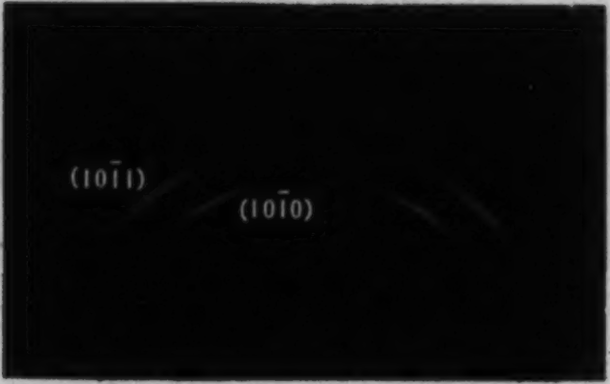

Fig. 3.6a - $P_{O_2}$ = 0%

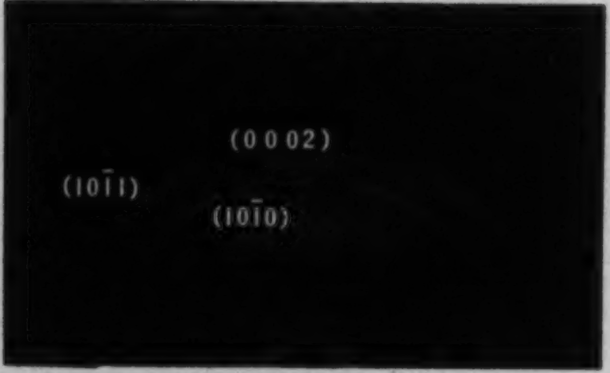

Fig. 3.6b - $P_{O_2}$ = 30%

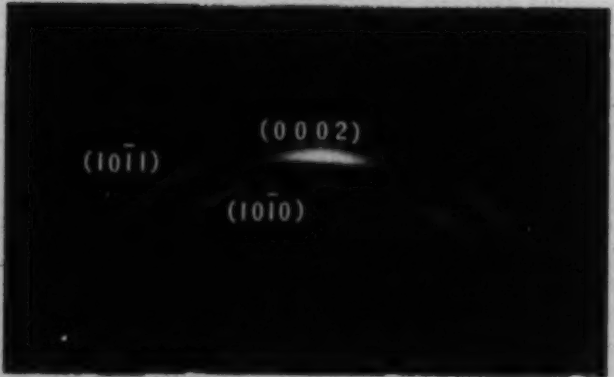

Fig. 3.6c - $P_{O_2}$ = 60%

Fig. 3.6 X-Ray Diffraction Photographs of ZnO Triode Sputtered on Pyrex - 1.65kv, 44ma, 10k; 300 Å/min.

Deposition Rate - 300Å/min

Substrate Table Temperature - 75°C to 150°C

Target - 1.65 kv, 44ma, 10K.

It can be seen that an increased $P_{O_2}$ induces a higher level of perpendicular orientation for ZnO on amorphous pyrex. It must be noted here that the film responsible for Fig. 3.6b failed mechanically but the films in Fig. 3.6a and c had sub-failure stress levels. Thus, not only does increasing $P_{O_2}$ improve the film orientation but it also serves to relieve stress. In the case represented in Fig. 3.6b, the induced level of orientation was higher than a $P_{O_2}$ = 30% could stress relieve.

This $P_{O_2}$ stress relief effect may be stated as follows: depending upon the orientation induced, the mechanical stress can be reduced to a sub-failure level by appropriately adjusting $P_{O_2}$. This will be made more obvious in the section dealing with the effect of the nucleating surface on the orientation in a thin film.

Scanning electron microscope (S.E.M) photographs of the films from which Fig. 3.6a and c were derived are shown in Fig. 3.7a and b. The angle between the substrate surface normal and the incident electron beam was 18° for these photographs. The surface in Fig. 3.7a ($P_{O_2}$ = 0%) appears to be composed of small crystallites randomly oriented while that in Fig. 3.7b ($P_{O_2}$ = 60%) appears to be made up of better oriented, larger crystallites. Due to the specimen shape, focusing with magnifications greater than 20,000 was difficult. Sharply focused photographs at higher magnification of the surface itself or a replica thereof would be necessary for a precise grain size determination. Here we see that the oxygen content affects not only the orientation in ZnO thin films on pyrex but also the grain size.

Fig. 3.7a S.E.M. Photograph of the Thin Film Represented in Fig. 3.6a.

Fig. 3.7b S.E.M. Photograph of the Thin Film Represented in Fig. 3.6c.

Fig. 3.8 Photograph of a Large Fractured Area in a ZnO Thin Film. (500x)

Fig. 3.9 Photograph of a Fractured Area in which the Expelled Material has been Re-Incorporated into the Film. (50x)

### 3.4.4 Nucleating Surface

Before considering the effect a gold nucleating surface has on ZnO thin films it should be observed from the previous figures that neither single crystal germanium (orientation relative to the film unknown) nor pyrex surfaces had a dominating effect on the orientation observed in the overlaying films. ZnO was also deposited on evaporated and sputtered thin film chromium surfaces with similar results. In all of these cases, the system deposition parameters had a greater effect on the level of orientation than the substrate surfaces. In any case, depending upon the deposition conditions, the best <0002> orientation achieved on poor nucleating surfaces could only be described as low level.

The diffraction patterns obtained for three Cr-Au-ZnO combinations are given in Fig. 3.10. In all instances, the ZnO target conditions were 1600 volts at 44 milliamps using a 10K ballast resistor, and the substrate table temperature rose from 75°C to 150°C during deposition. The remaining deposition parameters were:

Fig. 3.10a Cr evaporated at 400 Å/min
Au evaporated at 6000 Å/min
ZnO sputtered at 300 Å/min
$P_{O_2}$ = 20%

Fig. 3.10b Cr evaporated at 400 Å/min
Au evaporated at 300 Å/min
ZnO sputtered at 300 Å/min
$P_{O_2}$ = 45%

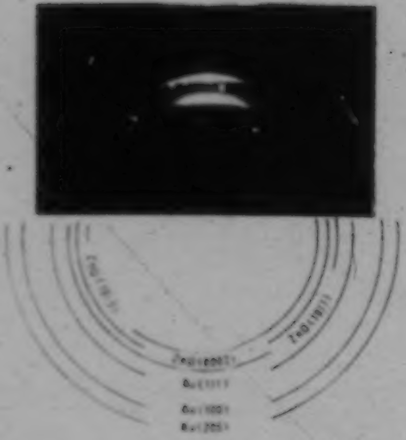

Fig. 3.10a Gold-Flash Evaporated, Not Annealed

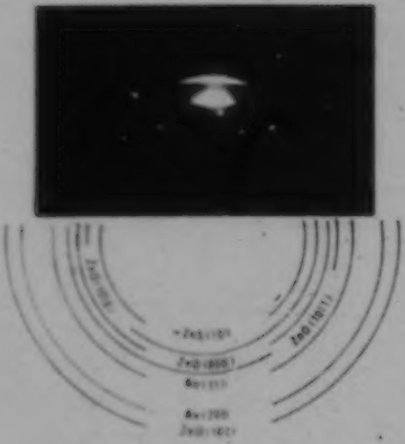

Fig. 3.10b Gold-Slowly Evaporated, Vacuum Annealed

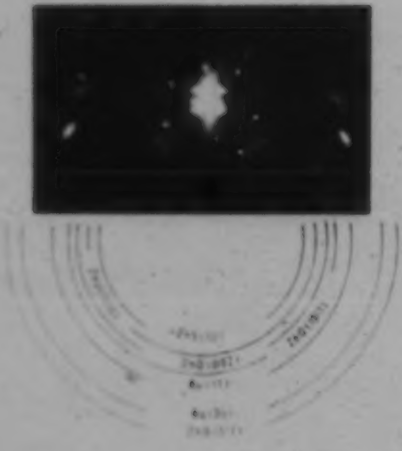

Fig. 3.10c Gold-Triode Sputtered, Vacuum Annealed

Fig. 3.10 X-Ray Diffraction Photographs of ZnO Triode Sputtered on Gold Thin Film Surfaces.

Fig. 3.10c Cr sputtered at 125 Å/min

Au sputtered at 250 Å/min

ZnO sputtered at 300 Å/min

$P_{O_2}$ = 60%

Fig. 3.10a shows the orientation of a ZnO film deposited onto a rapidly evaporated, unannealled thin film gold surface. This corresponds to the usually reported case in which a 80% - 20% (or less), Ar-$O_2$ mix is sufficient for mechanical stability [3.3, 3.4, 3.5, 3.6]. In Fig. 3.10b the gold was evaporated at a much slower rate and annealled. Corresponding to this case a 55% - 45%, Ar-$O_2$ mix was found necessary to prevent mechanical failure. In the "All" sputtered combination, shown in Fig. 3.10c, a 40% - 60%, Ar-$O_2$ mix was necessary. Note that the sputtered nucleating gold film exhibited the highest <111> perpendicular orientation, whereas the flash evaporated gold showed the least. Directly correlating with this orientation of the gold surface is the <0002> perpendicular orientation of the subsequent ZnO film. It is clearly evident that the orientation of the gold nucleating surface has a stronger influence on the subsequently deposited ZnO thin films than do the system deposition parameters themselves.

These results may be summarized as follows: as the level of orientation induced by the nucleating surface becomes higher, the mechanical stress increases proportionately in an oxygen deficient atmosphere. As previously stated, this mechanical stress, however, could be reduced to a sub-failure level by appropriately adjusting $P_{O_2}$.

Note that just as the crystalline structure of ZnO is affected by the deposition conditions so is that of gold thin films. In particular, the structure in gold thin films depends, as do all evaporated or sputtered films, on the supersaturation during deposition. Sputtering, effectively a means of producing a low supersaturation, therefore produced the higher level of <111> perpendicular orientation in the gold thin films.

## 3.5 Stress Manifestation

By visually observing ZnO thin films during stress failure it was found that the failure generally started at the mask edge and proceeded radially inward, taking about one minute to completely cover the surface. The larger surfaces generally failed first.

In an attempt to reduce the stress discontinuity at the mask edges, the masks were countersunk on the substrate side. Due to randomizing intermolecular collissions, resputtering and subsequent lateral spread of deposited material, a gradual increase in thickness resulted in the area under the countersink. This appeared to reduce the stress discontinuity since films, deposited with insufficient $P_{O_2}$ took much longer to fail. In these cases failure occurred at thicknesses of less than one micron.

Although an accurate measurement of these stresses were not obtained it can be stated that the bulk substrate surfaces, namely pyrex and germanium were visibly damaged only under the unmasked areas on which the ZnO films were deposited. This effect was, of course, only observed when the inter-film adherence and the film-substrate adherence were stronger than the interatomic forces in the bulk substrate. Such a situation existed for the gold nucleating thin films only when a chromium thin film was deposited, without breaking the vacuum, between the gold film and the bulk substrate. It is primarily for this reason that the target changer was built into the deposition system.

Microscope photographs of the fractured thin films revealed that the mode of failure was one in which areas from ten to one hundred microns in linear dimension would literally pop out of the thin film. Even in mechanically satisfactory films, a small number of widely separated areas in which the stress was above the failure level would occur. One such fractured area is shown in Fig. 3.8.

Aside from the intrinsic stress in the thin film, stress due to incorporation of debris from either an area already fractured or the deposition chamber, will contribute to these failures. Examples of such incorporation are shown in Fig. 3.9 and Fig. 3.11, respectively. The fact that these incorporations result in localized stress areas may be seen in Fig. 3.11b. The object in this figure was exactly the same as that in Fig. 3.11a, but polarized light was used to illuminate the specimen and the reflected light from the specimen was passed through a perpendicularly polarized analyser. As shown, the area around the inclusion has become optically active. This appears to be due to stress and not due to the 'c'-axis of ZnO being tilted, although this may be true in this region. The following explanation is suggested. In the dark regions of the photograph, the thin films with the 'c'-axis perpendicular to the substrate, do not exhibit optical activity. Therefore, ZnO thin films are not normally optically active and will not become active due simply to 'c'-axis rotation. A concise statement of this phenomenon is given by Nye, "the essential fact about optical activity in isotropic

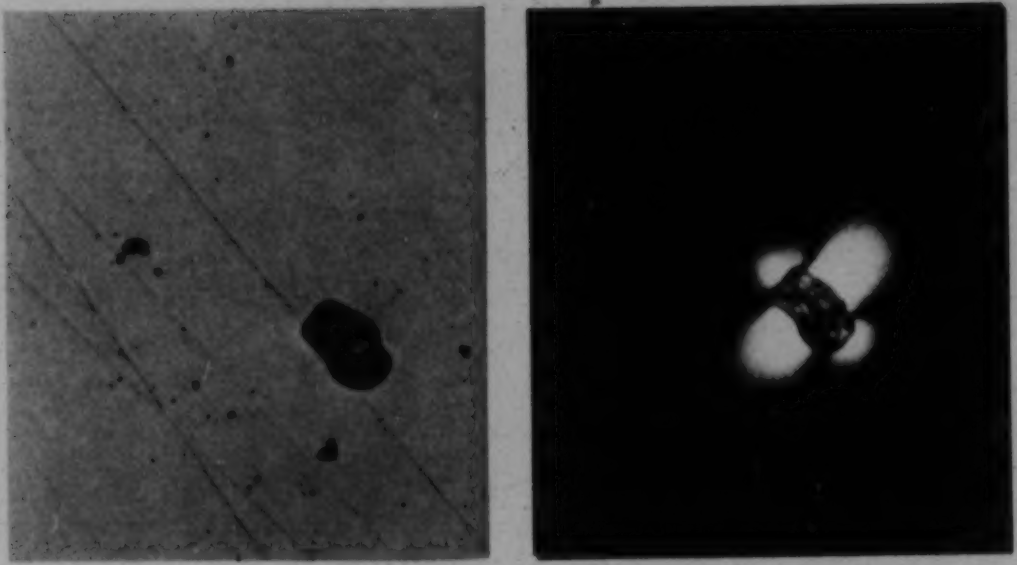

Fig. 3.11a Analyser not Crossed Fig. 3.11b Analyser Crossed

Fig. 3.11 Photographof ZnO Film Surface in which Chamber Debris has been Incorporated into the Film. (500x)

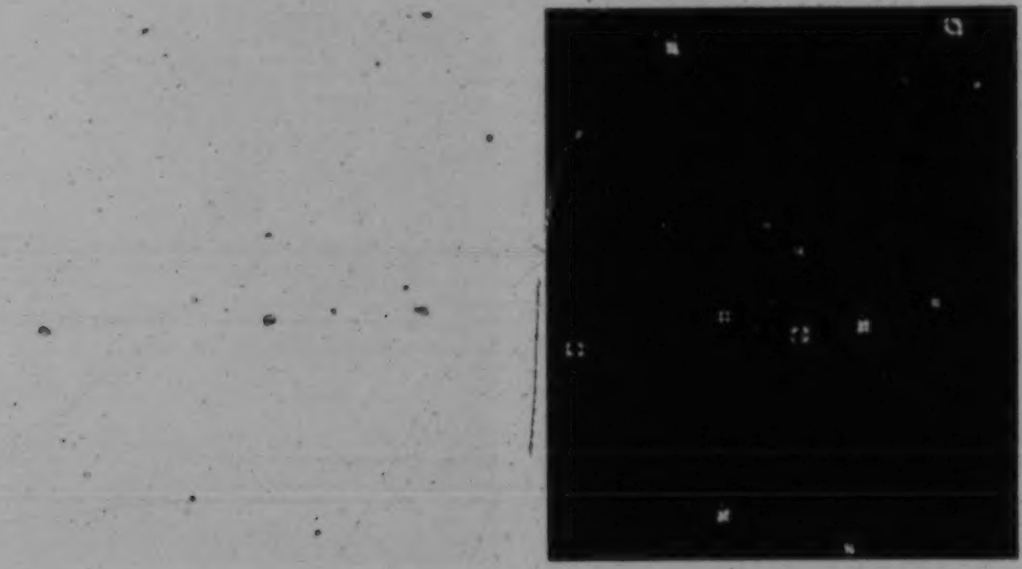

Fig. 3.12a Analyser not Crossed Fig. 3.12b Analyser Crossed

Fig. 3.12 Photograph of ZnO Film Surface Showing Typical Size and Density of Inclusions. (50x)

media, in cubic crystals, and for transmission along the optic axes of uniaxial and biaxial crystals, is this: the nature of the medium is such that two circularly polarized waves of opposite hand and different velocity may be transmitted through it unchanged in form, that is, in their state of polarization, while a plane polarized wave may not be so transmitted" [3.7].

The magnification used for photographs in Fig. 3.11 was approximately 500. The central inclusion in this photograph was above average in size. More typical of the size and density are the inclusions evident in Fig. 3.12 in which a magnification of approximately 50 was used. Again, the objects in both photographs are identical and polarized light was employed.

## 3.6 Non-Structural Analysis

In an effort to gain some insight into the chemical composition of the ZnO thin films several experiments were performed.

### 3.6.1 Electron Probe

A beam of high energy electrons is used to excite the characteristic x-ray spectra of elements present in the sample. To a first approximation, the intensity of any given x-ray line of a particular element is proportional to the weight concentration of the element in the sample. Thus

$$C_{sp} = \frac{I_{sp}}{I_{st}} \times C_{st} \tag{3.3}$$

where $C_{sp}$ = weight concentration of an element in the specimen,

$C_{st}$ = the known weight concentration of the same element in the standard,

$I_{sp}$ = measured intensity of an x-ray line of the element in the specimen,

and $I_{st}$ = measured intensity of the same x-ray line of the element in the standard.

The samples which were investigated by x-ray diffraction (Fig. 3.6a and c) were also probed for their zinc content. Before considering the probe results the visible characteristics of the target surface and the films under the respective $P_{O_2}$ deposition conditions must be stated. When $P_{O_2}$ = 0%, the zinc oxide target surface became very slightly gray and the film was transparent and pale yellow in color. The film deposited with $P_{O_2}$ = 60% was not as transparent and a definite brownish yellow in color while the target surface was white. These observations are symptomatic of stoichiometric variations and, therefore, one would have expected a difference in the composition of the films.

The samples were analyzed by the microprobe for the weight concentration of zinc in the films. In both cases, there were two standards of known chemical composition used; namely, pure metallic zinc and sphalerite, ZnS. The results were repeatable and thought to be accurate to within 1%. In both films, the zinc content was the same, 77% weight concentration which is 3% less than the theoretical value of 80%. Probe analysis was not carried out to determine what percentage of the remaining 23% was due to comtaminants, however resistivity, visible and infrared spectrophotometer investigations on different samples were carried out to further characterize the films.

### 3.6.2 Resistivity

The resistivity of a ZnO thin film deposited on glass with $P_{O_2}$ = 50% was determined from the standard equation,

$$r = \frac{R x A}{\ell} \tag{3.4}$$

where r = resistivity,
A = cross-sectional area,
ℓ = electrode separation
and R = measured resistance.

The film was one micron thick, .5 cm wide and 2 cm long with gold electrodes evaporated on both ends. A resistivity $> 10^6$ Ω-cm was obtained. Unfortunately a resistivity measurement of a film deposited with $P_{O_2}$ = 0% was not determined, however, it is expected that the resistivity would be considerably less. This is based on the target discoloration and severe arcing observed when depositing ZnO thin films in a pure argon atmosphere.

Resistivity of ZnO thin films has been considered by Raimondi and Kay [3.8]. They state, "Zinc Oxide (ZnO) is a meterial which, under ordinary circumstances, has a small oxygen deficiency. This lack of chemical stoichiometry makes ZnO an n-type semiconductor with a typical resistivity of 1-100 Ω-cm". They also state that by sputtering in an oxygen rich environment resistivities as high as $10^8$ Ω-cm may be obtained. Our results are consistent with these statements.

### 3.6.3 Band Gap

Presented in Fig. 3.13 are the visible spectrophotometer scans performed on ZnO films deposited on glass with $P_{O_2} = 45\%$ and 60%. The cut-off at 3900 Å corresponds to a band gap energy of 3.185 ev, consistent with the accepted bulk value of 3.2 ev [3.9]. The very slight absorption edge variation with $P_{O_2}$ was repeatable.

### 3.6.4 Optical Properties in the Infrared

The index of refraction and the effect of ZnO lattice absorption bands in the 2.5 to 40 micron infrared range were also considered. I.R. spectrophotometer scans for (a) an uncoated germanium disc and (b) the disc coated on both surfaces with equal thickness ZnO thin films ($P_{O_2} = 50\%$) are presented in Fig. 3.14. Also included in this figure are the I.R. absorption data for (c) single crystal ZnO and $WO_3$ (d) [3.10, 3.11, 3.12]. From thickness measurements of the film and the location of the $\lambda/2$ and $\lambda/4$ transmission extrema the index of refraction was found to be 2.09 ± 0.1. Examination of curve (b) indicates that the films are definitely absorbing around 2.9 microns (3400 $cm^{-1}$). This absorption may be due to scattering or slight contamination from the tungsten filaments. The latter conjecture appears to be supported by curve (d). Abrupt changes in the film transmittance are observed at 11.5 microns (850 $cm^{-1}$) and 15 microns (650 $cm^{-1}$). From curve (c) these changes may be attributed to the strong second order (two photon) lattice absorption peak in bulk ZnO at 11.4 microns and the main (Reststrahlen) lattice absorption (generation of a transverse optical phonon) band centered at 24.2 microns [3.11, 3.13].

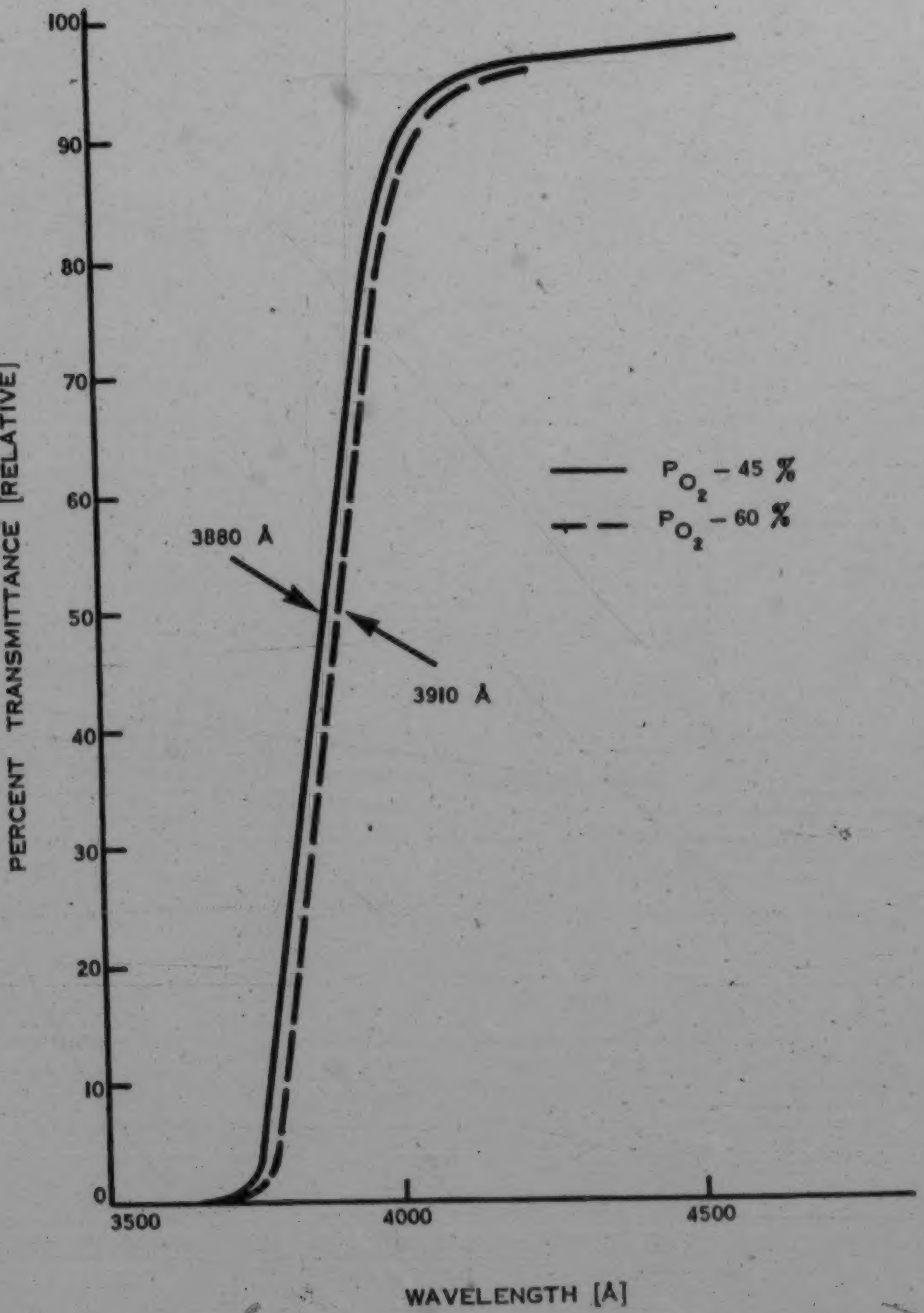

Fig. 3.13 Visible Spectrophotometer Scan of ZnO Film Deposited on Pyrex.

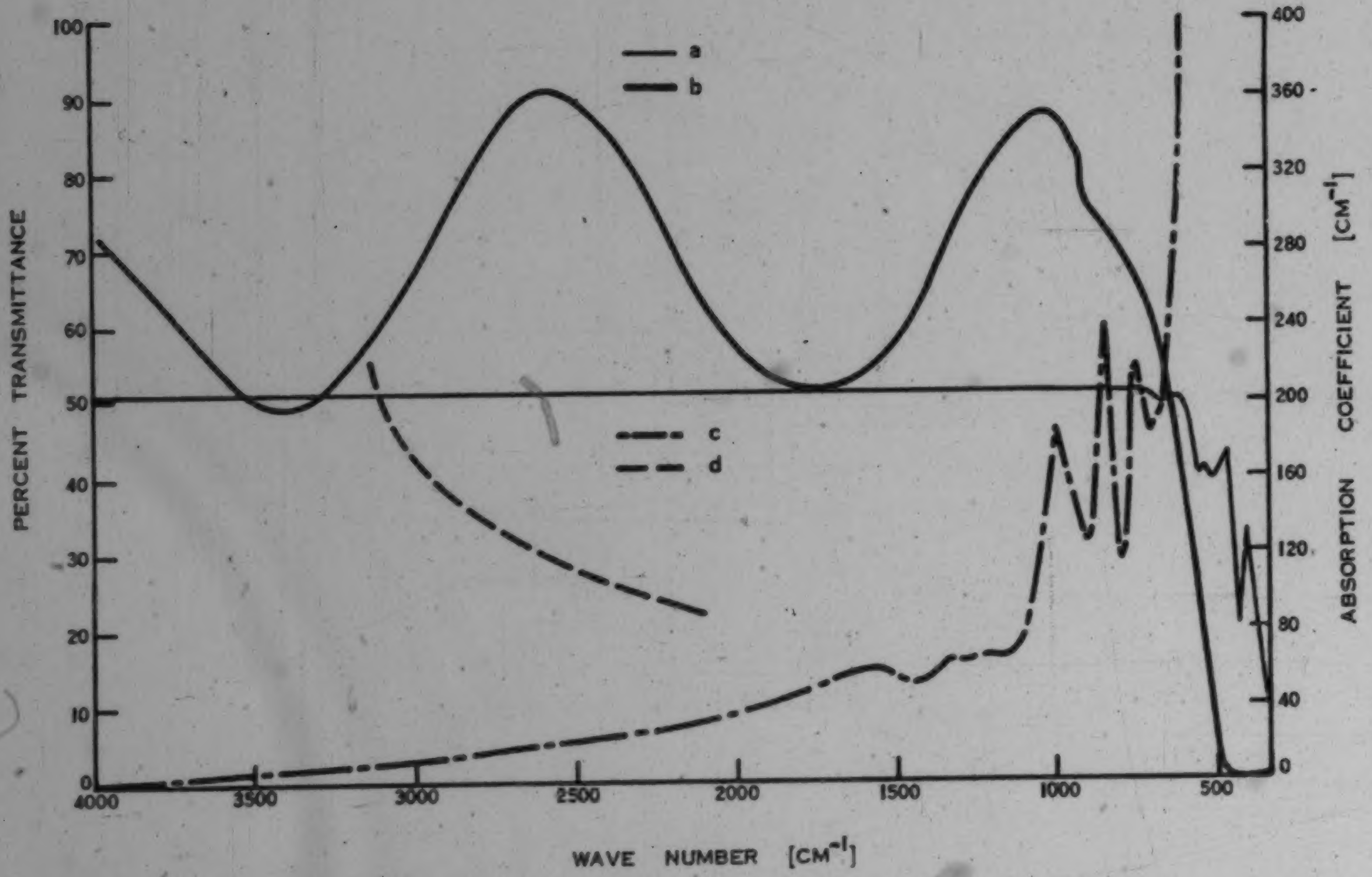

Fig. 3.14 Infrared Spectrophotometer Scans on: (a) uncoated single crystal germanium; (b) germanium substrate A.R. coated with ZnO on both sides.
Infrared Absorption Spectra on: (c) bulk single crystal Zinc Oxide [3.10,3.11]; (d) Tungsten Oxide (not to scale) [3.12].

### 3.7 Discussion

In a review paper on fiber texture Bauer states that materials crystallizing in a hexagonal structure have a strong tendency to exhibit perpendicular <0001> orientation at normal vapor beam incidence. However, he also points out that the orientational behavior of reactive materials in active residual gases is difficult to predict [3.14]. In view of these statements and the above experimental results the following explanation is suggested for the orientational dependence of ZnO thin films on gold nucleating surfaces and the oxygen content in the sputtering gas mix.

The strong influence of the gold nucleating under-lay on ZnO may be accounted for by three coincidences; first, for gold ($a_o$ = 4.078 Å, f.c.c.) the spacing between atoms in the (111) plane is 2.88 Å which is within 15% of the '$a_o$' lattice constant of ZnO, namely 3.25 Å; second, the $d_{111}$ spacing of gold is 2.355 Å while the $d_{0002}$ spacing of ZnO is 2.6 Å, again less than a 15% difference and; third, both the <111> direction in a face-centered cubic lattice and the <0001> direction in a hexagonal lattice are three-fold symmetry axes. It has been suggested that the last coincidence is primarily responsible for the influence a nucleating surface may have on an overlaying thin film [3.15].

Whenever compounds are sputtered there will be some non-molecular deposition. Consequently when sputtering ZnO onto amorphous glass with no oxygen added to the sputtering gas mix, one would expect some loss of oxygen to the gas phase and subsequent depostion of excess atomic zinc at the substrate surface. This zinc may remain uncombined or be forced to react with residual gas atoms. These non-oxide zinc compounds would crystallize in different habits and this have a randomizing influence on the necessarily smaller ZnO crystals. As the oxygen content is increased, the anticipated <0001> fiber texture begins to develop and the grain size increases, however, the film becomes mechanically unstable. It is recognized that the stress developed in a thin film is influenced by many factors, including stoichiometry and texture [3.16]. Upon further increasing the oxygen content to approximately 60% the film again becomes mechanically stable and exhibits a definite <0001> perpendicular orientation. This percentage of oxygen required to achieve films with compatible orientation and stability is very much higher than expected from purely stoichiometric considerations. This implies a second oxygen dependent texture mechanism; possibly the need for 'energetic' oxygen atoms at the substrate surface. Oxygen being electronegative, ionizes negatively and will be accelerated away from the target toward the substrate. Not only will this provide energetic oxygen ions at the substrate but this will also result in substrate surface charge effects, which are known to affect thin film growth mechanisms [3.17]. The results of Fig. 3.10a seem to support this hypothesis since, for a similar level of orientation as that depicted in Fig. 3.6c substantially less oxygen was required. In the former case, the necessary nucleation was provided by the gold thin film.

The electron probe results, were believed to be accurate to within 1% for the assumed composition namely a film composed of zinc and oxygen. However, in the case of $P_{O_2}$ = 0% the concentration of argon in the film may have been significant. This being the case, the weight concentration of zinc computed would be somewhat altered. In any case, the weight concentration of zinc in the films deposited with $P_{O_2}$ = 0% and $P_{O_2}$ = 60%

was not substantially different.

The physical constants determined, band gap energy and infrared refractive index, were within 5% of the values previously reported. An indication of the wavelength location, but not magnitude, of the major infrared lattice absorption peaks of ZnO were observed from infrared spectrophotometric scans of ZnO, A.R. films on germanium.

## 3.8 Conclusion

The ZnO thin films have been analysed for structure and for composition.

The results show that repeatable, highly oriented, stable ZnO thin films may be consistently produced by deposition at high supersaturations onto a highly oriented gold thin film nucleating surface with a high partial pressure of oxygen in the sputtering gas mix.

Because ZnO is a semiconductor small changes in stoichiometry have a considerable influence on the film. Most drastically affected are the film structure, level of stress, appearance and resistivity. Measurement of the latter would probably offer the most sensitive method of assessing the relative oxygen contents in a collection of ZnO thin films.

The principle objective of this work was to fabricate high quality thin film transducers for acoustic and acousto-optic studies. As a result the purely thin film investigation was not complete. A more thorough investigation would include: determining the effect of changes in total pressure (keeping $P_{O_2}/P_{A_r}$ fixed) on film structure and stress level; investigating many more substrate surfaces for their influence on ZnO thin films, in particular to more clearly characterize what will constitute a favorable nucleating surface and; microprobing the films for elements other than zinc, in particular, argon.

# CHAPTER IV

# TRANSDUCER FABRICATION AND EVALUATION

## 4.1 Introduction

For infrared radiation in the 5 - 20μ range there are at present, essentially only two materials suitable for acousto-optic modulation [4.1]. Tellurium has the highest figure of merit ($\Psi$ = 2920), however, besides being difficult to obtain in large pieces of good optical quality it has an optical absorption coefficient of 0.3 $cm^{-1}$ at 10.6μ, which makes it unsatisfactory for intracavity modulation or high power laser deflection at this wavelength. Germanium, possesses a $\Psi$ = 540 but has an optical absorption coefficient which may be reduced to .01 $cm^{-1}$ at 10.6μ by appropriate cooling. Also, it is readily available in large, single crystals of good optical quality. Consequently, in this chapter the acousto-electric performance of ZnO thin film transducers deposited onto the <111> face of a 1 inch germanium cube will be discussed.

In the next section a detailed description of the transducer fabrication process is given. A mathematical model of the transducer and delay medium is outlined in Section 4.3. Based on this theory, an APL computer program (Appendix I) was written to compute a set of insertion loss versus frequency curves for different values of $k_t$. In Section 4.4 the technique for measuring the insertion loss is presented. As expected, the echo patterns obtained indicated that the acoustic losses due to diffraction from the transducer and intrinsic attenuation in germanium were significant. These losses were considered in Section 4.5. A formula is given to estimate the diffraction losses and also, the measured intrinsic acoustic attenuation for the germanium crystal is presented. In Section 4.6 the value of $k_t = .25$ for a ZnO thin film transducer is obtained by comparing the corrected experimental data with the computed values. The chapter is followed by a conclusion.

## 4.2 Transducer Fabrication Recipe

The specific deposition parameters for the 'All' sputtered transducers are listed in Table 4.1.

Prior to introducing the sputtering gas the filaments were outgassed for fifteen minutes. To insure that the diffusion pump pressure did not rise above $5\times10^{-4}$ Torr and to conserve the ultra-pure gases, the high vacuum valve was mechanically throttled. The gas flow was then initiated. The chamber pressure was kept at $5\times10^{-4}$ Torr of Argon when sputtering the metal targets and 6μ of Ar and $O_2$ in a 40% - 60% ratio when sputtering ZnO. In this case, after turning on the filaments, an immediate reduction in the total pressure of ∿ 1μ would occur. The pressure would then relax exponentially,back to a value ∿ .3μ less than the initial total pressure. Only the oxygen content was found to vary and therefore the system was subsequently 'topped-up' with additional oxygen.

The targets were presputtered and the substrate surfaces plasma cleaned for 30 minutes prior to deposition. The plasma cleaning was accomplished by grounding the substrate table and fully inserting it

## TABLE 4.1

## Sputtering Parameters

| | Cr. | Au. | ZnO |
|---|---|---|---|
| Anode current-amps | 2.5 | 2.5 | 2.5 |
| Target Current Density-ma/cm$^2$ | 1.1 | 1.0 | 2.25 |
| Target Voltage-volts | 1500 | 2500 | 1600 |
| Target to Substrate Distance -cm | 5 | 5 | 5 |
| Axial Magnetic Field-gauss | 120 | 120 | 120 |
| Chamber Pressure -Torr | $5\times10^{-4}$ | $5\times10^{-4}$ | $6\times10^{-3}$ |
| Deposition Rate -Å/min | 125 | 250 | 300 |
| Sputtering Gas | Ar | Ar | $Ar+O_2$ |
| Sputtering Gas Mix-% | 100 | 100 | 40+60 |

into the plasma. For this process the axial magnetic field was removed so that the plasma was no longer confined and consequently enveloped the substrate.

The commercial targets, Cr and Au from 'Materials Research Corp' and the ZnO target from 'Sloan Materials Division', were two inches in diameter. Their voltage and current could be coarsely adjusted by positioning the probe relative to the plasma as well as varying the anode current. It was found that only the latter was necessary when the target was positioned at the edge of the plasma. Fine control was subsequently achieved by varying the magnetic field.

Although it was advantageous to deposit the Cr, Au and ZnO films without breaking the vacuum, this was not feasible for the thick ZnO films required. The vacuum was broken after the germanium substrate surface was metallized, and a clean main liner inserted. This procedure was made necessary because the ZnO on the metallized liner surfaces became oriented and consequently stressed. When these films fractured the chamber debris became utterly intolerable. Not only did the flaking occur much sooner but also it was much more extensive. As explained in Chapter II, even with a clean liner, the ZnO coating on it would eventually break away creating a dust problem.

In order to fabricate a transducer resonant at 400 MHz a film 6.5μ thick was required. Even at the high deposition rates employed here, 215 min. of deposition was needed. Since the filament lifetime in the oxygen rich atmosphere was only 150 min, the deposition process was interrupted after ∿ 100 min. of deposition and the alternate filament activated. It should be noted here that unlike the findings of Winslow et al., the formation of an inactive layer,due to the interruption in the deposition, was not observed [4.2].

No special substrate temperature control was found necessary during deposition of the ZnO films. Due to plasma heating, however, the temperature of the support table rose from 75°C to 150°C during the deposition period. The support table was electrically floating during deposition. This was not absolutely necessary, however, it served to prevent the discharge from arcing to the substrate when the filament current was not sufficient to supply enough electrons to support the discharge. The germanium substrate was cleaned simply by washing in a soap and water solution, rinsing in distilled water and drying in clean $N_2$ gas.

A 2000 Å layer of ZnS was evaporated on the sputtered Cr-Au-ZnO combination to insure against the active medium being shorted out during the deposition of the large area top electrode. Other than mass loading, this caused little deterioration in the overall transducer performance due to the acoustical ($Zo = 22.5\text{x}10^6$ kgm/sec $m^2$) and electrical ($K_{ZnS} = 8.35$) similarity with ZnO ($Zo = 36.4\text{x}10^6$ kgm/sec $m^2$, $K = 8.5$). In order to eliminate the possibility of an air gap, a 1000 Å aluminum top electrode was evaporated on the ZnS layer to complete the transducer. An aluminum rather than a gold electrode was selected primarily because of its superior adherence, but also to reduce the mass loading on the transducer [4.3].

## 4.3 Mathematical Model of Complete Electro-Acoustic System

The physical structure to be modelled is shown in Fig. 4.1. Each layer may be represented by a matrix thereby permitting the complete structure to be analysed by a simple matrix multiplication technique.

The equivalent circuit shown in Fig. 4.2 can be used to characterize the active medium provided: (1) there is only one mode of propagation; (2) the lateral dimensions are much larger than the thickness and; (3) the active layer is loss free [4.4, 4.5]. The piezoelectric layer is characterized by its density $\rho_3$, dilatational acoustic velocity $v_3^d$, thickness $d_3$, the dielectric impermeability at constant strain $\beta_{33}^S$, elastic constant $C_{33}^D$ and thickness coupling coefficient $k_t$. The relations

$$Zo_3 = \rho_3 v_3^d S , \qquad (4.1)$$

$$\gamma_3 = \frac{\omega d_3}{v_3^d} , \qquad (4.2)$$

$$C_o = \frac{S}{\beta_{33}^S d_3} , \qquad (4.3)$$

$$v_3^d = \left(\frac{C_{33}^D}{\rho_3}\right)^{1/2} \qquad (4.4)$$

and $$\phi = C_o h_{33} = \frac{S}{d_3}\left(\frac{C_{33}^D}{\beta_{33}^S}\right)^{1/2} k_t = \left[\frac{\omega_o C_o Zo_3 k_t^2}{S\pi}\right]^{1/2} , \qquad (4.5)$$

where $S$ = transducer area,

$h_{33}$ = piezoelectric tensor component expressed in matrix notation,

$C_{33}^D$ = elastic stiffness tensor component measured under a constant electric displacement, expressed in matrix notation,

$Zo_3$ = characteristic acoustic impedance of layer number 3, the ZnO thin film,

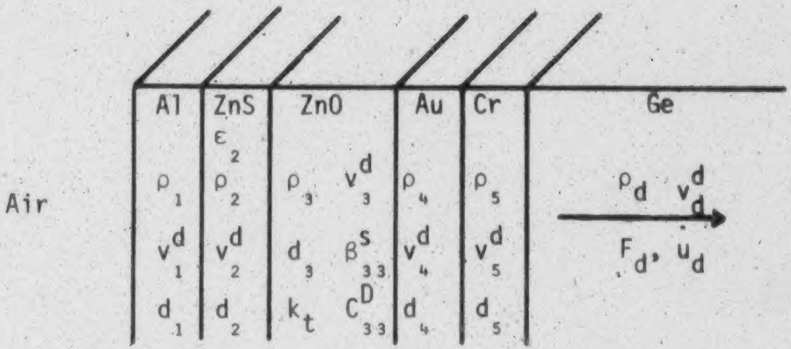
Air
Al
ZnS
ZnO
Au
Cr
Ge
$\varepsilon_2$
$\rho_1$ $\rho_2$ $\rho_3$ $v_3^d$ $\rho_4$ $\rho_5$
$v_1^d$ $v_2^d$ $d_3$ $\beta_{33}^s$ $v_4^d$ $v_5^d$
$d_1$ $d_2$ $k_t$ $C_{33}^D$ $d_4$ $d_5$
$\rho_d$ $v_d^d$
$F_d$, $\dot{u}_d$

Fig. 4.1 Layered Structure to be Modelled.

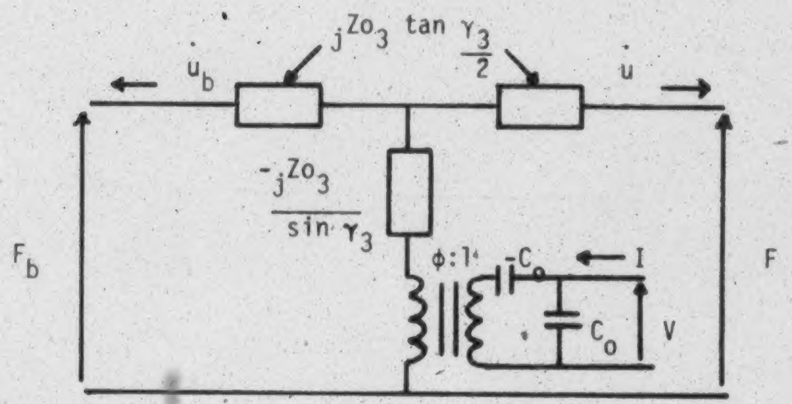
$\dot{u}_b$
$jZo_3 \tan \frac{\gamma_3}{2}$
$\dot{u}$
$\frac{-jZo_3}{\sin \gamma_3}$
$F_b$
$\phi:1$
$-C_o$
I
$C_o$
V
F

Fig. 4.2 Equivalent Circuit of Active Layer.

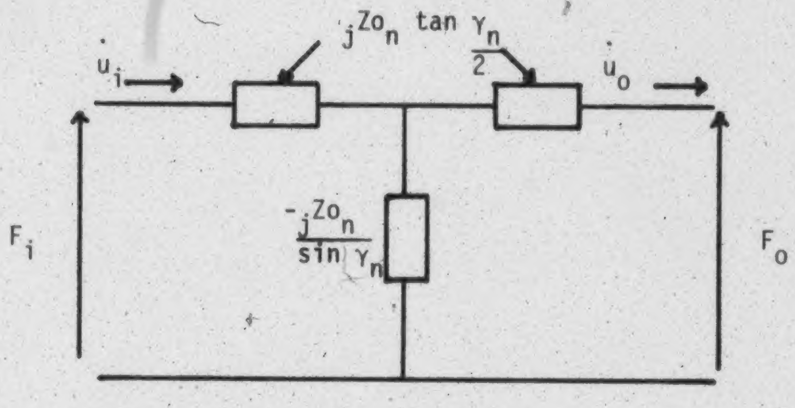
$\dot{u}_i$
$jZo_n \tan \frac{\gamma_n}{2}$
$\dot{u}_o$
$\frac{-jZo_n}{\sin \gamma_n}$
$F_i$
$F_o$

Fig. 4.3 Equivalent Circuit of Inactive Layer.

$C_o$ = clamped capacitance,

$\gamma_3$ = phase constant,

$\phi$ = electro-mechanical transformer turns ratio,

$\omega$ = $2\pi f$

and $f$ = frequency ,

define the values appearing in the equivalent circuit of Fig. 4.2.

The equivalent circuit shown in Fig. 4.3 can be used to characterize an inactive layer provided it is not lossy, does not convert one mode of propagation into another and has lateral dimensions comprising many acoustic wavelengths. It can be seen that this circuit is essentially the same as that shown in Fig. 4.2 with $\phi = 0$. The inactive layer, therefore, acts as a lossless transmission line section. Similar expressions as (4.1), (4.2) and (4.4) apply to this equivalent circuit where the material values for the respective layer are substituted. The matrix relating the mechanical force $F_i$ and particle velocity $\dot{u}_i$ at the input port, to that $(F_o, \dot{u}_o)$ at the output port for this circuit is:

$$M_n^a = \begin{bmatrix} \cos\gamma_n & jZo_n \sin\gamma_n \\ \dfrac{j \sin\gamma_n}{Zo_n} & \cos\gamma_n \end{bmatrix} \qquad (4.6)$$

$$\text{where} \begin{bmatrix} F_i \\ \dot{u}_i \end{bmatrix} = M_n^a \begin{bmatrix} F_o \\ \dot{u}_o \end{bmatrix} , \qquad (4.7)$$

In order to express the input voltage and current to the transducer in terms of the force and particle velocity delivered to the delay medium we must determine the acoustic impedance of the backing layers, $F_b/\hat{u}_b$, seen by the top surface of the transducer. This is done by matrix multiplication as follows:

$$\begin{bmatrix} F_b \\ \\ \hat{u}_b \end{bmatrix} = M_2^a \, M_1^a \begin{bmatrix} F_{air} \\ \\ \hat{u}_{air} \end{bmatrix}$$

$$= \begin{bmatrix} A_b & B_b \\ \\ C_b & D_b \end{bmatrix} \begin{bmatrix} F_{air} \\ \\ \hat{u}_{air} \end{bmatrix} \qquad (4.8)$$

where $\dfrac{F_{air}}{\hat{u}_{air}} \cong 0$ ,

$M_2^a = M_{ZnS}^a$

and $M_1^a = M_{A\ell}^a$ ;

therefore $Z_b \equiv \dfrac{F_b}{\hat{u}_b} = \dfrac{B_b}{D_b}$

$$= jZ_b'$$

$$= j\frac{Zo_1 \cos\gamma_2 \sin\gamma_1 + Zo_2 \sin\gamma_2 \cos\gamma_1}{\cos\gamma_2 \cos\gamma_1 - \dfrac{Zo_1}{Zo_2} \sin\gamma_2 \sin\gamma_1} \ . \qquad (4.9)$$

The equivalent circuit for the transducer and delay medium is now as shown in Fig. 4.4. The effect of the backing layers is represented by introducing $jZ_b'$ and the series capacitance due to the ZnS layer is accounted for by introducing $C_{se}$. By the appropriate matrix multiplication similar to that used to determine $Z_b$, the intermediate layers are taken into consideration. The delay medium is represented by $Zo_d$. From this equivalent circuit the relationship between the electrical input and mechanical output is given by

$$\begin{bmatrix} V \\ I \end{bmatrix} = M \begin{bmatrix} F_d \\ \dot{u}_d \end{bmatrix} \tag{4.10}$$

$$\text{where } M = M_2^e \; M_3^{e-a} \; M_4^a \; M_5^a = \begin{bmatrix} A^T & B^T \\ C^T & D^T \end{bmatrix}, \tag{4.11}$$

$$M_2^e = M_{ZnS}^e = \begin{bmatrix} 1 & \frac{1}{j\omega C_{se}} \\ 0 & 1 \end{bmatrix}, \tag{4.12a}$$

$$C_{se} = C_{ZnS} = \frac{K_{ZnS}\varepsilon_o S}{d_2}, \tag{4.12b}$$

$$M_3^{e-a} = M_{\substack{ZnO \\ \& \text{ backing}}}^{e-a} = \left[\begin{pmatrix} \frac{1}{\phi} & 0 \\ 0 & 0 \end{pmatrix} + j \begin{pmatrix} 0 & \frac{\phi}{\omega C_o} \\ \frac{\omega C_o}{\phi} & 0 \end{pmatrix}\right] \times$$

$$\left[\begin{pmatrix} A_t & 0 \\ 0 & D_t \end{pmatrix} + j \begin{pmatrix} 0 & B_t \\ C_t & 0 \end{pmatrix}\right], \tag{4.13}$$

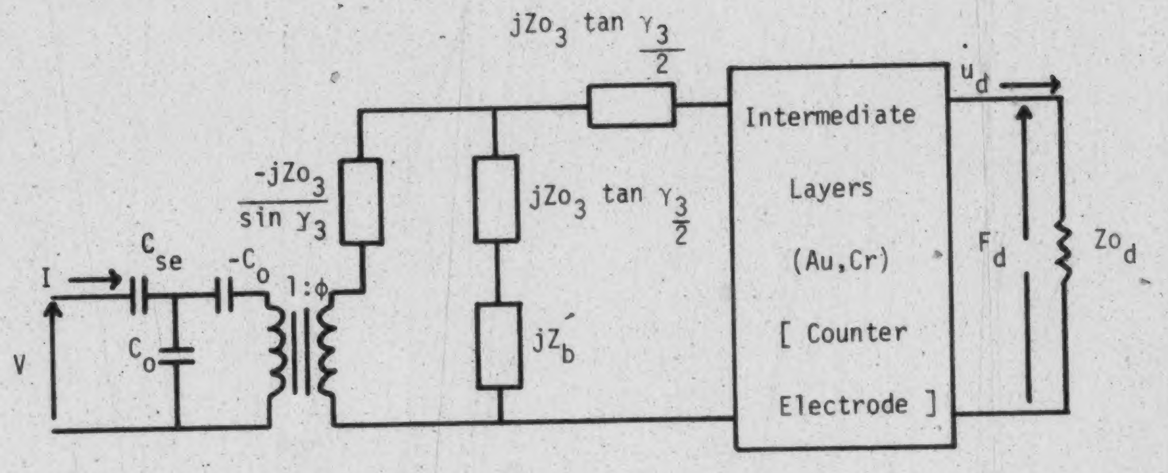

Fig. 4.4 Equivalent Circuit for Determining 'M'.

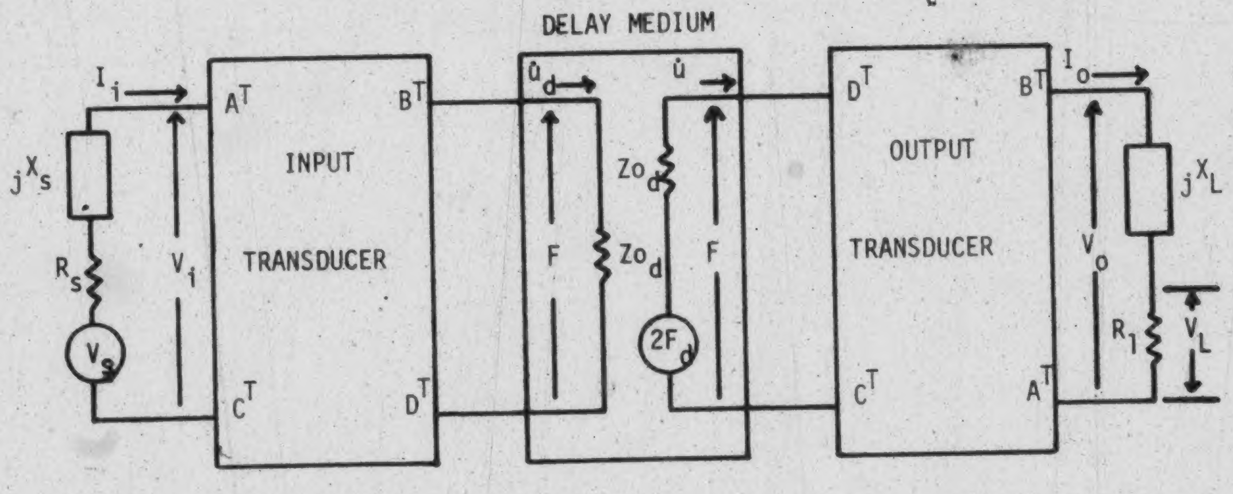

Fig. 4.5 Circuit for Insertion Loss Calculation.

$$A_t = \frac{\cos\gamma_3(\cos\gamma_3 - 1) - z_b^2 \sin^2\gamma_3 + z_b \sin\gamma_3}{\text{C.D.}} , \quad (4.14)$$

$$B_t = \frac{Zo_3 z_b (1 - \cos\gamma_3) + Zo_3 \sin\gamma_3 (\cos\gamma_3 (1 - z_b^2) - 1)}{\text{C.D.}} , \quad (4.15)$$

$$C_t = \frac{1}{Zo_3} \left[ \frac{z_b \sin^2\gamma_3 + \sin\gamma_3(\cos\gamma_3 - 1)}{\text{C.D.}} \right] , \quad (4.16)$$

$$D_t = \frac{2(\cos\gamma_3 - 1)^2 - z_b \sin\gamma_3 (z_b \sin\gamma_3 + 1 - \cos\gamma_3)}{\text{C.D.}} , \quad (4.17)$$

$$\text{C.D.} = (\cos\gamma_3 - 1)^2 - z_b^2 \sin^2\gamma_3 , \quad (4.18)$$

$$z_b = \frac{Z_b'}{Zo_3} , \quad (4.19)$$

$$M_4^a = M_{Au}^a , \quad (4.20)$$

$$M_5^a = M_{Cr}^a \quad (4.21)$$

and

$$Zo_d = \rho_d v_d^d S = \frac{F_d}{\dot{a}_d} . \quad (4.22)$$

The program Trans3 given in Appendix I calculates the matrix elements $A^T$, $B^T$, $C^T$ and $D^T$ for different values of the coupling coefficient over the frequency range 50 MHz to 1 GHz.

In order to calculate the insertion loss the circuit shown in Fig. 4.5 must be evaluated. This circuit is valid if the input pulse is short enough so that the output transducer does not interact with the input transducer.

From $V_s = IZ_s + V$ (4.23)

where $V = A^T F_d + B^T \dot{u}_d$ (4.24)

and $I = C^T F_d + D^T \dot{u}_d$ (4.25)

we obtain $$\frac{V_s}{F_d} = \left[\frac{(Zo_d C^T + D^T)Z_s + (A^T Zo_d + B^T)}{Zo_d}\right] \quad (4.26)$$

where $Z_s = R_s + jX_s$, source impedance. (4.27)

The insertion loss is given by

$$\begin{aligned} \text{I.L.} &= 20 \log \left|\frac{V_s}{V_L}\right| \left(\frac{R_L}{R_s + R_L}\right) \\ &= 20 \log \left|\frac{V_s}{V_L}\right| + 20 \log\left(\frac{R_L}{R_s + R_L}\right) \quad (4.28) \end{aligned}$$

therefore, we require the expression for $F_d/V_o$. From equation (4.10)

$$\begin{bmatrix} V_o \\ -I_o \end{bmatrix} = \underline{M} \begin{bmatrix} F \\ -\dot{u} \end{bmatrix} = \begin{bmatrix} A^T & -B^T \\ -C^T & D^T \end{bmatrix} \begin{bmatrix} F \\ -\dot{u} \end{bmatrix} \quad (4.29)$$

Therefore $$\begin{bmatrix} F \\ -\dot{u} \end{bmatrix} = \underline{M}^{-1} \begin{bmatrix} V_o \\ -I_o \end{bmatrix} \quad (4.30)$$

From matrix theory the elements of $\underline{M}^{-1}$ are given by

$$(\underline{m_{ij}})^{-1} = \frac{\Delta_{ji}}{|\underline{M}|}$$

where $\Delta_{ji} = (-1)^{j+i}|\underline{M_{ji}}|$ , the cofactor of $\underline{m_{ji}}$ ,

$|\underline{M_{ji}}|$ = determinant of $\underline{M}$ where the $j^{th}$ row and $i^{th}$ column have been deleted

and $|\underline{M}|$ = determinant of the matrix $\underline{M}$ [4.6].

Since $|\underline{M}| = +1$, the elements of $\underline{M}^{-1}$ in terms of the matrix elements of M will be

$$\underline{M}^{-1} = \begin{bmatrix} D^T & +B^T \\ +C^T & A^T \end{bmatrix} \tag{4.31}$$

$$\text{therfore} \begin{bmatrix} F \\ U \end{bmatrix} = \begin{bmatrix} D^T & B^T \\ C^T & A^T \end{bmatrix} \begin{bmatrix} V_o \\ I_o \end{bmatrix} \tag{4.32}$$

for the directions shown in Fig. 4.5. Therefore, for the receiving circuit

$$2F_d - UZo_d = F \ , \tag{4.33}$$

$$V_o = I_oZ_L \tag{4.34}$$

and $$Z_L = R_L + jX_L \ , \text{ load impedance.} \tag{4.35}$$

By using equations (4.32) through (4.35) we obtain,

$$\frac{F_d}{V_o} = \frac{Z_L(Zo_dC^T+D^T) + (A^TZo_d+B^T)}{2Z_L} \tag{4.36}$$

If we consider the untuned case, $X_S = X_L = 0$ and $V_o = V_L$ then, combining equation (4.26) and (4.36) we obtain

$$\frac{V_s}{V_L} = \frac{[(Zo_d C^T + D^T)R_s + (A^T Zo_d + B^T)][R_L(Zo_d C^T + D^T) + (A^T Zo_d + B^T)]}{2R_L Zo_d} \tag{4.37}$$

The program ILTRANS, given in Appendix I in conjunction with the program TRANS3 calculates the theoretical insertion loss versus frequency for different values of the coupling coefficient.

## 4.4 Insertion Loss Measurement

It can be shown that the bandshape function for untuned transducers with $k_t^2 << 1$ and a contact impedance much less than 50Ω is given by

$$BS(f) \cong \frac{\pi Zo_d}{16k_t^2 Zo_3}\left[\frac{1 + (\omega C_o R_s)^2}{\omega_o C_o R_s}\right] \text{ [4.7]}. \tag{4.38}$$

This is a minimum for $\frac{1}{\omega_o C_o} = R_s$. Since $\omega_o$ is specified by the system application, the area of the top electrode was made small enough ($R = .012$ inches) so that BS(f) was minimized. This transducer was, of course, not suitable for acousto-optic or attenuation studies due to the divergence of the acoustic beam caused by diffraction. These acoustic losses will be discussed in the next section.

The pulsed R.F. insertion loss measurements were made in the 50Ω coaxial system shown in Fig. 4.6. The input pulsed signal entered a well padded hybrid junction where it was divided equally and fed to the delay line and a reference path containing a precision attenuator. The

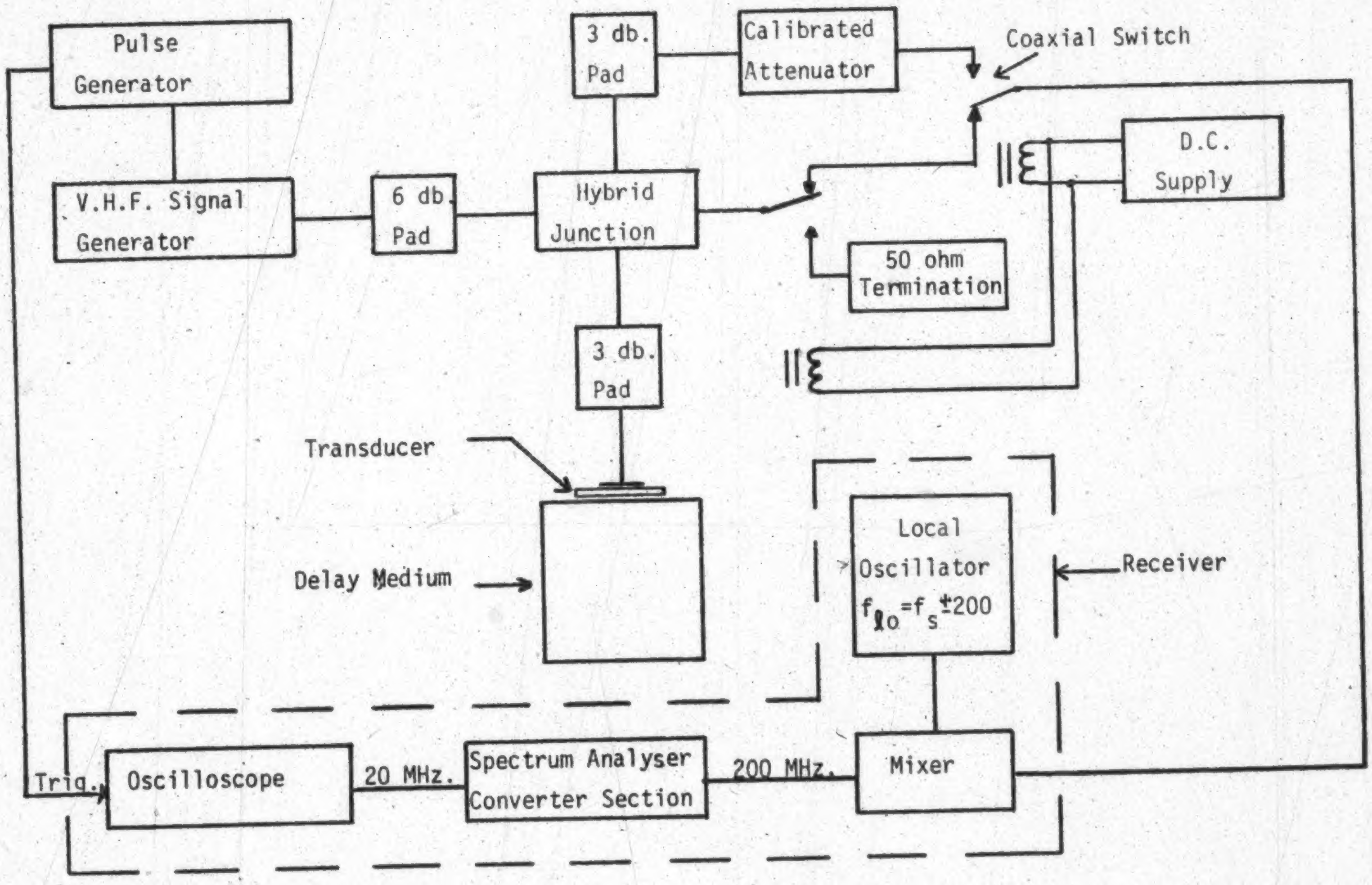

Fig. 4.6 Insertion Loss Measurement Circuit.

reflected pulse and echoes from the delay line were directed to the output port. A coaxial switch at the input to the heterodyne receiver selected either the delay line or the reference output. The insertion loss was given by the difference in attenuation between the reference and delay-line paths when the two receiver output signals were adjusted for equal amplitudes using the precision attenuator. For tuned measurements the tuning network was simply inserted between the 3 db pad and transducer.

In Fig. 4.7 the hardware used in the acoustic studies is shown. The germanium cube is mounted in a water cooled holder which may be filled with mercury for an anechotic termination. The germanium brick in this photograph has ZnO thin films deposited on two adjacent sides. The ZnO film on one side was sputtered onto an evaporate gold surface while that on the other was deposited onto a sputtered gold surface. Note the coaxial coupler used for access to the transducers.

## 4.5 Acoustic Losses

In order to be able to compare the measured insertion loss with the computed (which assume no acoustic losses) data,the acoustic losses must be determined. The significant acoustic losses are due to beam spreading and attenuation in the delay medium.

### 4.5.1 Diffraction Losses

The problem of acoustic diffraction has been considered in detail [4.8, 4.9]. For a circular transducer which acts as the transmitter and receiver, the echo pattern for wavelengths in the order of the transducer

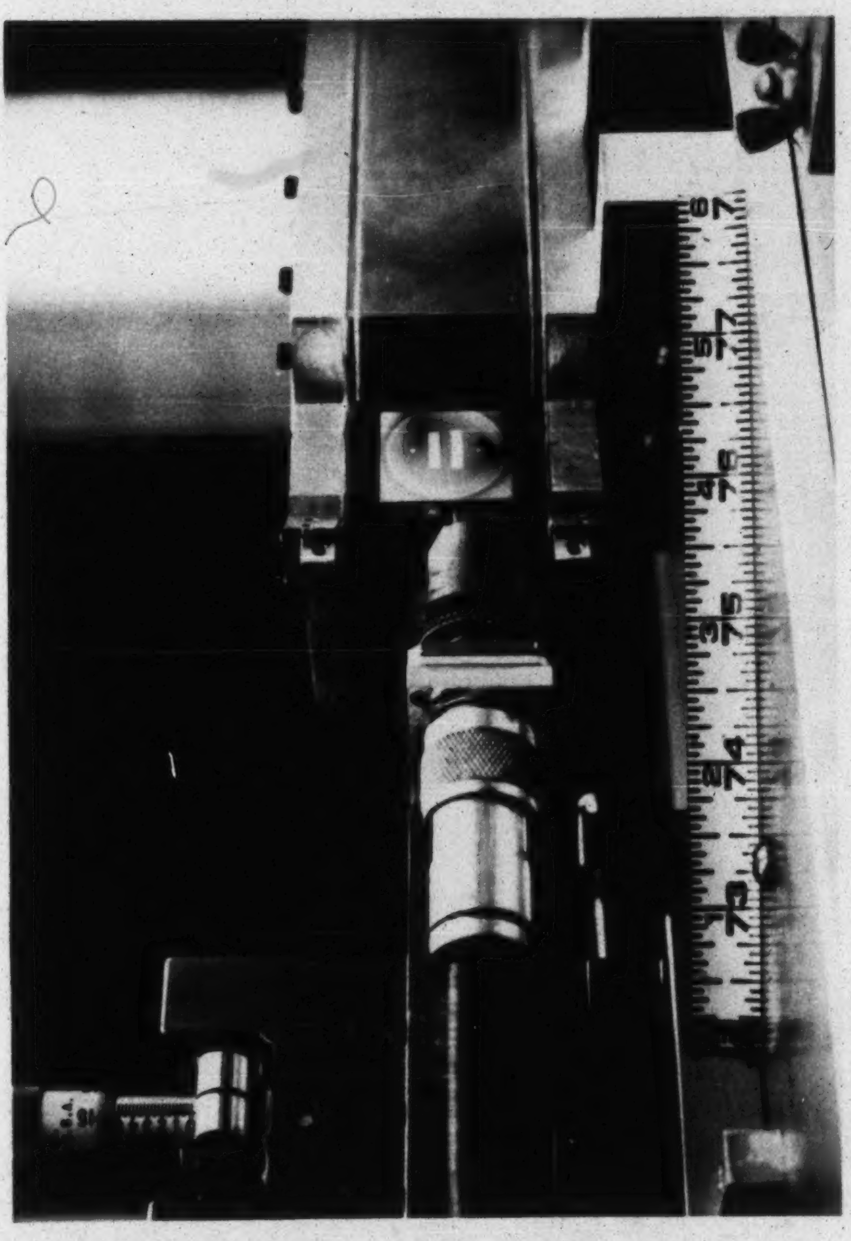

Fig. 4.7 Stainless Steel Mount for Germanium Cubes; U.H.F. Coupler.

dimensions is not a simple exponential as would be expected from intrinsic attenuation. In the region near the transducer the phase of the acoustic pressure wave is not constant across the plane perpendicular to the direction of propagation. The magnitude of the echoes in this region can be calculated by two integrations. The first is over the source area to determine the near acoustic field pattern in a manner analogous to the determination of the Fresnel field produced by a plane wave incident on an aperture. The second is over the area of the receiver upon which the non-plane wave is incident, to determine the average pressure hence the magnitude of the output electrical signal. The existence of these fluctuations in the echo pattern verifies the existence of diffraction. This affect is shown in Fig. 4.8 for a transducer having 1.9 mm as its smallest dimensions at 50 MHz. From the analysis outlined above it can be shown that an estimate of the average diffraction loss is given by

$$\alpha_d = \frac{a^2}{\Lambda} \left(\frac{db}{cm}\right) \tag{4.39}$$

where $\alpha_d$ = acoustic loss due to diffraction,
$a$ = half of smallest transducer dimension
and $\Lambda$ = acoustic wavelength [4.8].

As can be seen in Fig. 4.8, at 50 MHz the diffraction losses for this particular transducer are much greater than the intrinsic losses in germanium.

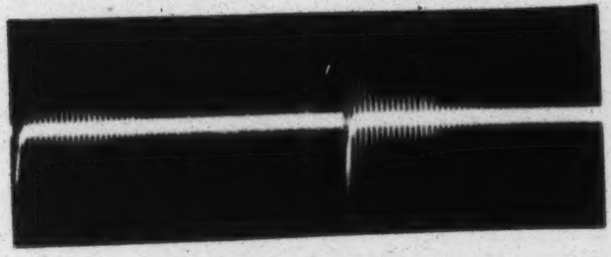

Fig. 4.8 Effects of Acoustic Diffraction on the Compressional Echo Pattern in Germanium. Area = 1.9mm x 5.5 mm; Hor. - 100μsec/cm; Ver. - 20mv/cm; f = 50 MHz.

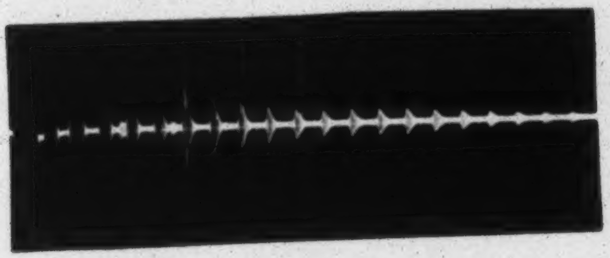

Fig. 4.9 Inadvertently Generated Shear Waves. Area = 1.9mm x 5.5 mm; Hor. - 20μsec/cm; Ver. - 50 mv/cm, f = 100 MHz.

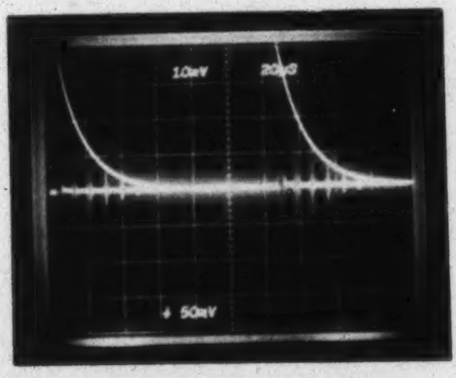

Fig. 4.10 Exponential Decay of Compressional Wave in Germanium at 300°K and 210 MHz - Intrinsic Attenuation; Area = 4.2mm x 5.5 mm.

### 4.5.2 Intrinsic Losses

Mason has considered intrinsic attenuation in Silicon and Germanium in detail [4.10]. Fundamentally acoustic attenuation is due to the anharmonicity in the interatomic force constants of the crystal. These anharmonicities allow phonon-phonon collisions, which in the case of germanium is the most important cause of acoustic attenuation. The thermoelastic effect accounts for only 4% of the measured attenuation. This must be the case, if shear waves are to experience any attenuation at all. The physics of the phonon interaction can be stated simply: the presence of one phonon causes a periodic elastic strain which (through the anharmonic interaction) modulates in space and time the elastic constant of the crystal. The second phonon perceives the modulation of the elastic constant and is thereupon scattered just as photons are scattered by phonons in the acousto-optic effect to be discussed in the next chapter [4.11].

In Fig. 4.9 inadvertently generated shear waves and their attenuation can be seen. The transducer used was the same as that in Fig. 4.8, however, the frequency in this case is 100 MHz. This particular transducer generated shear waves(still ∿ 20 db down from dilatational wave) because the top electrode was near the edge of the ZnO thin film and therefore the applied electric vector was not colinear with the ZnO thin film 'c'-axis. Note that the shear wave acoustic velocity and attenuation are approximately half that of the compressional wave. This is theoretically consistent. In Fig. 4.10 a typical example of dilatational acoustic attenuation at 210 MHz is shown. The transducer in this instance had the dimensions 4.2 mm by 5.5 mm. In Fig. 4.11 the acoustic losses in germanium for a dilatational acoustic wave propagating along the <111>

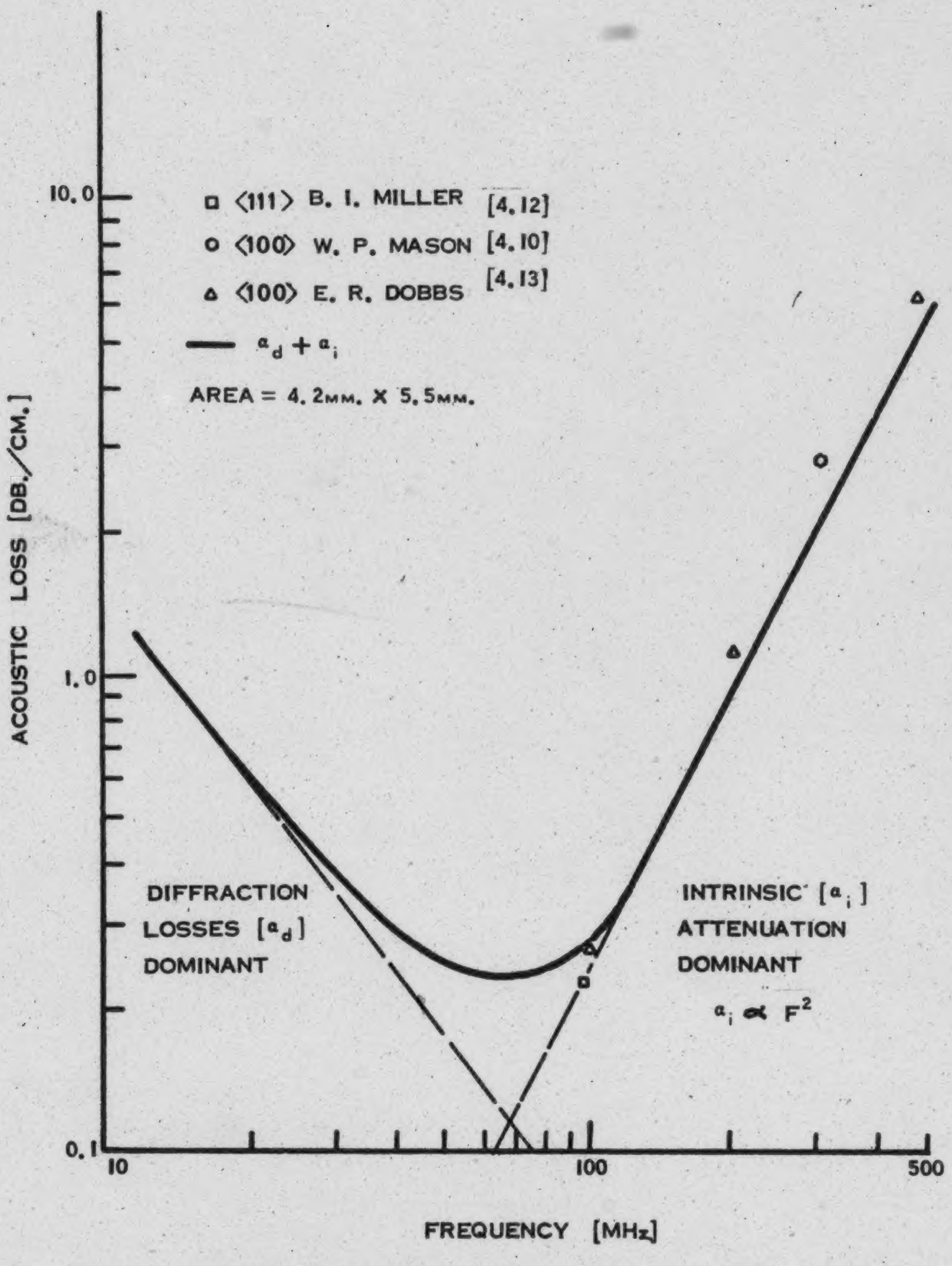

Fig. 4.11 Acoustic Losses in Germanium for Compressional Waves Propagating in the <111> Direction at 300°K.

axis at 300°K for frequencies up to 500 MHz using this transducer are given. This large area transducer was chosen for two reasons; first, to minimize the diffraction effects and second, because this was the transducer employed for the acousto-optic measurements. This intrinsic loss data together with the diffraction attenuation estimates were used to correct the raw insertion loss data for the R = .012 inch transducer. Note that in obtaining this data the relative levels between successive echoes were measured whereas, for insertion loss measurements just the level of the first echo was needed.

## 4.6 Evaluation of Coupling Coefficient

The effective coupling coefficient for the highly oriented ZnO thin film transducers were determined by comparing the untuned corrected (for diffraction and intrinsic losses in germanium) experimental insertion loss data with that generated by a computer program. The material constants $\rho_n$, $v_n^d$, used in the program were obtained from published data on bulk samples. The relative dielectric constant of the ZnO thin film was obtained experimentally using a Wayne-Kerr impedance bridge ($\omega = 10^4$). The value measured was 8.44, closer to the value 8.5 reported by Mason than that given by Meitzler in Table 2.1 [4.14]. As mentioned the film thicknesses were determined with a Taylor-Hobson Tallysurf 4. The material values used were as shown in Table 4.2. This test transducer area was $3.22 \times 10^{-7} m^2$.

In Fig. 4.12 the raw data and corrected data are plotted on a computer generated field of curves with $k_t$ as the adjustable parameter. It can be seen that the ZnO thin film has an effective coupling coefficient greater than .25 or ∿ 90% of the bulk value. Note that the

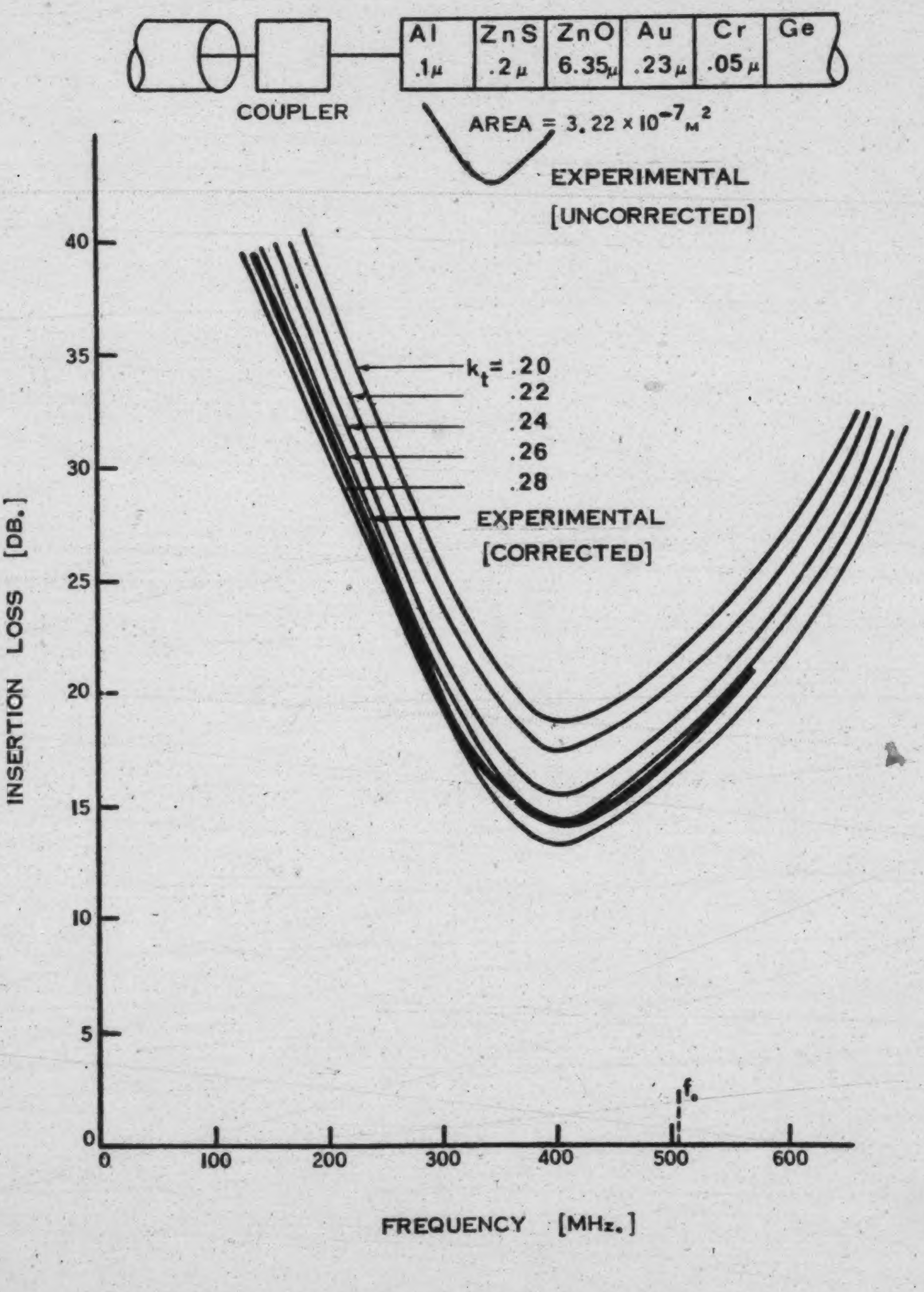

Fig. 4.12 Experimental and Computed Insertion Loss versus Frequency.

TABLE 4.2 Input Data for Computer Program

| Material | $\rho_n x10^3$ (kg/m³) | $v_n^d x10^3$ (m/sec.) | $d_n x10^{-6}$ (m) | $K_n$ | $C_{33}^D x\ 10^{11}$ $(\frac{kgm}{sec.^2 m})$ | Reference |
|---|---|---|---|---|---|---|
| Aluminum | 2.7 | 6.43 | .1 | | | 4.15 |
| Zinc Sulphide | 4.1 | 5.51 | .2 | 8.35 | | 4.16 |
| Zinc Oxide | 5.68 | 6.4 | 6.35 | 8.5 | 2.29 | 4.17 |
| Gold | 19.32 | 3.39 | .23 | | | 4.15 |
| Chromium | 7.2 | 6.55 | .05 | | | 4.18 |
| Germanium | 5.33 | 5.6 | | | | 4.15 |

resonant frequency of the response has been significantly shifted down to ∿ 400 MHz from the resonant frequency of the ZnO thin film itself, $f_o$. This is due to the mass loading by the ZnS and Aℓ layers on the transducer. Therefore, it is apparent that mass loading must be seriously considered when designing high frequency transducers to resonate at a specific frequency. It is thought these results are accurate to within 10%, the sources of error being: (1) the fact that bulk material constants were used and that the corresponding constants of the thin films will be somewhat different; (2) the diffraction loss estimate could be more accurate, however, it is to be recalled that as the frequency increases the diffraction losses become less significant and the intrinsic losses dominate and; (3) the contact resistance of the coupler was not included in the computer program, however, it can be shown that for the untuned measurements on a transducer having $\frac{1}{\omega_o C_o} = R_s$ the error is less than 1 db [4.19].

The last consideration of the previous paragraph does become significant however, when tuned measurements are performed, especially on a large area transducer. In order to evaluate the acousto-optic performance of germanium it was necessary to employ a large area transducer. For sufficient electrical excitation of such a transducer its impedance must be conjugately matched to that of the electrical source for maximum power transfer. In this case, the contact resistance is often equal to or greater than the transducer radiation resistance resulting in a non-zero tuned insertion loss. To be specific, the 4.2 mm x 5.5 mm transducer used in the acoustic loss measurements and employing the same thin film for which a $k_t = .25$ has been established, had a tuned one-way insertion loss at 354 MHz of 11.5 db. Thus more than 9/10 of the input power is being dissipated in the tuning circuit, contact resistance and the resistance of the top electrode. Surprisingly, however, this combined resistance can be shown to amount to only 1.73Ω [4.7]. It should be mentioned here that no effort was made to reduce these losses. One immediate improvement would be to use a gold top electrode ($R_{Au}<R_{A\ell}$) however, this would result in considerable mass loading, a reduction in bandwidth and a slightly higher untuned, minimum insertion loss.

The ZnO film discussed above was deposited on a slowly evaporated gold thin film. As shown it has excellent transducer characteristics however, it is important to note that the gold thin film in this case happened to be highly oriented. Not only that, but as already stated this evaporated-gold-orientation is not nearly as repeatable nor as high as that obtained by sputtering. The resulting variation in the $k_t$ values of different films is continually mentioned (but not necessarily for this reason) in the references cited in the preceding chapters.

It should be noted here that when the orientation in the ZnO thin film reaches a level given by an x-ray diffraction arc half-angle of approximately 6°, the improvement in $k_t$ becomes less significant, being already ∿ 90% of the bulk value. Therefore, in order to guarantee a ZnO thin film having a $k_t$ = .25 it is suggested that a sputtered gold thin film be used as the counter electrode.

## 4.7 Conclusion

In this chapter the fabrication recipe for repeatably producing ZnO thin film transducers having coupling coefficients equal to or greater than 90% of the bulk value, was given. This value of coupling coefficient was arrived at by comparing the measured insertion loss data with that generated on a computer. The mathematical model, based on Mason's transducer equivalent circuit,used for this program was derived and also the values and source of the necessary input data was presented. It was shown that the measured data had to be corrected for relevant acoustic losses, namely diffraction and intrinsic delay medium loss. The latter resulted in the determination of the intrinsic acoustic attenuation in germanium at 300°K for a compressional wave propagating along the <111> axis in the frequency range 50 MHz to 500 MHz. At 500 MHz the attenuation was found to be 5 db/cm thus limiting the usefulness of germanium for acousto-optic studies to frequencies less than 500 MHz. Tuned insertion loss measurements were discussed and the value measured (11.5 db) for the transducer to be used in the acousto-optic investigation was presented.

# CHAPTER V

# ACOUSTO-OPTIC PERFORMANCE OF GERMANIUM EMPLOYING A ZnO THIN FILM TRANSDUCER

## 5.1 Introduction

High frequency, wide-angle acousto-optic diffraction by single crystals finds application in many fields. These include laser modulation and output coupling for use in optical memories and displays; determination of the photoelastic constants of materials and; determination of the magnitude and shape of the pressure waves in a solid by optical probing. Also, there is, as stated in Chapter I, considerable interest in modulation and deflection of 10.6μ $CO_2$ laser radiation for such diverse applications as space communications and micromachining. In this chapter a theory describing the diffraction of electromagnetic (E-M) radiation by acoustic waves in a single crystal is given and the results compared with those obtained experimentally for germanium.

In the following section an expression for the diffraction efficiency as a function of the angle of incidence of the E-M wave on the acoustic wave is derived. It is shown that other than low acoustic and electromagnetic attenuation constants, elasto-optic modulators must possess a high refractive index for large diffraction efficiencies. In Section 5.3 the experimental results are compared with this theory and, the effective photoelastic constant of germanium is evaluated. The chapter is followed by a conclusion.

## 5.2 Theoretical Description of Acousto-Optic Diffraction

The acousto-optic diffraction problem of relating the magnitude and angular dependence of the diffracted intensity to the system geometry and parameters is given by Klein [5.1]. This theory, based on a coupled mode interpretation, is outlined below.

### 5.2.1 Difference Differential Equation

Consider plane, monochromatic radiation incident at an angle $\theta$ (positive in the case shown in Fig. 5.1) on a plane ultrasonic beam of width L.

In the region of the sound wave the optical wave equation can by written

$$\nabla^2 E = \frac{[\zeta(z,t)]^2}{c^2} \frac{\partial^2 E}{\partial t^2} \tag{5.1}$$

with $$\zeta(z,t) = \zeta_o + \zeta' \sin(\Omega t - \kappa z) \tag{5.2}$$

where $\zeta$ = index of refraction in the region of the sound wave,

$E$ = electric field intensity,

$c$ = velocity of light in a vacuum,

$\Omega$ = sound frequency

and $\kappa$ = acoustic wave number.

The amplitude of the electric intensity in the sound beam can be expressed as

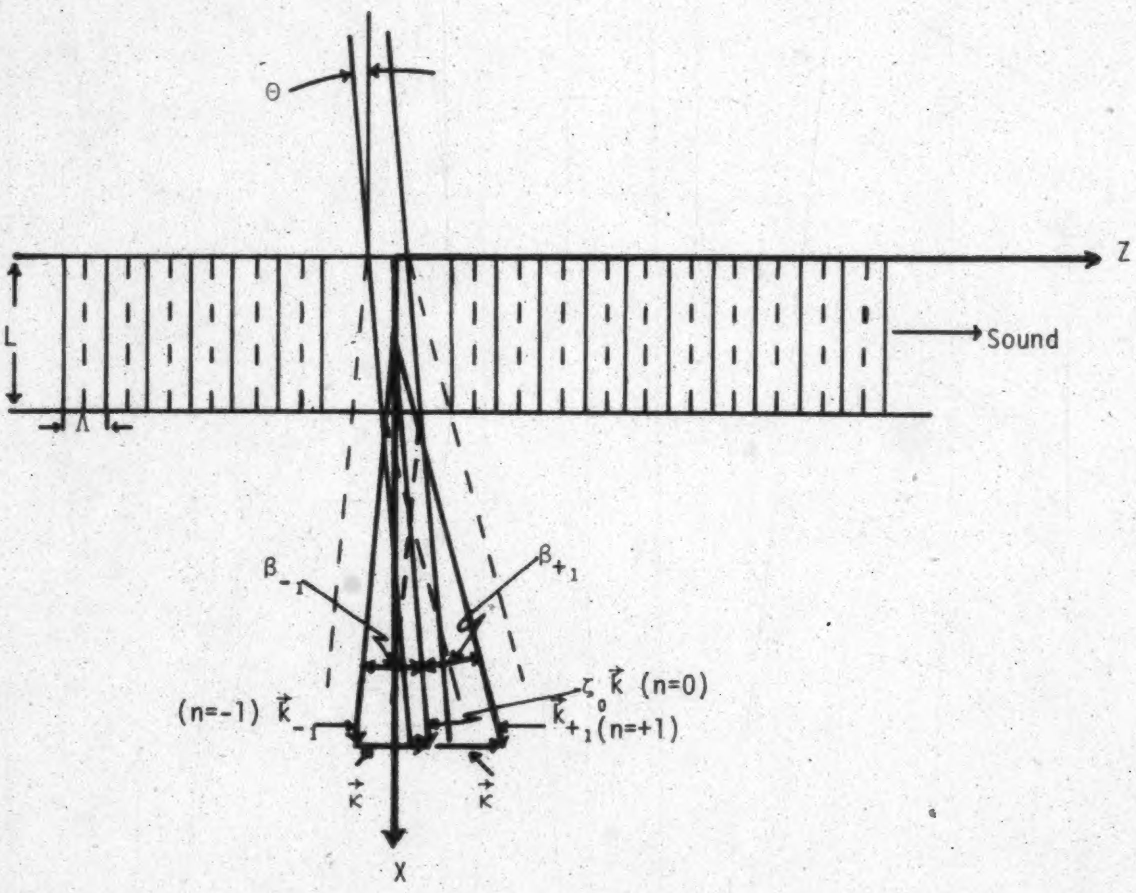

Fig. 5.1 Ultrasonic Diffraction of Electromagnetic Radiation - Orientation of the Partial Wave Vectors n = 0, +1, -1.

$$E = A(x,z,t)\exp[j(\omega t - \zeta_o \vec{k}\cdot\vec{r})] \qquad (5.3)$$

where $\omega$ = radian frequency of the E-M wave,

$A(x,z,t)$ = slowly varying spatial and time dependence of E,

and $k$ = vacuum wave number.

As E is periodic in space and time with the sound field it can be expanded in a Fourier series yielding

$$E = \exp(j\omega t) \sum_{m=-\infty}^{\infty} \Phi_m(x)\exp[j(m\Omega t - \vec{k}_m\cdot\vec{r})] \qquad (5.4)$$

where $\vec{k}_m\cdot\vec{r} = \zeta_o k(z\sin\Theta + x\cos\Theta) + m\kappa z$ (5.5)

and $\Phi_m(x)$ = slowly varying x dependence of E.

Equations (5.4) and (5.5) represent an expansion of E in plane waves where the index m labels the m$^{th}$ Fraunhofer diffraction order.

Substituting equations (5.4) and (5.2) into (5.1) one obtains

$$\exp(j\omega t) \sum_{m=-\infty}^{\infty} \{2j\zeta_o k \cos\Theta \frac{\partial\Phi_m(x)}{\partial x} + (\zeta_o^2 k^2 + 2\zeta_o k\, m\kappa\sin\Theta + m^2\kappa^2)\Phi_m(x)\}\exp[j(m\Omega t - \vec{k}_m\cdot\vec{r})]$$

$$= \exp(j\omega t) \sum_{m=-\infty}^{\infty} \{k^2[\zeta_o^2 + 2\zeta_o\zeta' \sin(\Omega t - \kappa z)]\Phi_m(x)\}\exp[j(m\Omega t - \vec{k}_m\cdot\vec{r})] \qquad (5.6)$$

where $k = \frac{\omega}{c}$

and the following assumptions have been made

$$k^2 \gg \frac{2k\Omega}{c} \qquad (5.7a)$$

$$k^2 \gg \frac{\Omega^2}{c^2} \qquad (5.7b)$$

$$\zeta' \ll \zeta_o \qquad (5.7c)$$

and
$$\frac{\partial\Phi_m(x)}{\partial x} \gg \frac{\partial^2\Phi_m(x)}{\partial x^2} . \qquad (5.7d)$$

By substituting the values given in Section 5.3 into equations (5.7) it can be seen that these assumptions are justified. Now using the identity

$$\sin(\Omega t-\kappa z) = \frac{\exp[j(\Omega t-\kappa z)] - \exp[-j(\Omega t-\kappa z)]}{2j} \qquad (5.8)$$

in equation (5.6) and equating coefficients of the exponentials we obtain the following difference differential equation for $\Phi_n(x)$.

$$\frac{\partial\Phi_n(x)}{\partial x} + \frac{\zeta' k}{2\cos\Theta}[\Phi_{n-1}(x) - \Phi_{n+1}(x)] = j[n\kappa \tan\Theta + \frac{n^2\kappa^2}{2\zeta_o k\cos\Theta}]\Phi_n(x) \qquad (5.9)$$

The quantities which can be easily varied in a given experimental system are the acoustical pressure and the angle of incidence of the radiation on the sound field, while the radiation and sound wavelengths as well as the width of the sound field usually remain fixed. Therefore, two dimensionless parameters are chosen which depend only upon the angle of incidence and the acoustic pressure, $\alpha$ and $\nu$, respectively.A third parameter (Q) is needed to complete the description of the problem. These parameters are

$$\nu = \frac{k\zeta' L}{\cos\Theta} \qquad \text{(Raman-Nath parameter)}$$

$$\simeq k\zeta' L \qquad \text{since } \cos\Theta \simeq 1 \;, \tag{5.10}$$

$$\alpha = \frac{\zeta_o k}{\kappa} \sin\Theta \;, \tag{5.11}$$

and

$$Q = \frac{\kappa^2 L}{\zeta_o k \cos\Theta}$$

$$\simeq \frac{\kappa^2 L}{\zeta_o k} \qquad \text{since } \cos\Theta \simeq 1 \;. \tag{5.12}$$

Substituting these parameters into equation (5.9) we obtain

$$\frac{d\Phi_n(x)}{dx} + \frac{\nu}{2L}\left[\Phi_{n-1}(x) - \Phi_{n+1}(x)\right] = j\,\frac{nQ}{2L}(n-2\alpha)\Phi_n(x) \tag{5.13}$$

where the partial differentials have been replaced by total differentials. In a manner analogous to x-ray diffraction the Bragg angle for acousto-optic diffraction is given by

$$\sin\Theta_B = \frac{\lambda_o}{2\zeta_o\Lambda} \tag{5.14}$$

where $\Theta_B$ = Bragg angle in the modulating medium,

$\lambda_o$ = vacuum wavelength of electromagnetic radiation,

and $\Lambda$ = acoustic wavelength.

Therefore, at $\Theta = -\Theta_B$, $\alpha = +\frac{1}{2}$.

If the plane waves of equation (5.4) are considered the normal modes, then $\nu$ may be thought of as the coupling coefficient between 'adjacent' modes [5.2]. Since a purely sinusoidal sound field has been assumed, only adjacent modes are coupled. On the other hand, if the sound wave is not sinusoidal the refractive index can be expressed as a Fourier series. In this case, the amplitude of the refractive index change for each harmonic, $\zeta_j'$, will yield a corresponding $\nu_j$. Therefore, modes which are not adjacent will be coupled. For instance, $\nu_2 \neq 0$, corresponding to the second harmonic will allow energy transfer between every other mode. Consequently, by analysing the intensity distribution of the diffracted radiation the waveform of the acoustic beam (the $\zeta_j$'s) in the diffracting medium can be determined (optical probing).

The amount of energy transfer between modes depends not only upon $\nu$ but also upon the degree of synchronization of the modes. Since the various diffraction orders have different propagation directions, two orders which are in phase at a given plane in space will not maintain this phase relationship except at special incidence angles. The parameter Q is a measure of the differences in spatial phase of the various partial waves due to their different directions of propagation.

Consider the E-M wave travelling through the sound field at an angle $\beta_n$ with respect to the $n = 0$ wave (see Fig. 5.1). Its path length will be

$$\text{P.L.} = \frac{\zeta_o L}{\cos\beta_n} = \zeta_o L[1 + \tan^2\beta_n]^{1/2} \tag{5.15}$$

But $$\tan\beta_n \approx \frac{n\kappa}{\zeta_o k} \tag{5.16}$$

Therefore $$\text{P.L.} \simeq \zeta_o L \left[1 + \frac{1}{2}\left(\frac{n\kappa}{\zeta_o k}\right)^2\right] \qquad (5.17)$$

and the difference in spatial phase $\Delta\delta_n$ for a wave travelling in the $\beta_n$ direction and a wave travelling at the incidence angle is

$$\Delta\delta_n = k\Delta\text{P.L.} \simeq \frac{n^2 Q}{2} \qquad (5.18)$$

Consequently for larger values of Q there is less synchronization and there will be little energy transfer except when $\alpha = \frac{1}{2}$. In this case, from equation (5.13) it can be seen that the right hand side is zero just as it is for the incident (n=0) beam indicating that the two waves, n = 0 and n = 1, are synchronized. Note that n = -1 is not synchronized and will therefore not grow in amplitude.

### 5.2.2 Derivation of Diffracted Intensity

For n = 1, $\alpha \cong \frac{1}{2}$ and recalling that $\Phi_{-1}(x) = 0$, one obtains from equation (5.13)

$$\frac{d\Phi_o(x)}{dx} - \frac{\nu}{2L}\Phi_1(x) = 0 \qquad (5.19)$$

and $$\frac{d\Phi_1(x)}{dx} + \frac{\nu}{2L}\Phi_o(x) = j\frac{Q}{2L}(1-2\alpha)\Phi_1(x) \quad . \qquad (5.20)$$

In their decoupled form equations (5.19) and (5.20) become

$$\frac{d^2\Phi_o(x)}{dx^2} - \frac{j[Q(1-2\alpha)]}{2L}\frac{d\Phi_o(x)}{dx} + \left(\frac{\nu}{2L}\right)^2\Phi_o(x) = 0 \qquad (5.21)$$

and $$\frac{d^2\Phi_1(x)}{dx^2} - j\frac{[Q(1-2\alpha)]}{2L}\frac{d\Phi_1(x)}{dx} + \left(\frac{\nu}{2L}\right)^2\Phi_1(x) = 0 \tag{5.22}$$

with the boundary conditions

$$\Phi_o(o) = 1 \tag{5.23}$$

and $$\Phi_1(o) = 0 \tag{5.24}$$

The solutions to these second order, homogeneous differential equations with constant coefficients, subject to the above boundary conditions are

$$\Phi_o(x) = \exp\left[\frac{jQ(1-2\alpha)}{4L}x\right]\left[\cos\left(\frac{\sigma}{L}x\right) + \frac{jQ(1-2\alpha)}{4\sigma}\sin\left(\frac{\sigma}{L}x\right)\right] \tag{5.25}$$

and $$\Phi_1(x) = -\frac{\nu}{2\sigma}\exp\left[\frac{jQ(1-2\alpha)}{4L}x\right]\sin\left(\frac{\sigma}{L}x\right) \tag{5.26}$$

where $$\sigma = \frac{1}{4}\{[Q(1-2\alpha)]^2 + [2\nu]^2\}^{1/2} \tag{5.27}$$

Therefore, the respective intensities $I_o$ and $I_1$, at $x = L$ will be

$$I_o = \Phi_o\Phi_o^* = 1 - I_1 \tag{5.28}$$

and $$I_1 = \Phi_1\Phi_1^* = \left(\frac{\nu}{2}\right)^2\left[\frac{\sin\sigma}{\sigma}\right]^2 \tag{5.29a}$$

$$\cong \left(\frac{\nu}{2}\right)^2 \quad \nu << 1,\ \alpha = .5. \tag{5.29b}$$

[With respect to equation (5.27) it should be mentioned that it is correct, as opposed to that given in Klein's paper].

Equation (5.29a) gives the intensity of the n = 1 order as a function of angle ($\alpha$). The sharpness of the distribution will depend upon Q and the magnitude upon the Raman-Nath parameter. The validity of the above theory will be demonstrated in Section 5.3.2.

### 5.2.3 The Raman-Nath Parameter for a Single Crystal Solid

The change produced in the dielectric impermeability in a solid is related to the strain by

$$\Delta B_{ij} = p_{ijk\ell}s_{k\ell} \tag{5.30}$$

where $B_{ij}$ = dielectric impermeability tensor component,

$p_{ijk\ell}$ = elasto-optic coefficient in tensor notation,

and $s_{k\ell}$ = the applied strain in tensor notation [5.3].

The dielectric impermeability tensor components are related to the dielectric tensor components ($K_{ij}$) by

$$K_{ij}B_{jk} = \delta_{ik} \tag{5.31}$$

where $\delta_{ik}$ = Kronecker delta.

In the case of cubic crystals $K_{ij} = K$. Thus,

$$\Delta K_{ij} = -K^2\Delta B_{ij} = -K^2 p_{ijk\ell}s_{k\ell}. \tag{5.32}$$

Now, since $K = \zeta_o^{\,2}$ (5.33)

and therefore $\Delta K = 2\zeta_o \Delta\zeta$ , (5.34)

the change in refractive index due to a strain is given by

$$\zeta' = \Delta\zeta_{ij} = -\frac{\zeta_o^3}{2} p_{ijk\ell} s_{k\ell} . \tag{5.35}$$

In order to determine the change in refractive index due to a compressional wave propagating in the <111> direction the applicable tensor components must be determined in terms of those relative to the crystal axis. This is done by using the general tensor transformation law

$$T'_{ijk\ell} = a^T_{im} a^T_{jn} a^T_{ko} a^T_{\ell p} T_{mnop} \tag{5.36}$$

where

$$A^T = \begin{bmatrix} \frac{1}{\sqrt{2}} & \frac{-1}{\sqrt{2}} & 0 \\ \frac{1}{\sqrt{6}} & \frac{+1}{\sqrt{6}} & \frac{-2}{\sqrt{6}} \\ \frac{1}{\sqrt{3}} & \frac{1}{\sqrt{3}} & \frac{1}{\sqrt{3}} \end{bmatrix} \tag{5.37}$$

for the z' axis in the <111> direction, the x' axis in the <1$\bar{1}$0> direction and the y' axis in the <11$\bar{2}$> direction,

with $T_{mnop}$ = fourth rank tensor component relative to the principle axis of the crystal

and $T'_{ijkl}$ = fourth rank tensor component relative to the new,rotated axis.[5.6].

Thus $p'_{33} = \frac{1}{3} p_{11} + \frac{2}{3} p_{12} + \frac{4}{3} p_{44}$ (5.38) where $p'_{33}$ = elasto-optic tensor component written in reduced notation and is applicable for the radiation wave polarization being parallel to the <111> direction. It has been shown that the elasto-optic constants in germanium have the same sign [5.4]. This is the reason for polarizing the radiation parallel to the <111> axis. If it were polarized in the <1$\bar{1}$0> direction the relative photoelastic constant would be

$$p'_{13} = \frac{1}{3} p_{11} + \frac{2}{3} p_{12} - \frac{2}{3} p_{44} . \tag{5.39}$$

The value of $p_{44}$ turns out to be approximately half of $p_{11}$ or $p_{12}$, therefore $p'_{13}$ for an E-M wave polarized in the <1$\bar{1}$0> direction and a <111> directed acoustic wave will be ∿ 2.5 times smaller than $p'_{33}$.

The acoustic power is related to the strain in the following manner [5.5]. From Chapter IV, the average acoustic power delivered to the crystal is

$$P_{del} = \frac{1}{2} \dot{u}_d^2 \rho_d v_d^d S \tag{5.40}$$

$$\text{but} \qquad s_{33} = \frac{\dot{u}_d}{v_d^d} \tag{5.41}$$

$$\text{therefore} \quad \frac{P_{del}}{S} = \frac{1}{2} \rho_d (v_d^d)^3 s_{33} \tag{5.42}$$

$$\text{where} \quad \frac{P_{del}}{S} = \text{acoustic power density} .$$

The acoustic power density is related to the incident R.F. power ($P_{RF}$) on the transducer impedance matching network by an effective transduction efficiency T. From equation (5.10) and using (5.35) and (5.42) we obtain

$$\nu = \frac{2\pi L}{\lambda_o}\left[-\frac{\zeta_o^3}{2}\, p_{eff}\left(\frac{2P_{RF}T \times 10^7}{\rho_d (v_d^d)^3 S}\right)^{1/2}\right] \qquad (5.43)$$

and therefore $\frac{\nu^2}{4} = \frac{\pi^2}{2\lambda_o^2}\Psi[(\frac{L}{H})P_{RF}T \times 10^7]$ (5.44)

where $\Psi = \frac{\zeta_o^6 p_{eff}^2}{\rho (v_d^d)^3}$ (5.45)

and $S = L x H$ . (5.46)

The factor $10^7$ is the conversion factor relating watts and ergs. $\Psi$ is the photoelastic figure of merit for the modulating medium, in this case germanium.

## 5.3 Acousto-Optic Experimental Results

Fig. 5.2 shows the experimental arrangement used; first to evaluate the effective photoelastic constant of germanium hence determine $\nu$ and second, to compare the variation of the diffracted intensity with the angle of incidence, that is, to determine Q.

### 5.3.1 Determination of Photoelastic Constant of Germanium ($p'_{33}$)

The 5 watt, 10.6µ laser beam was incident from the left and polarized parallel to the <111> directed dilatational acoustic wave. To evaluate the figure of merit of germanium the chopped, transmitted optical beam power was continuously monitored and the diffracted beam was collected by a NaCl lens and detected with a Au:Ge (77°K) detector.

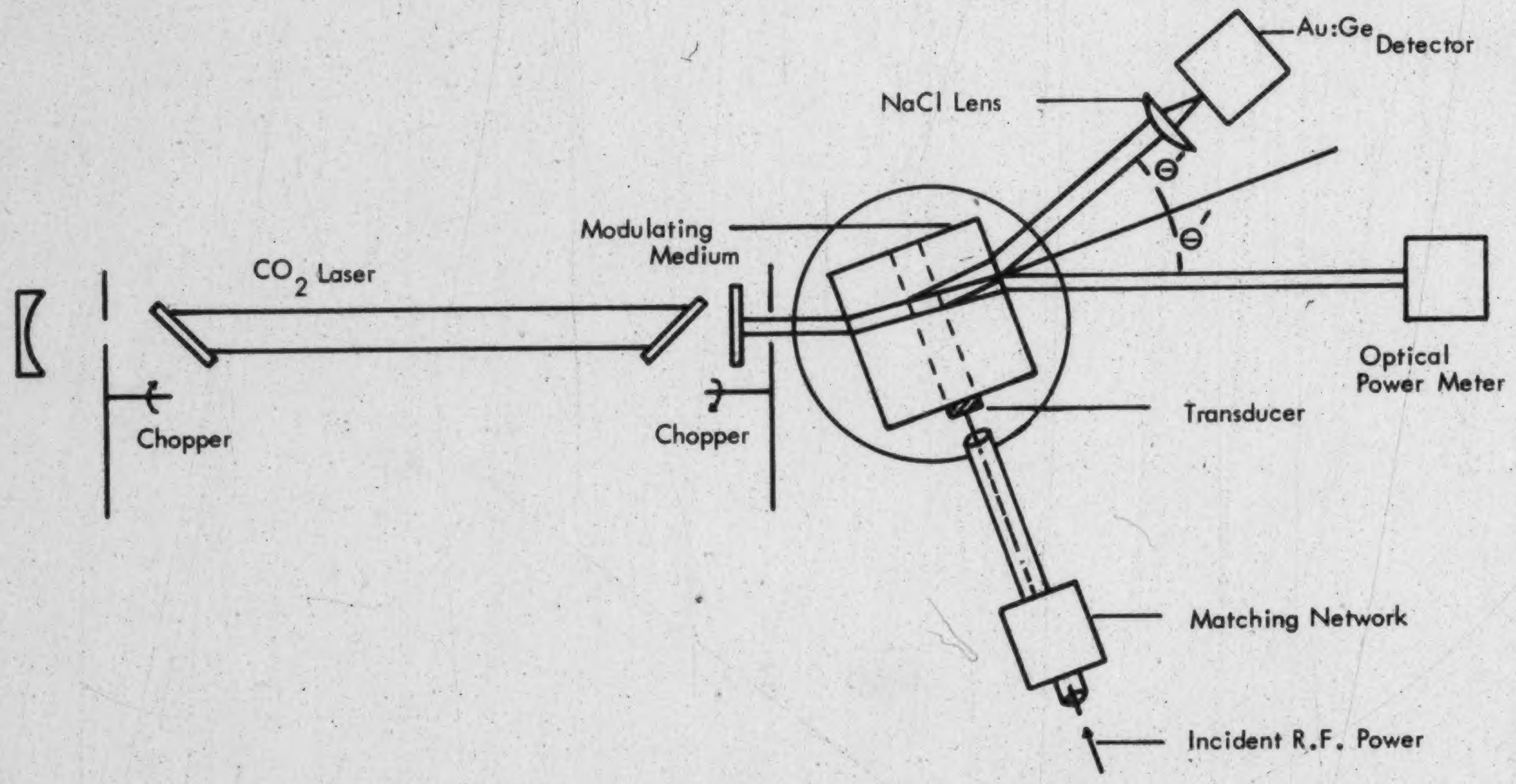

Fig. 5.2 Schematic Diagram of Experimental Apparatus.

The detector responsivity was 1.85 v/watt as determined by attenuating with calibrated $\mathrm{CaF_2}$ attenuators, an incident 10.6μ beam of known power. For a transducer having an L = 4.25 mm and an H = 5.5 mm, the corrected one-way tuned insertion loss at 354 MHz was 11.5 db. The material acoustic losses (see Fig. 4.11) amounted to an additional 2.95 db/cm or 3.68 db loss to the center of the 1 inch germanium cube resulting in an effective transduction efficiency of T = 15.18 db. Using the circuit shown in Fig. 5.3 three watts of R.F. power was delivered to the matching network. At the Bragg angle, 12.33 mw or .25% of the incident radiation was diffracted. From equations (5.29b) and (5.44) this results in a $\nu = .1$ and an $\Psi = 8.08\mathrm{x}10^{-16}$ for germanium ($\zeta_0 = 4.0$). From this figure of merit an effective photoelastic constant of $p_{eff} = .42$ is obtained. Considering the experimental arrangement this result is surprising since it is, essentially, exactly the same as that determined by Pinnow who employed an experimental technique much more suited for determining photoelastic constants [5.4].

### 5.3.2 Angular Dependence of Diffracted Intensity

By rotating the table on which the germanium cube was located the angular location and relative amplitudes of the diffracted intensity maxima were determined. The signals obtained at $\Theta$ = 20°, 18.75° and 21.25° are shown in Fig. 5.4. In this instance the chopper was located intracavity hence the 'Q'-switched leading edge of the infrared pulse. The acoustic beam was also pulsed.

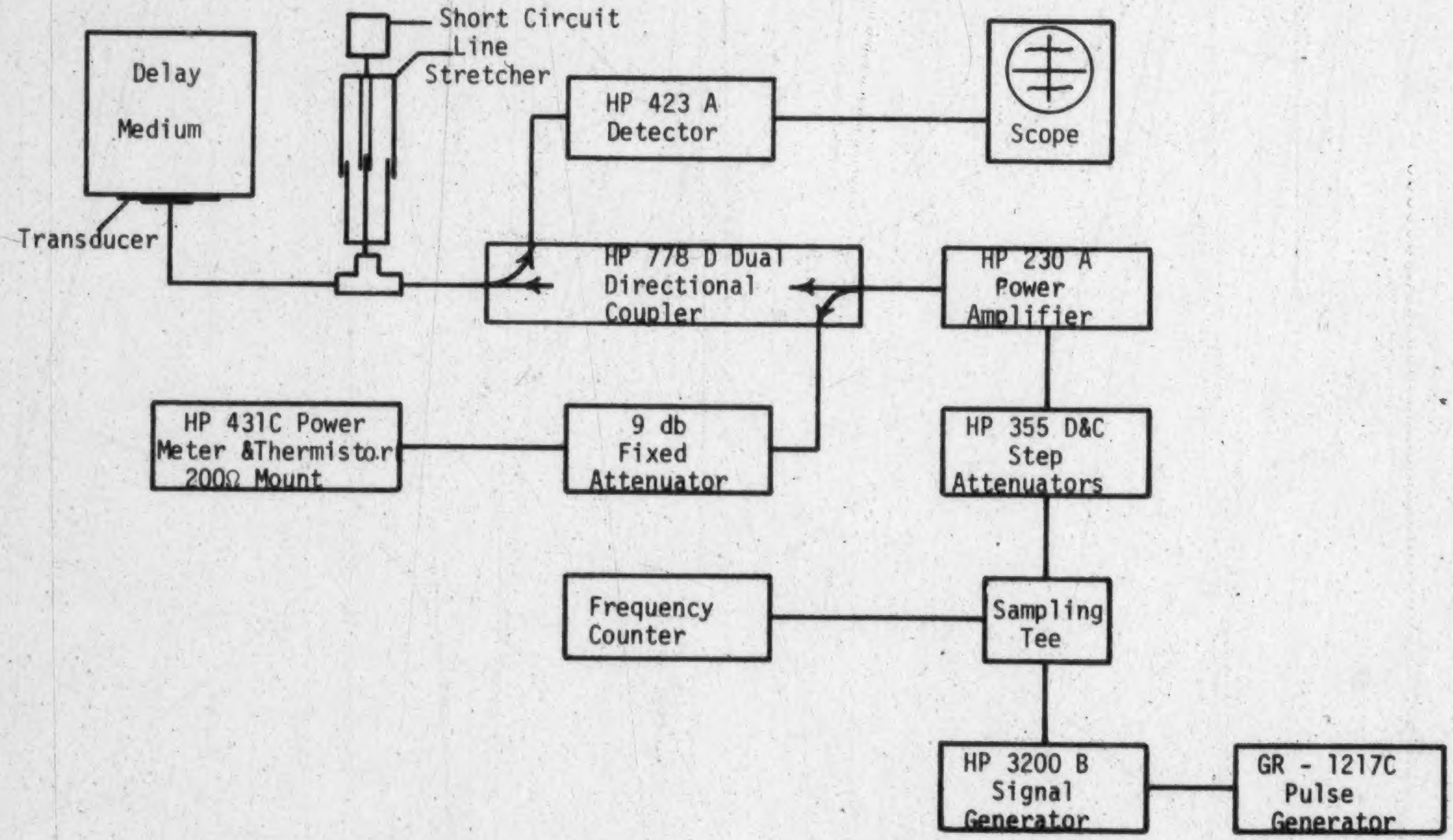

Fig. 5.3 Circuit for Controlling and Monitoring Transducer Input Power (Power Meter) and Reflected Power (Scope).

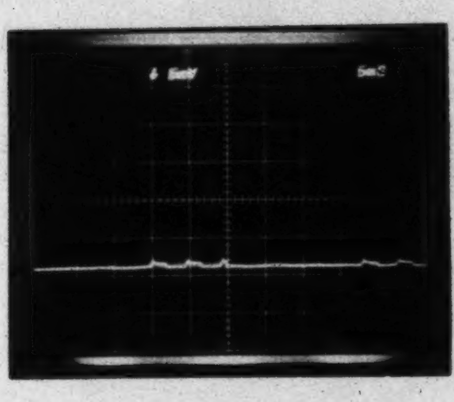

Fig. 5.4a $\Theta' = 18.75°$

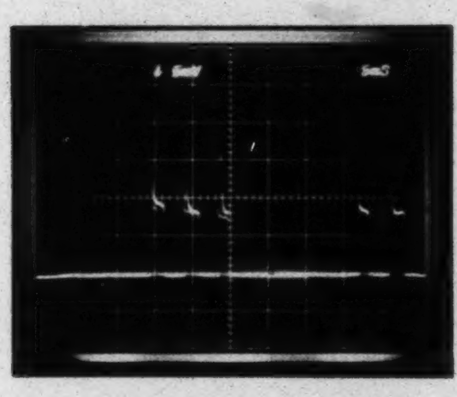

Fig. 5.4b $\Theta' = 20°$

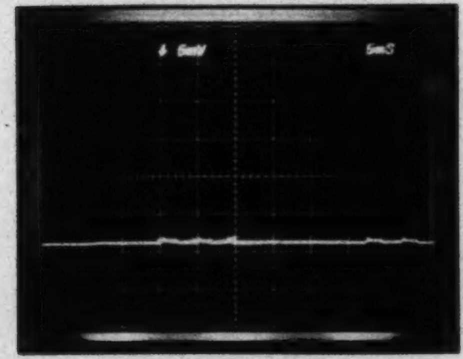

Fig. 5.4c $\Theta = 21.25°$

Fig. 5.4 Diffracted 10.6μ Laser Pulses at the Angular Locations of Maximum Intensity.

The above data was plotted on a computer generated curve based on equations (5.27) and (5.29) for $\nu = .1$ and $Q = 291$. As can be seen in Fig. 5.5, the agreement is excellent. The angle ($\theta'$) represented in Fig. 5.5 is the experimental angle between the normal to the cube and the incident beam; that is, the angle external to the medium and not the internal angle usually reported.

## 5.4 Conclusion

The unified theory of Klein and Cook presented in Section 5.1 which is based on the dimensionless parameters $\nu$, $\alpha$, and Q was shown experimentally to adequately describe the ultrasonic ($\Omega > 100$ MHz) diffraction of 10.6μ radiation. The acousto-optic, material figure of merit for a single crystal was derived. This figure of merit was determined experimentally for germanium and shown to be ∿ 540 times that of fused quartz, indicative of an effective photoelastic constant of .42 for a 10.6μ radiation wave polarized parallel to a <111> directed compressional acoustic beam [5.4].

Based on the results presented in this chapter, one can realistically expect to achieve a 12.5% diffraction efficiency with only 50 watts R.F. and an aspect ratio ($\frac{L}{H}$) of 3. If a T = 15 db is to be maintained, however, this will require: an improved R.F. matching network due to the increased transducer area; a reduction in contact resistance and transducer electrode $I^2R$ loss; cooling and; precise, stable angular alignment due to the concomitant increase in Q. It should be noted that the overall area requirements can still be kept reasonable by the use of cylindrical lenses resulting in a reduction in the required transducer height.

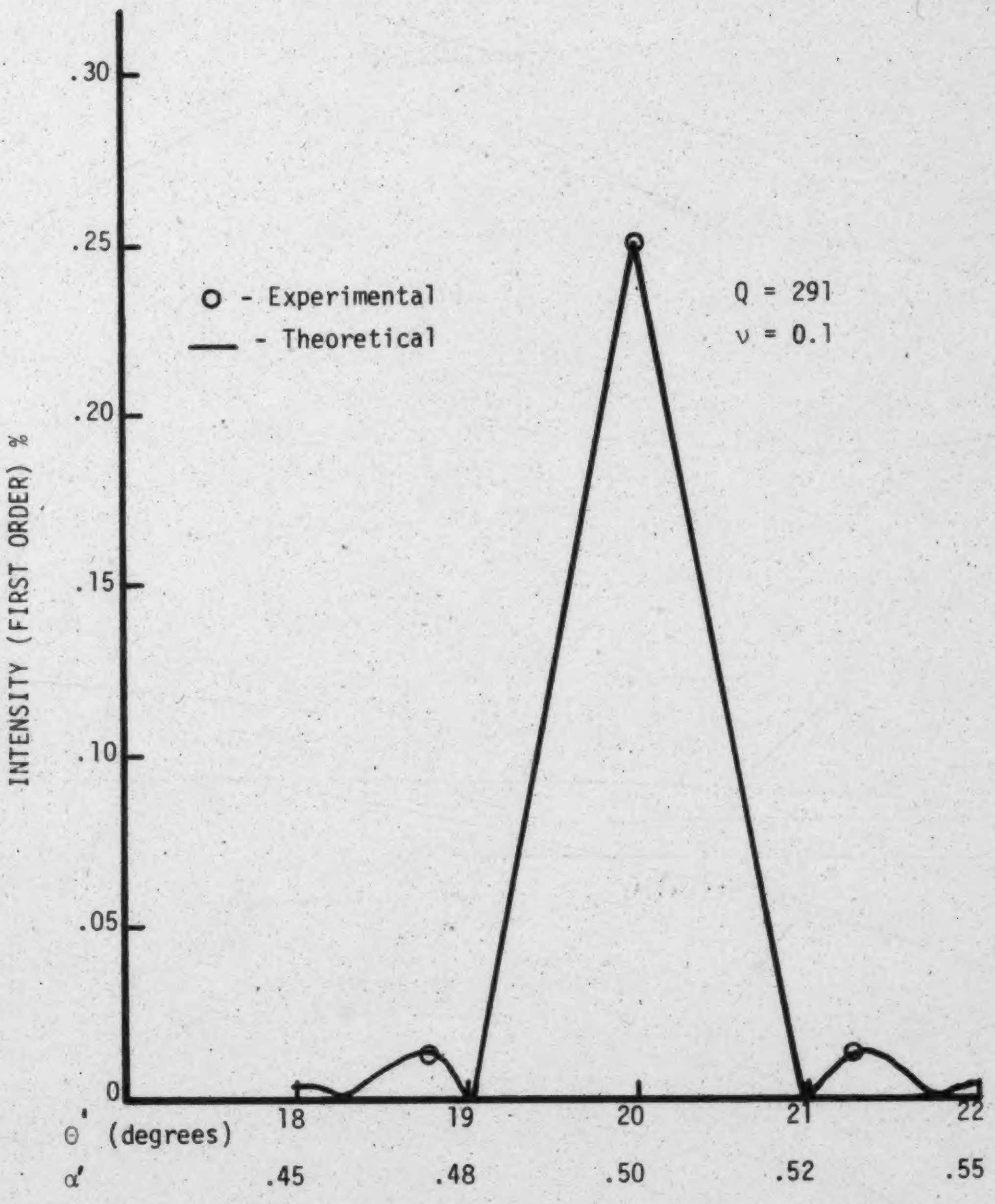

Fig. 5.5 First Order Light Intensity versus Angle of Incidence (Θ' external) with ν = .1 and Q = 291.

Use of such an acousto-optic modulator (a single crystal of germanium utilizing a thin film ZnO transducer) intracavity, would be capable of coupling out 25% of the cavity energy. Thus it would appear that the use of an acousto-optic modulator, operated intracavity, to efficiently output couple a $CO_2$ laser is indeed feasible.

# CHAPTER VI

# CONCLUSION

The feasibility of simultaneously frequency modulating and optimally coupling radiation out of a $CO_2$ laser cavity by means of an acousto-optic modulator has been demonstrated experimentally and theoretically. In addition to the development of a modulation system capable of detecting Doppler shifts of 1 GHz described in this thesis, other aspects of the system were also investigated. A method of controlling and stabilizing a passively Q-switched $CO_2$ laser (see Appendix II) was developed. A 1 meter coaxial $CO_2$ laser with the uncooled germanium cube intracavity was made to oscillate. Also, coherent detection was attempted, however, it was, as expected, unsuccessful due to the very limited frequency response of the Au:Ge detector. These results, in our opinion, renders the IRDAR system proposed in Chapter I worthy of further consideration. This is due not only to the developments reported above but also to the state of the art development in $CO_2$ laser technology.

There would, of course, be many challenging engineering problems to be overcome in building a working system. Some of these problems would be to test the modulator intracavity to determine, the cooling, beam focusing and power, both acoustic and electromagnetic, requirements; to construct (purchase) and test an ultra-fast photodetector; to measure the magnitude of the frequency pulling between the two cavities and correct this if possible; and to construct a suitable optical delay line for testing the system. Also, after a working system had been constructed and tested under controlled conditions the signal degredation due to transmission through the non-ideal, real atmosphere would have to be investigated. If a Doppler compensating communication system were to be designed having a 50% bandwidth with a center frequency of $\sim$ 400 MHz using an ultrasonic frequency translator, piezoelectrically active single crystal plates would have to be seriously considered and care taken in choosing the electrode materials and thicknesses. As mentioned, for large area transducers this would indeed be challenging.

Due to the broad scope of the investigation described in this thesis, a thorough study of all aspects of the project was difficult for one man to accomplish, even in a three year period. Therefore, there are many aspects which warrant further investigation. To begin with, an improved deposition system could be constructed and many purely thin film experiments conducted. These would include investigating the ZnO thin film growth mechanisms paying particular attention to the effect of the nucleating surface and reactive gas content in the sputtering gas mix on the film structure and composition. Acoustically, the maximum gain-bandwidth product for the ZnO thin film transducers as well as their power handling capabilities should be determined experimentally. In addition, consideration could be given to acoustic beam steering techniques. Acousto-optically, the maximum number of resolvable spots for the modulator should be determined. Also, when higher acoustic powers are employed, optical probing experiments to determine the shape of the acoustic wave could be conducted.

# REFERENCES

## CHAPTER I

1.1 N. Uchida, N. Nüzeki, Acousto-Optic Deflection Materials and Techniques", Proceedings IEEE 61, pp. 1073-1092, 1973.

1.2 A Korpel et al., "A Television Display Using Acoustic Deflection and Modulation of Coherent Light", Proceedings IEEE 54, pp. 1429-1437, 1966.

1.3 S.E. Harris, R.W. Wallace, "Acousto-Optic Tunable Filter", Journal Optical Society of America 59, pp. 744-747, 1969.

1.4 A.J. DeMaria, "Review of CW High-Power CO$_2$ Lasers", Proceedings IEEE 61, pp. 731-748, 1973.

1.5 M.E. Pedinoff, "Technical Memorandum on Applications of Intracavity Ultrasonic Frequency Translators at 10.6μ".

1.6 M. Ross, "Laser Receivers-Devices, Techniques, Systems", Wiley, 1966, Chapter 10, pp. 340-368.

1.7 J.F. Reintjes, G.T. Coate (eds.), "Principles of Radar", McGraw-Hill, 1952, Chapter 1, pp. 23-32.

1.8 D.K. Barton, "Radar Systems Analysis", Prentice-Hall, 1965, Chapter 2, p. 57.

1.9 Ibid., p. 248.

1.10 A.E. Seigman et al., "Frequency Translation of Lasers Output Frequency by Acoustic Output Coupling", Applied Physics Letters 5, p. 1, 1964.

1.11 Loc. cit. [1.6], Chapter 4, pp. 118-119.

1.12 R.L. Abrams, D.A. Pinnow, "Acousto-Optic Properties of Crystalline Germanium", Journal Applied Physics 41, pp. 2765-2768, 1970.

CHAPTER II

2.1 A.H. Meitzler, "Piezoelectric Transducer Materials and Techniques for Ultrasonic Devices Operating Above 100 MHz", Ultrasonic Transducer Materials, (ed.) O.E. Mattiat, Plenum Press, 1971, Chapter 3, pp. 133-139.

2.2 Ibid., pp. 158-163.

2.3 W.A. Warner, A.H. Meitzler, "Performance of Bonded, Single Crystal $LiNbO_3$ and $LiGaO_2$ as Ultrasonic Transducers Operating Above 100 MHz", Proceedings IEEE 56, pp. 1376-1377, 1968.

2.4 E.K. Sittig, H.D. Cook, "A Method for Preparing and Bonding Ultrasonic Transducers Used in High Frequency Digital Delay Lines", Proceedings IEEE 56, pp. 1375-1376, 1968.

2.5 Loc. cit., [2.1], p. 162.

2.6 R.M. Malbon et al., "Zinc Oxide Film Microwave Acoustic Transducers", Applied Physics Letters 10, pp. 9-10, 1967.

2.7 L. Holland, "Cathodic Sputtering for Thin Film Deposition and Surface Etching", Edwards High Vacuum, 430 South Service Road, West Oakville, Ontario, Canada, 1969.

2.8 L.B. Loeb, "Basic Processes in Gaseous Electronics", University of California Press, Berkeley, 1955, pp. 329, 620-628.

2.9 F. Reif, "Fundamentals of Statistical and Thermal Physics", McGraw-Hill, 1965, pp. 262-273.

2.10 Ibid., pp. 467-471.

2.11 C.M. Van Atta, "Vacuum Science and Engineering", McGraw-Hill, 1965, pp. 13-14.

2.12 L.I. Maissel, "Applications of Sputtering to the Deposition of Films", Chapter 4, Handbook of Thin Film Technology, (eds.) L.I. Maissel, R. Glang, McGraw-Hill, 1970, pp. 4-20.

2.13 H.F. Winters et al., "Adsorption of Gases Activated by Electronic Impact", Journal of Chemical Physics 41, p. 2766, 1964.

2.14 H.F. Winters, E. Kay, "Gas Incorporation into Sputtered Films", Journal Applied Physics 38, p. 3928, 1967.

2.15 C.F. Brockelsby et al., "Ultrasonic Delay Lines", Iliffe Books Ltd., London, 1963.

2.16 A.W. Warner, "New Piezoelectric Materials", Proceedings of the 19th Annual Symposium on Frequency Control, pp. 5-21, 1965.

2.17 M. Onoe et al., "Elastic and Piezoelectric Characteristics of Bismuth Germanium Oxide $Bi_{12}GeO_{20}$", IEEE Transactions on Sonics and Ultrasonics 14, pp. 165-167, 1967.

2.18 A.W. Warner et al., "Piezoelectric and Photoelastic Properties of Lithium Iodate", Journal Acoustical Society of America 47, pp. 791-794, 1970.

2.19 N.F. Foster et al., "Cadmium Sulfide and Zinc Oxide Thin-Film Transducers", IEEE Transactions on Sonics and Ultrasonics 15, pp. 28-41, 1968.

2.20 J. de Klerk, "Thin-Film Piezoelectric Transducers Used as Generators and Detectors of Microwave Phonons with Some Attenuation Measurements in $SiO_2$", Journal Applied Physics 37, pp. 4522-4528, 1966.

2.21 M. Onoe et al., "Shift in Location of Resonant Frequencies Caused by Large Electromechanical Coupling in Thickness-Mode Resonators", Journal Acoustical Society of America 35, pp. 36-42, 1967.

2.22 D.A. Berlincourt et al., "Piezoelectric and Piezomagnetic Materials and Their Function in Transducers", Physical Acoustics (ed.) W.P. Mason, Academic Press, 1964, Volume 1, Part A, Chapter 3, pp. 198-219.

2.23 L. Egerton, "Piezoelectric and Dielectric Properties of Ceramics in the System Potassium-Sodium Niobate", Journal American Ceramic Society 42, pp. 438-442, 1959.

2.24 A.W. Warner et al., "Determination of Elastic and Piezoelastic Constants for Crystals in Class [3m]", Journal Acoustical Society of America 42, pp. 1223-1231, 1967.

2.25 A.W. Warner et al., "Elastic and Piezoelectric Constants of $Ba_2NaNb_5O_{15}$", Journal Applied Physics 40, pp. 4353-4356, 1969.

## CHAPTER III

3.1 G.A. Rozgonyi, W.J. Polito, "Epitaxial Thin Films of ZnO on CdS and Sapphire", Journal of Vacuum Science and Technology 6, pp. 115-119, 1969.

3.2 K.L. Chopra, "Thin Film Phenomena", McGraw-Hill, 1969, Chapter 3, pp. 83, 97.

3.3 N.F. Foster, "Crystallographic Orientation of Zinc Oxide Films Deposited by Triode Sputtering", Journal of Vacuum Science and Technology 6, pp. 111-114, 1969.

3.4 D.L. Denburg, "Wide-Bandwidth High-Coupling Sputtered ZnO Transducers on Sapphire", IEEE Transactions on Sonics and Ultrasonics 18, pp. 31-35, 1971.

3.5 J.D. Larson et al., "R.F. Diode Sputtered ZnO Transducers", IEEE Transactions on Sonics and Ultrasonics 19, pp. 18-22, 1972.

3.6 A.H. Fahmy, E.L. Adler, "Structure and Properties of R.F. Sputtered ZnO Transducers", IEEE Transactions on Sonics and Ultrasonics 19, pp. 346-349, 1972.

3.7 J.F. Nye, "Physical Properties of Crystals", Oxford at the Clarendon Press, 1967, Chapter 14, p. 262.

3.8 D.L. Raimondi, E. Kay, "High Resistivity Transparent ZnO Thin Films", Journal of Vacuum Science and Technology 7, pp. 96-99, 1970.

3.9 C. Kittel, "Introduction to Solid State Physics", John Wiley & Son, 1966, Chapter 10, p. 302.

3.10 D.G. Thomas, "Infrared Absorption in Zinc Oxide Crystals", Journal of Physics and Chemistry of Solids 10, pp. 47-51, 1959.

3.11 R.J. Collins, D.A. Kleinman, "Infrared Reflectivity of Zinc Oxide", Journal of Physics and Chemistry of Solids 11, pp. 190-194, 1959.

3.12 V.N. Filimonov, "Change in the Infrared Absorption of Certain Semiconducting Absorbents Under Ultraviolet Illumination", Optics and Spectroscopy 6, pp. 139-140, 1959.

3.13 K.D. Möller, W.G. Rothschild, "Far-Infrared Spectroscopy", John Wiley & Son, 1971, Chapter 12, pp. 451-452.

3.14 E. Bauer, "Growth of Oriented Films on Amorphous Surfaces" in "Single Crystal Films, Francombe and Sato (eds.), MacMillan, 1964, pp. 43-67.

3.15 Loc. cit., [3.2], Chapter 4, p. 226.

3.16 Loc. cit., [3.2], Chapter 5, pp. 287-295.

3.17 Ibid., p. 291.

## CHAPTER IV

4.1 H.A. Heynau, "The State of the Art in Beam Steering and Control using Acousto-Optics", Acoustic Surface Wave and Acousto-Optic Devices, (ed.) T. Kallard, Optosonic Press, 1971, pp. 127-138.

4.2 J.D. Larson et al., "R.F. Diode Sputtered ZnO Transducers", IEEE Transactions on Sonics and Ultrasonics 19, pp. 18-22, 1972.

4.3 J.D. Larson et al., "Effect of Top Electrode Thickness on the Performance of Microwave Acoustic Transducers", IEEE Transactions on Microwave Theory and Techniques 18, pp. 602-608, 1970.

4.4 W.P. Mason, "Crystal Physics of Interaction Processes", Academic Press, 1966, Section 6.3, pp. 136-146.

4.5 E.K. Sittig, "Effects of Bonding and Electrode Layers on the Transmission Parameters of Piezoelectric Transducers Used in Ultrasonic Delay Lines", IEEE Transactions on Sonics and Ultrasonics 16, pp. 2-10, 1969.

4.6 K. Ogata, "State Space Analysis of Control Systems", Prentice-Hall, 1967, Chapter 2, pp. 49-52.

4.7 T.M. Reeder, D.K. Winslow, "Characteristics of Microwave Acoustic Transducers for Volume Wave Excitation", IEEE Transactions on Microwave Theory and Techniques 17, pp. 927-941, 1969.

4.8 H. Seki et al., "Diffraction Effects in the Ultrasonic Field of a Piston Source and Their Importance in the Accurate Measurement of Attenuation", Journal Acoustical Society of America 28, pp. 230-238, 1956.

4.9 E.P. Papadakis, "Diffraction of Ultrasound Radiating into an Elastically Anisotropic Medium", Journal Acoustical Society of America 36, pp. 414-422, 1964.

4.10 W.P. Mason, T.B. Bateman, "Ultrasonic-Wave Propagation in Pure Silicon and Germanium", Journal Acoustical Society of America 36, pp. 644-652, 1964.

4.11 C. Kittel, "Introduction to Solid State Physics", Wiley, 1966, Chapter 6, p. 182.

4.12 B.I. Miller, "Temperature Dependence of the Ultrasonic Attenuation in Germanium", Physical Review 132, pp. 2477-2483, 1963.

4.13 E. Dobbs, "Attenuation of Sound in a Germanium Crystal at Ultra-High Frequencies and Low Temperatures", Physical Review Letters 3, pp. 332-334, 1959.

4.14 Loc. cit., [4.4], p. 133.

4.15 R. Truell, "Ultrasonic Methods in Solid State Physics", Academic Press, 1969, p. 370.

4.16 R.W. Dixon, "Photoelastic Properties of Selected Materials and Their Relevance for Applications to Acoustic Light Modulators and Scanners", Journal Applied Physics 38, pp. 5149-5153, 1967.

4.17 H. Jaffe, D. Berlincourt, "Piezoelectric Transducer Materials", Proceedings IEEE 53, pp. 1372-1386, 1965.

4.18 G. Simmons, H. Wang, "Single Crystal Elastic Constants and Calculated Aggragate Properties, A Handbook", M.I.T. Press, 1971, pp. 176-177 (an average value was taken).

4.19 A.H. Fahmy, E.L. Adler, "Multilayer Microwave Acoustic Transducers", Journal Acoustical Society of America 50, pp. 415-420, 1971.

## CHAPTER V

5.1 W.R. Klein et al., "Light Diffraction by Ultrasonic Gratings", Acoustics 15, pp. 67-74, 1965.

5.2 W.R. Klein, B.D. Cook, "Unified Approach to Ultrasonic Light Diffraction", IEEE Transactions on Sonics and Ultrasonics 14, pp. 123-134, 1967.

5.3 J.F. Nye, "Physical Properties of Crystals", Clarendon Press, 1967, Chapter 6, pp. 93-109, and Chapter 13, p. 249.

5.4 R.L. Abrams, D.A. Pinnow, "Acousto-Optic Properties of Crystalline Germanium", Journal Applied Physics 41, pp. 2765-2768, 1970.

5.5 M.E. Pedinoff, "Technical Memorandum on Applications of Intracavity Ultrasonic Frequency Translators at 10.6μ Microns Wavelength".

5.6 Loc. cit., [5.3], Chapter 1, pp. 3-15.

5.7 Loc. cit., [5.3], Chapter 13, p. 251.

# APPENDIX 1

```
    ∇ TRANS3;F;G1;G2;G3;G4;G5;X;Y;Z;ZB;CD;A;B;C;D;Z11;Z12;
      Z21;Z22;V;G;H;I;J;K;L;M;P;Q;R;S;T;U;O;W;II;CF

[1]   V←D1,V1,T1,D2,V2,T2,D3,V3,T3,AREA,RP33,C33,KT,D4,V4,
      T4,D5,V5,T5,EPZNS
[2]   ZO1←V[2]×V[1]×V[10]
[3]   ZO2←V[4]×V[5]×V[10]
[4]   ZO3←V[7]×V[8]×V[10]
[5]   ZO4←V[14]×V[15]×V[10]
[6]   ZO5←V[17]×V[18]×V[10]
[7]   CO←V[10]×V[11]÷V[9]
[8]   FO←V[8]÷2×V[9]
[9]   ZO←1÷○2×FO×CO
[10]  COZNS←V[20]×V[10]÷V[6]
[11]  INTV←RETV←⍳0
[12]  II←0
[13]  CF←V[13]+0.02×II
[14]  N←CO×CF×(V[12]÷V[11])*0.5
[15]  FR←ZOB←⍳0
[16]  F←50000000
[17]  M←1
[18]  G1←○2×F×V[3]÷V[2]
[19]  G2←○2×F×V[6]÷V[5]
[20]  G3←○2×F×V[9]÷V[8]
[21]  G4←○2×F×V[16]÷V[15]
[22]  G5←○2×F×V[19]÷V[18]
[23]  X←(ZO1×(2○G2)×1○G1)+ZO2×(1○G2)×2○G1
[24]  Y←((2○G2)×2○G1)-(1○G2)×(1○G1)×ZO1÷ZO2
[25]  Z←X÷Y
[26]  ZB←Z÷ZO3
[27]  CD←(((2○G3)-1)*2)-(ZB×1○G3)*2
[28]  A←(((2○G3)×(2○G3)-1)+ZB×(1○G3)×1-ZB×1○G3)÷CD
[29]  B←(ZO3×((ZB×1-2○G3)+(1○G3)×((2○G3)×1+ZB*2)-1))÷CD
[30]  C←((ZB×(1○G3)*2)+(1○G3)×(2○G3)-1)÷(CD×ZO3)
[31]  D←((2×((2○G3)-1)*2)-ZB×(1○G3)×(ZB×(1○G3))+1-
      2○G3)÷CD
[32]  Z11←((2○G4)×2○G5)-(1○G5)×(1○G4)×ZO4÷ZO5
[33]  Z12←(ZO5×(2○G4)×1○G5)+ZO4×(1○G4)×2○G5
[34]  Z21←((1○G4)×(2○G5)÷ZO4)+(1○G5)×(2○G4)÷ZO5
[35]  Z22←((2○G4)×2○G5)-(1○G4)×(1○G5)×ZO5÷ZO4
[36]  G←(((Z11×A)-Z21×B)÷N)-((Z11×C)+Z21×D)×N÷○2×F×CO
[37]  H←-((Z22×B)+Z12×A)×○2×F×CO÷N
[38]  I←(((Z12×A)+Z22×B)÷N)+((Z22×D)-Z12×C)×N÷○2×F×CO
[39]  J←((Z11×A)-Z21×B)×○2×F×CO÷N
[40]  K←G+J÷○2×F×COZNS
```

```
[41]  L←I-M÷○2×F×COZNS
[42]  P←1+XS1[M]÷XP1[M]
[43]  S←1
[44]  →47×⍳M≤3
[45]  P←1
[46]  S←1+XS1[M]÷XP1[M]
[47]  Q←XS1[M]×50
[48]  R←-1÷XP1[M]×50
[49]  T←(P×K)-Q×J
[50]  U←(P×L)+Q×H
[51]  O←(R×K)+S×J
[52]  W←(H×S)-R×L
[53]  M←M+1
[54]  RETV←RETV,T, 0 0 ,W
[55]  INTV←INTV,0,U,O,0
[56]  ZOB←ZOB,Z
[57]  FR←FR,F
[58]  F←F+50000000
[59]  →18×⍳F≤1000000000
[60]  II←II+1
[61]  →13×⍳II≤4
[62]  RETM← 5 20 2 2 ⍴RETV
[63]  INTM← 5 20 2 2 ⍴INTV
    ∇


      D1                              T1
2700                            1E¯7
      D2                              T2
4100                            2E¯7
      D3                              T3
5680                            6.35E¯6
      D4                              T4
19320                           2.3E¯7
      D5                              T5
7200                            5E¯8
      V1
6430                                  EP33
      V2                        7.86E¯11
5510                                  EPZNS
      V3                        7.2909502262E¯11
6400                                  C33
      V4                        2.29E11
3300                                  AREA
      V5                        3.22E¯7
6550                                  KT
      DT                        0.2
5330                                  RL
      VT                        50
5600
```

```
      FO                                  ZO1
503937067.9                         5.590242
      CO                                  ZO2
3.985700787E¯12                     7.274302
      ZO                                  ZO3
79.23903651                         11.705344
      COZFC                               ZO4
1.173842986E¯10                     21.0893256
      W                                   ZO5
0.06023781244                       15.18552


      ∇ILTRANS3[⎕]∇

    ∇ ILTRANS3;J;I;W;X;Y

[1]     W←DT,VT,ML
[2]     ZOT←W[1]×W[2]×AREA
[3]     MAGIL←PHASEIL←⍳0
[4]     J←1
[5]     I←1
[6]     X←(RETM[J;I;1;1]×ZOT)+RETM[J;I;1;2]+(W[3]×ZOT×RETM[J;
        I;2;1])+W[3]×RETM[J;I;2;2]
[7]     Y←(IMTM[J;I;1;1]×ZOT)+IMTM[J;I;1;2]+(W[3]×ZOT×IMTM[J;
        I;2;1])+W[3]×IMTM[J;I;2;2]
[8]     MAGIL←MAGIL,(6+20×10⍟2×W[3]×ZOT÷(X*2)+Y*2)
[9]     PHASEIL←PHASEIL,(-(180÷○1)×(-3)○2×X×Y÷(X*2)-Y*
        2)
[10]    I←I+1
[11]    →6×⍳I≤20
[12]    J←J+1
[13]    →5×⍳J≤5
[14]    DATA1← 6 20 ⍴(FR÷1000000),MAGIL
[15]    DATA2← 6 20 ⍴(FR÷1000000),PHASEIL
    ∇
```

# APPENDIX 2

Reprinted from **APPLIED OPTICS**, Vol. 9, page 515, February 1970
Copyright 1970 by the Optical Society of America and reprinted by permission of the copyright owner

## Pulse Repetition Rate Control and Stabilization in a Passively Q-Switched $CO_2$ Laser

G. Hillman, J. Tulip, and H. Seguin

Department of Electrical Engineering, University of Alberta,
Edmonton, Alberta.
Received 29 August 1969.

PREVIOUSLY COPYRIGHTED MATERIAL
IN APPENDIX 2 NOT MICROFILMED:

l. 142